Age-controlled south polar floral trends show a staggered Early Triassic gymnosperm recovery following the end-Permian event

Marcos Amores[1,†], Tracy D. Frank[2], Christopher R. Fielding[2], Michael T. Hren[2], and Chris Mays[1,3]

[1]*School of Biological, Earth & Environmental Sciences, Environmental Research Institute, University College Cork, Cork, T23 TK30, Ireland*

[2]*Department of Earth Sciences, University of Connecticut, Storrs, CT 06269, USA*

[3]*Geological-Palaeontological Department, Natural History Museum Vienna, Burgring 7, Vienna 1010, Austria*

[†]mamores@ucc.ie, https://orcid.org/0000-0003-0487-4453

ABSTRACT

The end-Permian event (EPE, ca. 252.3–251.9 Ma) led to the generalized collapse of gymnosperm-supported ecosystems. They eventually recovered despite Early Triassic suppression and became globally dominant for most of the Mesozoic. Understanding the sequence and timing of gymnosperm reestablishment at different latitudes is therefore key to explaining how they regained their foothold. Given the limited data on polar plant communities, here we present the first high-resolution, age-controlled floristic trends from the high southern latitudes (Sydney Basin, Australia; ~70°S) from the latest Permian to the Middle Triassic. Sedimentological and biostratigraphic data and stable carbon isotope ratios of organic matter were used to establish lithostratigraphic correlations, paleoenvironmental insights, and links to the global chronostratigraphy.

Non-metric multidimensional scaling of spore-pollen groupings confirmed that the late Smithian thermal maximum (LSTM, ca. 250.3–249.6 Ma) and the Smithian-Spathian event (SSE, ca. 249.6–249.2 Ma) were the primary drivers of significant Early Triassic ecosystem changes in the Sydney Basin. Following the EPE, ecosystems supported by peltasperm seed ferns were the first to establish, lasting for ~200,000 years. Voltzialean conifers were thereafter dominant for ~1.5 million years until the LSTM. Stress-tolerant cosmopolitan pleuromeian lycophytes then became the predominant flora, lasting ~800,000 years until SSE-associated cooling allowed umkomasialean seed ferns to expand, which persisted and ultimately characterized Middle-to-Late Triassic high-latitude Gondwanan ecosystems. Global comparisons showed that pleuromeians surged under extreme post-EPE conditions, but their rise was delayed by ~1.7 million years in the polar south. Our findings support the hypothesis that the post-EPE interval was a staggered process rather than one of monotonic recovery, with gymnosperm and lycophyte floral communities waxing and waning in succession until the early Middle Triassic.

Key words: palynology, floristics, stable carbon isotopes, geochronology, end-Permian event, Smithian-Spathian event, Early-Middle Triassic event, Australia.

INTRODUCTION

There were several times in Earth's history when continental ecosystems were disturbed or even destroyed by climate change (e.g., DiMichele et al., 2004; McElwain and Punyasena, 2007). Considering that plants form the foundations of terrestrial trophic webs and are particularly sensitive to climate (Grimm et al., 2013), it is possible to recognize when life on land was impacted by severe climatic changes (Boyce and Lee, 2017) by looking for shifts in fossil

plant communities (e.g., Hochuli and Vigran, 2010; Hermann et al., 2011a; Mays et al., 2020, 2021a; Shu et al., 2023). Given the multitude of disruptive climatic events that punctuate the Phanerozoic Eon (Bond and Grasby, 2017), here we will discuss those that followed in the wake of the most impactful of all (Rojas et al., 2021): the end-Permian event (EPE). The EPE interval occurred ca. 252.3–251.9 Ma (Burgess et al., 2014; Fielding et al., 2019; Gastaldo et al., 2020; Wu et al., 2024). In the Southern Hemisphere, the start of the EPE interval ("EPE horizon" sensu Fielding et al., 2019) is characterized by several key factors, most notably the collapse of widespread, productive glossopterid gymnosperm forests (McLoughlin, 2011; Mays et al., 2020) and the uppermost horizon of the last Permian coal formations, the last in the stratigraphic record for several millions of years (Retallack et al., 1996; Fielding et al., 2019). Herein, we demarcate the termination of the EPE interval as the Permian-Triassic boundary (Burgess et al., 2014), which is marked by spikes in nickel and mercury abundance (Kaiho et al., 2001; Fielding et al., 2019; Shen et al., 2023) and substantial variations in stable carbon isotopic ratios (Cao et al., 2002; Korte and Kozur, 2010). Ecologically, the end of the EPE is linked to a mass extinction of marine faunal species (>80%; Stanley, 2016). As for terrestrial floras, there is debate whether the EPE constituted a "mass extinction" for plant species as well (McElwain and Punyasena, 2007; Nowak et al., 2019). Nevertheless, the EPE is recognized as having the greatest global impact on plant communities in the Phanerozoic (Cascales-Miñana et al., 2016). Mass extinction events are typically followed by so-called "recovery phases," times during which climatic conditions are stable enough for plant communities to gradually reestablish in the landscape (e.g., Hochuli et al., 2010a; Lowery et al., 2018; Lindström, 2021). This often involves a succession of dominant plant groups being replaced by another (e.g., Barreda et al., 2012; Mays et al., 2020; Carvalho et al., 2021). While the timing of ecosystem recovery may be shorter than the recovery of species

richness—as seen in marine faunas (Song et al., 2018; Alvarez et al., 2019)—the length of these recovery phases seems to correlate with the severity of the climatic disturbance (Erwin, 1998; Bond and Grasby, 2017). The structures and functions of global ecosystems following the EPE, for example, appear to have taken millions of years to reestablish themselves (Sahney and Benton, 2008; Chen and Benton, 2012).

The literature on post-EPE plant communities has painted a comprehensive picture regarding the trends and timeline of their recovery. However, an absence of polar/high latitude localities (see fig. 8 in Lindström et al., 2020) emphasizes that there is still much to be known about what transpired in these regions. For instance, polar regions were able to maintain complex ecosystems throughout most of the Permian and Triassic, despite extreme light regimes (e.g., Taylor et al., 1992; Retallack and Krull, 1999; Gulbranson et al., 2012). Considering the modern phenomenon of polar amplification, whereby temperature variations are more pronounced at the poles (Stuecker et al., 2018), would paleopolar plant communities have been more vulnerable to global temperature changes? Would a milder/flatter latitudinal gradient of diversity for terrestrial biotas (as observed in the marine record; Song et al., 2020) mean that polar regions acted as refugia for floras originating at lower latitudes during the late Permian to Early Triassic warming events (e.g., Bomfleur et al., 2018)?

To assist in answering these questions, here we present the long-term shifts of the paleopolar floral communities of the Sydney Basin (southeastern Australia), examined over an ~8-million-year interval, from the pre-EPE late Permian to the early Middle Triassic. With regional biostratigraphic and global stable carbon chemostratigraphic correlations, these long-term floristic trends were compared to coeval localities around the world to test whether the observed changes were globally synchronous or regionally variable. We hypothesize that the

Early to Middle Triassic polar gymnosperm forest communities: (1) were severely impacted by global climate events and (2) experienced quicker recoveries following hyperthermal events, relative to lower latitude communities, owing to generally cooler climates as a result of lower insolation.

PALEOCLIMATIC AND GEOLOGICAL CONTEXT

Stable Carbon Isotope Ratios and Global Warming Events

Stable carbon isotope ratios ($\delta^{13}C$) are useful in paleoenvironmental studies, particularly for global climate-driven ecosystem changes, since: (1) they assist in correlating local lithostratigraphy to the global chronostratigraphy (Gröcke, 2020), and (2) they are consistently linked to major global warming/cooling events (e.g., Gröcke, 1998, 2002; Hesselbo et al., 2003; Hren et al., 2009; Korte and Kozur, 2010; Ruhl et al., 2011; Sun et al., 2012; Schobben et al., 2019; Hesselbo et al., 2020). Given the high number of prominent global carbon isotope excursions across the late Permian to Middle Triassic (Payne et al., 2004; Gradstein et al., 2020; Ogg et al., 2020, p. 905), the $\delta^{13}C$ record of this interval is exceptionally suited for correlating the associated climatic and biotic events to the global geochronology. These erratic $\delta^{13}C$ variations are probably owing, in large part, to a combination of intermittent intrusive magmatic activity from the Siberian Traps and associated carbon cycle disruptions (Svensen et al., 2018; Elkins-Tanton et al., 2020)—that persisted long after its main phase of action during the end-Permian event (EPE; Burgess and Bowring, 2015; Augland et al., 2019)—and the absence of stable, $\delta^{13}C$-regulating land plant carbon sinks (e.g., peatlands) following their worldwide devastation at the EPE (Xu et al., 2022).

At least three globally recognizable episodes of carbon dioxide degassing are known for the Early Triassic (Paton et al., 2010; Du et al., 2022), all of which have been linked to major, near-concurrent negative $\delta^{13}C$ excursions (Zhang et al., 2018). Following the nomenclature presented by Song et al. (2013), these correspond to the early Griesbachian "N1," the Griesbachian-Dienerian "N2," and the Smithian "N3" (Fig. 1). The end of the N3 negative $\delta^{13}C$ excursion coincided with a hyperthermal episode called the "late Smithian thermal maximum" (LSTM; Lindström et al., 2020; Du et al., 2022), when exceptional warming was present for over half a million years (ca. 250.3–249.6 Ma; Widmann et al., 2020; Du et al., 2022) and temperatures soared to levels similar to those observed during the EPE (Sun et al., 2012). Middle and late Smithian fossil floras indicate a concurrent spread of opportunistic, herbaceous isoëtalean lycophytes (Retallack, 1997; Lindström et al., 2020; Schneebeli-Hermann, 2020; Vajda and Kear, 2024), these being particularly represented by members of the Pleuromeiaceae and Isoëtaceae families (Looy et al., 2021).

Following the LSTM termination, a cooling trend began to manifest around the Smithian-Spathian substage boundary (Sun et al., 2012; Widmann et al., 2020), which is chemostratigraphically represented by the "P3" (Song et al., 2013) positive $\delta^{13}C$ excursion (Fig. 1). High-precision U-Pb zircon dating from the low paleolatitude marine deposits of southern China reveal that the P3 lasted for ~400 thousand years (k.y.), starting at ca. 249.6 Ma and ending at ca. 249.2 Ma (Widmann et al., 2020). Climatic responses simultaneously hindered and fostered ecosystems during this time interval, the causes and effects of this event being hereafter collectively referred to as the "Smithian-Spathian event" (SSE). For instance, in the marine realm, the SSE negatively impacted the diversity of ammonoids and conodonts (Stanley, 2009; Widmann et al., 2020). These impacts were apparently spatiotemporally distinct between

regions, however, as disappearances of some of the same marine groups seem to have been expressed during the preceding LSTM, rather than the SSE (Zhao et al., 2020; Leu et al., 2023). In the terrestrial realm, the SSE allowed for the return of some gymnosperm forest communities (e.g., Hermann et al., 2011a; Lindström et al., 2020; Mays et al., 2021a), with certain regions (e.g., Europe), reflecting very little change during this event (Looy et al., 1999), which highlights the complicated nature of regionally and temporally distinct climatic changes.

The boundary between the Early and Middle Triassic is chemostratigraphically identified by the "P4" (Song et al., 2013) positive $\delta^{13}C$ excursion (Fig. 1). High-precision U-Pb zircon dating places this boundary at ca. 247.2 Ma (Lehrmann et al., 2015), with younger ages being proposed based on astrochronology (ca. 246.8 Ma; Li et al., 2018) and chemo-bio-magneto-stratigraphy (ca. 246.7 Ma; Chen et al., 2020). The P4 has been linked to cooling temperatures, with equatorial temperature reductions of ~3.5°C in south China (Sun et al., 2012), and of ~6°C in Turkey (paleolatitude: ~20°N; Trotter et al., 2015). Herein, we refer to the biotic and climatic trends that occurred during this P4 interval as the "Early-Middle Triassic event" (EMTE), which sees gymnosperm fossil abundances remaining common in most known records, even after the termination of this event (Looy et al., 1999; Lindström et al., 2017; Kustatscher et al., 2018; Peng et al., 2019; Xu et al., 2022).

Geological and Stratigraphic Setting

The locality of interest—the Sydney Basin—is in the central-eastern portion of New South Wales, Australia (Herbert and Helby, 1980). During the Early Triassic (ca. 250 Ma; Fig. 2A), it was within the south polar circle at ~70°S (Müller et al., 2022). The basin includes a southeast-plunging synclinorium composed of Permian to Triassic sedimentary rocks (Fielding et

al., 2021) and presently (Fig. 2B) extends over an ~36,000 km^2 onshore area (Mayne et al., 1974, p. 3). The basin opened during a time of crustal extension in the early Permian and became a retroarc foreland basin by the late Permian following tectonic compression (Jessop et al., 2019). This allowed for considerable amounts of sedimentary material to be deposited over tens of millions of years, with the onshore central portion—informally known as the Central Coalfield (Mayne et al., 1974, p. 5–7; Ward et al., 1995)—preserving a succession ~2.3 km thick today (Mayne et al., 1974, p. 111).

The basin included marine environments throughout most of the Permian, but pulses of orogenic uplift led to progressively more terrestrially influenced environments (Ward, 1972; Goldbery and Holland, 1973; Herbert, 1997; Fielding et al., 2021): from coastal-deltaic in the early late Permian, to a lowland alluvial plain by the latest Permian, and continuing into the Early Triassic, with coastal and shallow marine influences higher in the section. Fluvial systems transported and deposited sediments from the Lachlan Orogen in the west (Herbert, 1980; Richard et al., 1983), the rising New England Orogen in the east (Herbert, 1980; Fielding et al., 2021), and the rest of the Sydney-Gunnedah-Bowen Basin System to the north (Ward, 1972; Cowan, 1993; Fielding et al., 2021). The youngest strata in the Sydney Basin belong to the shale-rich Wianamatta Group, which has been assigned an Anisian Age (lower Middle Triassic; Colquhoun et al., 2024), though it may be as young as Ladinian (upper Middle Triassic; Herbert, 1997).

MATERIALS AND METHODS

Core Sampling

The examined strata (Table 1) are in the synclinal axis of the Sydney Basin, eastern Australia (Fig. 2B), and were targeted for their (almost) complete stratigraphical continental record of the upper Permian to Middle Triassic. The Permian strata correspond to the Illawarra Coal Measures (Bowman, 1980; Ward et al., 1995; McLoughlin et al., 2021), with the Triassic strata belonging to the Narrabeen Group and Hawkesbury Sandstone (Herbert, 1980, 1997; Fielding et al., 2019). We collected data from two drillcores (Fig. S1[1]): (1) Pacific Power Hawkesbury Bunnerong DDH 1 (33°58′17.61″S, 151°13′43.52″E; hereafter shortened to "Bunnerong-1") and (2) Pacific Power Hawkesbury Eveleigh DDH 1 (33°53′42.89″S, 151°11′32.92″E; hereafter shortened to "Eveleigh-1"). These are housed at the W.B. Clarke Geoscience Centre in Londonderry, New South Wales, Australia. The newly obtained data were from strata belonging to Lower-and-Middle Triassic lithostratigraphic units, with the lowermost and uppermost examined units being the Stanwell Park Claystone and the Hawkesbury Sandstone, respectively (Herbert, 1997; Fielding et al., 2021; McLoughlin et al., 2021). Sediment sample targets were principally organic-rich mudrocks (i.e., dominated by claystone and siltstone). Additional samples were collected from coarser-grained sediments (i.e., sandstones with mudrock laminae) when the spatial interval between mudrocks was >25 m. Each sample has been given a simplified lithofacies description, provided as supplementary data in Table S1 (see Footnote 1). Sampling depth targets were constrained by previously published works on the Lower Triassic succession of the Sydney Basin (Metcalfe et al., 2015; Fielding et al., 2019), or lithological logs in unpublished well completion reports (Bunnerong-1: Smith and Bocking, 1994, chap. 6.1; Eveleigh-1: Smith and Bocking, 1993, chap. 6.1). All depths are presented as depth below the surface.

205 **Stable Carbon Isotopes and Total Organic Carbon**

206 Stable carbon isotope ratios of bulk organic sediments ($\delta^{13}C_{org}$) and total organic carbon
207 (TOC) were measured from 159 samples (Table S1): 91 from Bunnerong-1 and 68 from
208 Eveleigh-1. Most samples (132) were processed by Iso-Analytical Ltd. in Crewe, UK, with the
209 rest (27) being processed at the Stable Isotope and Organic Molecular Biogeochemistry
210 Laboratory, University of Connecticut, Storrs, Connecticut, USA. The full protocol used for
211 processing samples is described in Appendix 1. These new data were combined with previously
212 collected data from Fielding et al. (2019), Mays et al. (2020), and Shen et al. (2023). The global
213 chronostratigraphic correlations (and associated floristic and lithological trends) of the Sydney
214 Basin were calibrated following the global $\delta^{13}C$ signature (Gradstein et al., 2020, and references
215 therein). Nomenclature for the Early Triassic positive (P) and negative (N) carbon isotope
216 excursions follow Song et al. (2013). The carbon isotope excursion intervals expressed in this
217 paper terminate at the peaks indicated by Song et al. (2013), but also include the entire excursion
218 interval preceding each peak. Analyses of geochemical data were done with R version 4.4.1 (R
219 Core Team, 2025) using RStudio Desktop version 2024.04.2+764 (Posit Team, 2025). Graphical
220 representation, including three-point estimation lines, were obtained using the R packages
221 ggplot2 (Wickham, 2016) and dplyr (Wickham et al., 2023).
222
223 **Palynology and Floristics**

224 For palynological analyses, we retrieved ~20–35 g of sedimentary rock from 76 samples
225 (Table S1): 36 for Bunnerong-1 and 40 for Eveleigh-1. Processing of organic microfossils
226 (including palynofacies and palynomorph assemblages) was done at Global Geolab Ltd. in
227 Medicine Hat, Alberta, Canada, using traditional palynological techniques (see Riding, 2021,

chaps. 7–10), with specific processing details being provided in Appendix 1. We conducted palynofacies counts on pre-oxidized residues (=kerogen slides) with no lower or upper sieve. Palynomorph counts were conducted on oxidized residues sieved with a lower sieve of 10 µm and with no upper sieve. We collected palynofacies data (Table S1) by counting each particle over 10 µm and categorizing them following an updated scheme by Tyson (1995, chap. 20.4): (1) plant spores and pollen; (2) algae and probable algal acritarchs (sensu Mays et al., 2021b); (3) phytoclasts; (4) fungi; and (5) amorphous organic matter (AOM), subdivided into resin and other AOM (i.e., granular and gelified). Fungal spores and algal/acritarch cysts are here independently considered due to their relevance as proxies for acute ecological changes (e.g., Vajda et al., 2020; Mays et al., 2021a). A Zeiss Axioskop 2 Plus transmitted light microscope with differential interference contrast was used to observe the prepared palynology slides.

All kerogen counts consisted of ≥500 discrete particles. For the palynomorph counts the target count size was ≥300 specimens, with a minimum of 200 counts being accepted. We did not include samples rendering fewer than 200 palynomorphs in statistical analyses. These count sizes were deemed adequate for the floristic trends described herein, given the broad palynological categories used—hence, large proportional abundances of each—which significantly reduces the potential error rates (see Weng and Hooghiemstra, 2024). Considering new and previous collected data together, this was the case for 26 samples in Bunnerong-1 and two in Eveleigh-1 (depths in Table S1). Samples that appeared depleted of palynomorphs were branded as barren. Land plant pollen and microspores (collectively "miospores") were grouped into seven broad morphological categories, following Mays et al. (2020): (1) acavate trilete spores, (2) cavate trilete spores, (3) acavate monolete spores, (4) cavate monolete spores, (5) non-taeniate bisaccate pollen, (6) taeniate bisaccate pollen, and (7) other pollen (e.g., non-

saccate). For palynomorph identifications, we captured multiple photomicrographs of each counted specimen at different focal depths with a Canon EOS 700D camera attached to the microscope. We then "focus-stacked" photographs (five per specimen on average, more for larger specimens) following the protocol outlined by Bercovici et al. (2009) using Helicon Focus version 8.2.2 (Kozub et al., 2025). We combined palynological data for Bunnerong-1 with those collected previously (Fielding et al., 2019; Mays et al., 2020). The identification of key index taxa enabled the biostratigraphic correlation of assemblages to the schemes of Helby et al. (1987), Price (1997), and Mays et al. (2020); additional details of these correlations are provided in the Discussion section. In Appendix 2, we discuss the long-standing issue of distinguishing *Alisporites* and *Falcisporites*; while we recognize that they are not synonymous, we conflated these taxa herein with the broader diagnosis of *Alisporites*.

We rendered palynofacies and palynomorph compositional data plots in C2 version 1.8.0 (Juggins, 2025). All palynological slides are registered with the prefix "S" (Table S1) and are housed at the Swedish Museum of Natural History, Stockholm, Sweden. Additional data for figured specimens, including England Finder locations, are given in Table S2. All mentioned taxon authorities (including sources) are given in Table S3. We do not present any new macrofloral data, nor do we aim to provide a comprehensive systematic taxonomic review of the macrofloral taxa mentioned herein. In our review of these occurrences and abundances, we have utilized the taxonomic designations attributed to these taxa by the cited authors. The macrofloral abundance data of the Sydney Basin are compiled from Retallack (1975, 1977, 1980, 1997, 1999), Fielding et al. (2019), and Mays et al. (2020); however, a standardized quantitative analysis of macrofloral data from this region is presently lacking. Therefore, these trends should be considered preliminary.

Ordination and Cluster Data Analysis

We established temporal groupings (=clusters) of palynological assemblages for Bunnerong-1 and Eveleigh-1 using compositional data of land plant palynomorph data (expressed in percentages). These clusters (Fig. S2) were determined using constrained incremental sum of squares (CONISS) cluster analysis (Grimm, 1987), and visualized with Tilia version 3.0.3 (Grimm, 1991). We named each clustered microfloral assemblage according to identified $\delta^{13}C$ excursions linked to global climatic events (Fig. 1). The clusters are (in stratigraphic order): (1) pre-EPE, (2) post-EPE, (3) syn-LSTM, (4) post-SSE, and (5) post-EMTE. The stratigraphic depths and intervals that correspond to these clusters/time bins are specified in Table S1. From these clusters, we conducted ordination analysis and visualization with non-metric multidimensional scaling (nMDS). This was performed to statistically determine the primary spore and pollen contributors that characterize the assemblage groupings across time and between climatic events in a two-dimensional plot. This non-parametric method has been applied in ecological studies (Minchin, 1987) and has recently enjoyed increased usage by palynologists (e.g., Broothaerts et al., 2018; Peng et al., 2018; Slater et al., 2019; Mays et al., 2020, 2021a). Bray-Curtis was the chosen similarity index, as it allows for the ordination of group abundance differences between sites (or sampled depths, in the present case). One of the weaknesses of this index is its sensitivity to samples with group abundances of zero (Clarke et al., 2006); however, the impact of this effect was mitigated by the broadness of the morphological groups analyzed herein, therefore promoting larger group abundances. To visualize the ordination goodness-of-fit, a Shepard plot is provided as supplementary in Figure S3. Ordination analysis was performed with PAST version 4.17 (Hammer et al., 2001).

RESULTS

Geochemical and Microfloral Trends

Below, we summarize in stratigraphic order the litho-, chemo- and biostratigraphical trends that we observed. Owing to the similarity in these trends for both cores—Bunnerong-1 (Fig. 3) and Eveleigh-1 (Fig. 4)—these were considered together to minimize redundancy, but we have drawn contrasts where the data diverged. Recovered index miospore taxa indicate that the palynological assemblages of the newly processed samples range from the *Protohaploxypinus samoilovichii* Palynozone to the *Aratrisporites parvispinosus* Palynozone (Foster, 1982; Helby et al., 1987; Mays et al., 2020), which correspond to the informal, regional APT1 to APT3 zones of Price (1997). Unless specified, all fossil abundances presented as percentages represent the mean values for the specified chronostratigraphic interval. Supplementary material contains more exhaustive information on each sampled stratigraphic depth (Table S1), in addition to the full statistical results for $\delta^{13}C_{org}$ and total organic carbon (Table S4). For the Lopingian and Induan, almost all data come from previously mentioned published studies, which are here combined and recontextualized with the new data.

Lopingian

The Lopingian Series (late Permian) data corresponded to the upper Illawarra Coal Measures, specifically the Wongawilli Coal (Wuchiapingian Stage) and Eckersley Formation (Changhsingian Stage). Strata before the end-Permian event (EPE) exhibited fluctuations in $\delta^{13}C_{org}$ not exceeding ±1.7‰ from the mean. Total organic carbon displayed greater variability,

with ±4.02% for Bunnerong-1 (median = 2.68%, min = 0.22%, max = 6.83%) and ±16.07% for Eveleigh-1 (median = 2.39%, min = 0.49%, max = 31.57%).

Palynofacies analysis revealed that phytoclasts were the predominant components (89%), followed by spores/pollen (8%), and AOM (3%). Miospores were primarily acavate trilete spores (77%): mainly laevigate (e.g., *Leiotriletes*), granulate (e.g., *Osmundacidites*), and baculate taxa (e.g., *Horriditriletes, Microbaculispora, Neoraistrickia, Raistrickia*). Taeniate bisaccate pollen were also commonly found (9%), which consisted of pollen typical of Glossopteridales (e.g., *Protohaploxypinus*, Figs. 5F, 5G, 5J; *Striatopodocarpites*, Fig. 5L). Cavate trilete spores (7%), and non-taeniate bisaccate pollen (6%) made up the rest of the assemblage.

The EPE interval (uppermost Lopingian) is characterized by a $\delta^{13}C_{org}$ excursion of −1.6‰ in Bunnerong-1 (Fig. 3) and −1.8‰ in Eveleigh-1 (Fig. 4). The start of the EPE coincided with the top of the *Dulhuntyispora parvithola* Palynozone (ca. 257.6–252.3 Ma; Laurie et al., 2016; Mays et al., 2020) and the onset of a biostratigraphic "dead zone" (sensu Vajda et al., 2020), characterized by negligible numbers of identifiable palynomorphs in addition to a spike in charcoal abundance (from a high late Permian baseline; Mays and McLoughlin, 2022). Directly overlying the "dead zone" is the *Playfordiaspora crenulata* Palynozone (ca. 252.3–251.9 Ma), characterized by the co-occurrence of several distinctive trilete spore taxa (Foster, 1982; Price, 1997), including the acavate rugulate *Triplexisporites playfordii* (Fig. 6A), the cavate *P. crenulata* (Fig. 6U), and the acavate echinate/conate *Brevitriletes bulliensis*. Lithostratigraphically, the EPE interval encompasses the short Frazer Beach Member—the uppermost unit of the Illawarra Coal Measures (McLoughlin et al., 2021)—and most of the Coal Cliff Sandstone (Fig. 1). Although phytoclasts still dominate the palynofacies assemblage (Fig. 3), there is a notable increase in AOM, accounting for ~27%. As noted by Mays et al. (2021a),

342 an increase in algal content is observed commencing at 802.97 m in Bunnerong-1. Miospores
343 continued to be primarily acavate trilete spores (66%), but with acavate monolete spores (e.g.,
344 *Thymospora*) rising in abundance (18%). The proportion of taeniate bisaccate pollen decreased
345 by approximately half (4%), and non-taeniate bisaccate pollen remained relatively stable (5%).
346
347 ***Induan***
348 The Griesbachian substage (lower Induan Stage, lowermost Lower Triassic) exhibited
349 notable fluctuations in $\delta^{13}C_{org}$ in comparison to the preceding Lopingian, with variations of up to
350 ±4.0‰ from the mean. Total organic carbon remained consistently low, with values of 0.19% ±
351 0.21% in Bunnerong-1 (Fig. 3) and 0.23% ± 0.34% in Eveleigh-1 (Fig. 4). Biostratigraphically,
352 this interval witnessed the establishment of a series of distinct palynofloral assemblages in
353 relatively rapid succession: the first being the *Protohaploxypinus microcorpus* Palynozone (ca.
354 251.9–251.8 Ma). This palynozone (Helby et al., 1987; Mays et al., 2020) is characterized by the
355 association of *Playfordiaspora crenulata* (Fig. 6U), the taeniate bisaccate pollen
356 *Protohaploxypinus microcorpus* (Fig. 5G), and by the first appearances of the trilete cavate
357 spores *Rewanispora foveolata* and *Lundbladispora springsurensis* (Fig. 6H). Other characteristic
358 features of this palynozone are: (1) persistently low palynomorph concentrations (Mays et al.,
359 2020, 2021a) and (2) an assemblage of non-taeniate bisaccate pollen mostly consisting of
360 *Alisporites* (Fig. 5D; Helby, 1970; Price, 1997). Probable freshwater leiospherid acritarchs and
361 the fern spore *Brevitriletes bulliensis* are present in this palynozone and are often very abundant
362 (Mays et al., 2020). The overlying upper Griesbachian *Lunatisporites pellucidus* Palynozone (ca.
363 251.8–?251.7 Ma) is characterized by high abundances of the taeniate bisaccate pollen *L.*
364 *pellucidus* (Figs. 5H and 5K; Helby et al., 1987), *L. noviaulensis* (Fig. 5I), and

365 *Protohaploxypinus samoilovichii* (Figs. 5F and 5J; Helby, 1970, p. 312–313). This palynozone is
366 also associated with the co-occurrence of *Limatulasporites fossulatus* (Fig. 6F) and *L. limatulus*
367 (Fig. 6G; Mays et al., 2020). The upper Griesbachian to lower Spathian *Protohaploxypinus*
368 *samoilovichii* Palynozone (ca. ?251.7–249.3 Ma) is defined by the first appearance of the cavate
369 monolete spore *Aratrisporites* (Figs. 6I–6S; Helby et al., 1987; Mays et al., 2020). Price (1997,
370 p. 161) argues caution against using the first appearance of the *Aratrisporites* genus as a
371 correlatable bioevent, however, mentioning the fact that *Aratrisporites* can resemble the aborted
372 spores of *Lundbladispora*. Hence, the informal palynostratigraphy by Price (1997) differs here
373 from the formal scheme of the region for this interval in the Lower Triassic (Foster, 1982; Helby
374 et al., 1987) in the sense that the *P. samoilovichii* Palynozone is offset from the proposed APT2
375 of Price (1997). The latter palynozone is defined by the appearance of the species *A. wollariensis*
376 (Figs. 6I–6K), which only appears in the middle Smithian of the Sydney Basin (mid–*P.*
377 *samoilovichii* Palynozone, mid–Bulgo Sandstone; Figs. 3 and 4). Compared to the pre-EPE
378 Lopingian, Induan palynofacies assemblages showed a relative decrease in phytoclasts (from
379 89% to 78%), and a corresponding increase in AOM (from 3% to 15%). Induan palynomorph
380 assemblages were predominantly acavate trilete spores (63%), followed by non-taeniate
381 bisaccate pollen (14%). Acavate monolete spores increased to 8% (from <1% in the pre-EPE
382 Lopingian), while taeniate bisaccate pollen maintained a relatively stable proportion (5%). Ten
383 assemblages were barren during the Griesbachian substage.
384 The Dienerian substage (upper Induan) did not exhibit major fluctuations in $\delta^{13}C_{org}$ nor in
385 total organic carbon. Between the lower and upper Induan, palynofacies analysis indicated a
386 decrease in phytoclasts (from 82% to 70%) accompanied by an increase in AOM (from 10% to
387 26%), with spores/pollen proportions remaining stable (4%). Low sampling density could be the

388 reason behind the substantial gap in palynomorphs between 661.09 m and 637.36 m in
389 Bunnerong-1 (Fig. 3), as only six depths (three barren) were sampled inside the Dienerian
390 substage (Table S1). With this caveat in mind, Dienerian plant microfossil assemblages showed
391 similar proportions to those in the preceding Griesbachian substage. There is an apparent trend
392 where non-taeniate bisaccate pollen decreased across the Dienerian (from 9% to 5%), and cavate
393 monolete spores emerged as uncommon members (2%). Within the apparently barren interval
394 (Fig. 3), palynofacies have AOM proportions reaching 49%, with scarce spores/pollen being
395 present (~1%).
396
397 ***Smithian (lower Olenekian)***
398 The Smithian substage (lower Olenekian Stage, early-to-middle Lower Triassic) interval
399 is entirely encompassed within the Bulgo Sandstone: including ~245 m of strata in Bunnerong-1
400 (Fig. 3), and ~280 m in Eveleigh-1 (Fig. 4). Fluctuations in $\delta^{13}C_{org}$ values for the Smithian
401 reached ±3.3‰ from the mean in Bunnerong-1 (Eveleigh-1: ± 2.6‰), with TOC values
402 averaging 0.22% ± 0.25% (Eveleigh-1: 0.33% ± 0.67%). In the middle-to-upper Smithian, a
403 substantial but gradual negative excursion in $\delta^{13}C_{org}$ was observed (= N3). Palynofacies
404 assemblages before the N3 excursion in Bunnerong-1 (Fig. 3; 587.47 m) revealed a
405 predominance of phytoclasts (78%), followed by spores/pollen (15%) and AOM (5%).
406 Palynomorphs were dominantly acavate trilete spores (57%), with common acavate monolete
407 spores (17%), cavate trilete spores (11%), and taeniate bisaccate pollen (8%). Palynological data
408 within the N3 excursion in Bunnerong-1 (559.60–477.20 m) showed a fourfold relative increase
409 of cavate trilete spore proportions (from 13% to 47%). Although the proportion of taeniate
410 bisaccate pollen and other pollen are similar throughout (~11%), non-taeniate bisaccate pollen

411 decreased by more than half (from 7% to 2%). In the case of Eveleigh-1 (Fig. 4), the interval
412 before the N3 excursion saw taeniate bisaccate pollen attaining proportions as high as 46% at
413 613.63 m.

414 Plant palynomorph composition underwent a drastic shift after the end of the N3
415 excursion, now predominantly made up by cavate trilete spores (Bunnerong-1: 72%; Eveleigh-1:
416 64%), the majority of these being *Densoisporites*, particularly *D. nejburgii* (= *D. narrabeenensis*,
417 sensu Helby, 1970, p. 171–172; Figs. 6B–6E). Considering all spores/pollen, *D. nejburgii* made
418 up 71% of the assemblage in Bunnerong-1 (Fig. 3; ~87% between 420.25 m and 418.01 m) and
419 47% in Eveleigh-1 (Fig. 4). Acavate trilete spores accounted for 11% in Bunnerong-1 and 9% in
420 Eveleigh-1, with non-taeniate bisaccate pollen remaining rare at ~3% and taeniate bisaccate
421 pollen keeping their steady representation (8% in Bunnerong-1), although gradually reducing in
422 both cores until the end of the Smithian. Palynofacies data revealed similar substantial changes
423 (Bunnerong-1: 460.13–420.25 m; Eveleigh-1: 539.97 and 519.33 m), with phytoclasts reducing
424 from 78% to 45%, and spores/pollen increasing from 15% to 37%. Fungal microfossils became
425 more common throughout this interval in Bunnerong-1—although still in relatively low
426 abundances (<1%)—alongside the persistent but uncommon presence of algae in both cores.
427
428 ***Spathian (upper Olenekian)***

429 The positive $\delta^{13}C_{org}$ excursion (= P3) marking the Smithian-Spathian substage boundary
430 (middle Olenekian) is expressed in the uppermost section of the Bulgo Sandstone (Fig. 1). In
431 Bunnerong-1 (Fig. 3), the P3 excursion is represented by an excursion of +4.4‰ across ~26 m of
432 strata (418.01–391.88 m), with Eveleigh-1 (Fig. 4) experiencing +1.9‰ over ~35 m (490.54–
433 456.09 m). Palynofacies within this interval revealed a drastic reduction in spores/pollen

representation: in Bunnerong-1 (Fig. 3) these dropped from 58% at 418.01 m to <1% at 410.14 m, averaging ~9% thereafter. In their stead, phytoclasts became the most common element (55%), followed by AOM (27%); a similar pattern being noted for Eveleigh-1 (Fig. 4). These broad proportions do not fully capture the extent of the palynofacies fluctuations occurring during the P3, however. Focusing on Bunnerong-1 (Fig. 3), spores/pollen dominated the palynofacies (66%) before the P3 onset at 420.25 m. By 410.14 m, however, their presence drastically decreased (<1%) and they were replaced by a mixture of phytoclasts (44%) and AOM (55%). Only toward the conclusion of the P3 (~391.88 m) do spores/pollen once again became prominent components of the palynofacies (19%). Plant palynomorph assemblages have consistently high abundances of cavate trilete spores (72%–87%) between the depths of 420.25 m and 408.20 m. However, near the conclusion of the P3 (393.18 m), their representation declined sharply to 2% and non-taeniate bisaccate pollen became dominant, representing 61% of the assemblage, followed by azonate trilete spores (31%). The most representative gymnosperm pollen in this interval (393.18–391.88 m) are *Alisporites australis* (Fig. 5D) and *Chordasporites australiensis* (Fig. 5C). In Eveleigh-1, a similar signal is revealed between 457.51 and 450.38 m (Fig. 4). Here, *Vitreisporites pallidus* (Fig. 5A) and *Pteruchipollenites indarraensis* (Fig. 5B) were a common occurrence, in addition to the aforementioned *A. australis* and *C. australiensis*.

The P3 excursion, ending at ~391 m in Bunnerong-1 (Fig. 3) and ~457 m in Eveleigh-1 (Fig. 4), was immediately followed by the early Spathian negative $\delta^{13}C_{org}$ excursion (= N4). This coincided with a substantial lithological shift, where facies transition from bluish gray mudrocks of the uppermost Bulgo Sandstone to kaolinitic “red bed” mudrocks of the Bald Hill Claystone, historically referred to as “red shales” (Clarke, 1878) or “chocolate shales” (Goldbery and Holland, 1973). Relative to its initiation near the base of the primary red bed facies interval, the

N4 culminated in a total negative excursion of −4.1‰ in Bunnerong-1 and −4.4‰ in Eveleigh-1. The lower Spathian is correlated to the onset of the *Aratrisporites tenuispinosus* Palynozone (ca. 249.3–247.2 Ma), which is defined (Helby et al., 1987; Price, 1997) by the large relative abundance increases of *Alisporites australis* (Fig. 5D) and the cavate monolete spore *A. tenuispinosus* (Figs. 6M–6O), the near-complete absence of *Lunatisporites* spp. (Figs. 5H, 5I, and 5K), and the decline of cavate trilete spores (e.g., *Densoisporites*). The initial part of this palynozone in the lower Spathian (ca. 249.0 Ma) comprised diverse *Aratrisporites* spp., with *A. coryliseminis* (Figs. 6Q and 6R), *A. strigosus* (Fig. 6L), and *A. plicatus* (Fig. 6P) being especially common.

In Bunnerong-1 (Fig. 3), the palynofacies assemblages from 383.48 m to 370.32 m (lower Spathian) revealed wildly variable AOM values (median: 12%; minimum: 6%; maximum: 92%). Microfossils primarily consisted of cavate monolete spores (36%), peaking at 373.02 m (55%), with *Aratrisporites* consistently being the sole representative of this group. Non-taeniate bisaccate pollen initially experienced a sharp decline between the P3 and N4 excursions, from a maximum of 60% at 391.88 m to a minimum of 10% at 387.99 m, before rising to their previous dominance (60%) at 370.32 m. Assemblages remained rather consistent for the remainder of the Spathian in both cores; however, taeniate bisaccate pollen, which averaged ~5%, increased considerably around the middle Spathian, up to ~22%.

Anisian

The transition from the upper Bald Hill Claystone to the Garie Formation is accompanied by a major positive $\delta^{13}C_{org}$ excursion (+6.1‰ in Bunnerong-1, +4.8‰ in Eveleigh-1). Chronostratigraphically, the approximate midpoint of this positive excursion (= P4) indicates the

480 boundary between the Olenekian and Anisian Stages (Lower-Middle Triassic boundary;
481 Gradstein et al., 2020). Total organic carbon showed a gradual increase—the first since the EPE,
482 but still far below pre-EPE levels—with Anisian sections in Bunnerong-1 showing a median of
483 0.81% (min = 0.13%, max = 1.75%) and in Eveleigh-1 of 1.02% (min = 0.51%, max = 2.41%).
484 Biostratigraphically, the *Aratrisporites parvispinosus* Palynozone, which extends from the
485 Olenekian-Anisian boundary (247.2 Ma) to the Ladinian (Price, 1997), first appeared in the
486 Sydney Basin concurrent with the P4 excursion. This palynozone is defined by the first
487 consistent appearance of *A. parvispinosus* and lasts until the appearance of *Craterisporites*
488 *rotundus* (Helby et al., 1987). The same authors further described this palynozone as being
489 dominated by the non-taeniate bisaccate pollen *Alisporites australis* (Fig. 5D). Price (1997)
490 proposed a concurrent but alternate informal palynozone (designated APT3), the base of which is
491 defined by the first appearance of *Striatella scanica* and the top by the first appearance of
492 *Annulispora folliculosa*. Of these index taxa, we have only recorded the presence of
493 *Aratrisporites parvispinosus* and an increase in *Alisporites australis* for the Anisian sections of
494 Bunnerong-1 and Eveleigh-1, and none of the additional taxa reported by Helby et al. (1987) and
495 Price (1997) for the *A. parvispinosus* Palynozone were identified in this study. Since most of
496 these accessory taxa occur above the base of the *A. parvispinosus* Palynozone, their absence
497 suggests that only the lower portion of this zone is preserved in both analyzed cores.
498 Palynofacies assemblages for the Anisian in Bunnerong-1 (Fig. 3; 301.11–26.34 m)
499 consisted of phytoclasts (72%), followed by AOM (19%), and spores/pollen (9%). The Anisian
500 strata in Eveleigh-1 (Fig. 4; 357.00–19.24 m) showed comparatively lower proportions of
501 phytoclasts (50%) and considerably more AOM (42%). Fungal and algal remains declined across
502 the Garie Formation to nearly 0% and remained rare until the top of the examined strata in both

503 cores. Taeniate bisaccate pollen were rare (~1%), and non-taeniate bisaccate pollen showed a
504 steady increase throughout the Anisian, becoming the most common group in the uppermost
505 analyzed parts of both cores (from 19% to 58% in Bunnerong-1, and from 19% to 46% in
506 Eveleigh-1). Other pollen groups also increased in proportion, including monosaccate pollen,
507 such as *Striomonosaccites morondavensis* (Fig. 5M), and non-saccate pollen, such as the colpate
508 *Cycadopites follicularis* (Fig. 5E), and the polyplicate *Praecolpatites* sp. cf. *P. sinuosus*.
509
510 **Ordination Data Analysis**
511 Non-metric multidimensional scaling (nMDS) data ordination (Fig. 7A) resulted in a
512 stress value equal to 0.1082 (Fig. 7B). According to Clarke (1993), stress lower than 0.1 signifies
513 good ordination with negligible risk of drawing false inferences. Stresses lower than 0.2 are
514 considered usable; however, caution is needed if values tend toward 0.2.
515 The pre-EPE group of microfloral assemblages (Fig. 7A) displayed the lowest degree of
516 variation (i.e., smallest ordination plot area) of all considered time bins, reflecting the relatively
517 uniform climax floras of the "*Glossopteris* flora" (Mays et al., 2020). The post-EPE assemblage
518 group exhibited a broader range, with an overall shift toward a higher proportion of non-taeniate
519 bisaccate pollen (e.g., *Alisporites, Vitreisporites*). No overlap existed between post-EPE and syn-
520 LSTM microfloras, indicating a considerable turnover from an association made up mostly by
521 acavate trilete spores (e.g., *Microbaculispora*), taeniate bisaccate pollen (e.g., *Protohaploxypinus*
522 *samoilovichii*), and non-taeniate bisaccate pollen, to one with a major cavate trilete spore
523 component (most notably, *Densoisporites nejburgii*). Another substantial shift exists between
524 syn-LSTM and post-SSE microfloras, reflected by the absence of overlap in ordination space.
525 This is largely owing to cavate trilete spores losing their overwhelming influence on the

assemblages. Although the post-SSE association skewed toward higher proportions of non-taeniate bisaccate pollen, the large spread of values indicated microfloral composition instability. The column scores (Fig. 5B) indicated that this was largely the result of variable levels of cavate monolete spores (i.e., *Aratrisporites*). There is also an increased input of taeniate bisaccate pollen—a portion of which may be reworked—that resulted in a degree of overlap with the post-EPE association. Finally, the post-EMTE association (Fig. 7A) has a smaller area than that of the preceding post-SSE, and it is almost entirely contained within the post-SSE region. This indicates that similar, but more stable, floral assemblages had established themselves in the Sydney Basin by the early Middle Triassic, with a slightly higher proportion of non-taeniate bisaccate pollen. Correlations with the global chronostratigraphy (Fig. 7C) suggest that the post-EPE palynoflora began at the start of the EPE interval and had a total duration of ~1.7 million years, with the syn-LSTM and post-SSE palynofloras lasting ~0.7 million years and ~2.2 million years, respectively.

DISCUSSION

Timing of Boundaries and Global Climatic Events

The ages we put forward for chronostratigraphic boundaries and climatic events are largely the result of correlating key absolute dating studies (e.g., Metcalfe et al., 2015; Burgess and Bowring, 2015; Fielding et al., 2019; Widmann et al., 2020; Fielding et al., 2021) with globally recognized fluctuations in $\delta^{13}C$ values (Cramer and Jarvis, 2020). The values presented by Cramer and Jarvis (2020) are a composite of various $\delta^{13}C$ measurements done in organic matter ($\delta^{13}C_{org}$) and in inorganic carbonates ($\delta^{13}C_{carb}$), with Triassic data primarily represented by $\delta^{13}C_{carb}$ (Cramer and Jarvis, 2020, p. 331). Although $\delta^{13}C_{org}$ and $\delta^{13}C_{carb}$ do not always match in

549 magnitude (Bachan et al., 2012), they generally exhibit consistent temporal alignments. Notably,
550 for the Smithian-Spathian event (SSE) interval, the P3 positive $\delta^{13}C_{org}$ excursion shows
551 variations in values of a similar magnitude to the $\delta^{13}C_{carb}$ record (Hermann et al., 2011b; Shen et
552 al., 2019). Originally, floristic changes driven by the SSE, along with the P3, were dated to at
553 least 250.55 ± 0.51 Ma (Galfetti et al., 2007b), based on the work by Ovtcharova et al. (2006).
554 However, updated U-Pb age models (e.g., the Permian-Triassic boundary type section at
555 Meishan, China; Burgess et al., 2014) reveal that the older methods for SSE age estimation likely
556 produced large error ranges and overestimated the age values (Condon et al., 2010). More recent
557 radiogenic isotope dating efforts by Widmann et al. (2020) using the EARTHTIME model
558 (Condon et al., 2015; McLean et al., 2015) on the same tuff beds studied by Ovtcharova et al.
559 (2006) enabled direct comparisons of the SSE age estimates to those of the Permian-Triassic
560 (Burgess et al., 2014) and Early-Middle Triassic boundaries (Ovtcharova et al., 2015). The end
561 of the SSE has now been interpreted as occurring between 249.29 ± 0.06 Ma and 249.11 ± 0.09
562 Ma (Widmann et al., 2020), approximately one million years later than previous estimates. If
563 based on astronomical tuning techniques, however, it would be ca. 248.1 Ma (Li et al., 2016;
564 Gradstein et al., 2020; Ogg et al., 2020, p. 927). Hence, the end of the SSE is likely within ca.
565 249.3–248.1 Ma; here, we follow the age-controlled chemostratigraphy presented by Widmann
566 et al. (2020) and place the Smithian-Spathian boundary at ca. 249.4 Ma, the midpoint of the SSE-
567 associated positive $\delta^{13}C_{org}$ excursion (P3). Considering the microfloral data presented herein, the
568 effects manifested by the SSE (e.g., cooling conditions) in the Sydney Basin lasted ~400 k.y.,
569 and only in the latter half (~200 k.y.) did plant communities begin to resemble those of post-EPE
570 times before the late Smithian thermal maximum (LSTM): i.e., a significant representation of
571 arborescent gymnosperms (Fig. 7).

572 The distinctive positive $\delta^{13}C_{org}$ excursion initiating toward the top of the Bald Hill
573 Claystone (upper *A. tenuispinosus* Palynozone) that we have identified as P4 (Fig. 1) should peak
574 after the Early-Middle Triassic boundary (Galfetti et al., 2007a; Ovtcharova et al., 2015; Sun et
575 al., 2021). Radiogenic U-Pb absolute age estimates using the EARTHTIME model provide
576 constraints for the Early-Middle Triassic boundary (=Olenekian-Anisian boundary) in the
577 Sydney Basin (Metcalfe et al., 2015; Fielding et al., 2019, 2021). These suggest the Early-Middle
578 Triassic boundary is present in the stratigraphically short Garie Formation, dated to 248.23±0.13
579 Ma and 247.87±0.11 Ma (Metcalfe et al., 2015). These dates show a considerable discrepancy
580 with the dating provided for various marine deposits of the Early-Middle Triassic boundary. For
581 example, the latest Geologic Time Scale (Ogg et al., 2020, p. 927) considers an even younger
582 Early-Middle Triassic boundary date (ca. 246.7 Ma) based on marine chemo-, bio-, and
583 magnetostratigraphy by Chen et al. (2020). Integrated chronostratigraphic data sets from south
584 China instead provided an estimated age of ca. 247.2 Ma for this boundary (Lehrmann et al.,
585 2015; Ovtcharova et al., 2015), which is favored by the International Commission on
586 Stratigraphy (Cohen et al., 2013, updated). Owing to this absence of clear consensus on the
587 Early-Middle Triassic boundary, we tentatively ascribe the boundary age of 247.2 Ma in the
588 Sydney Basin, as this is closer to the previous minimum age estimate from the same region
589 (247.87 ± 0.11 Ma; Metcalfe et al., 2015).
590 There are important limitations to consider when comparing the durations and
591 magnitudes of carbon isotope excursions, particularly: (1) for continental successions, which are
592 prone to discontinuous deposition, and (2) in the absence of radiogenic age controls. Boundaries
593 without local absolute age controls were the Griesbachian-Dienerian (ca. 251.5 Ma) and the
594 Aegean-Bithynian (ca. 245.0 Ma) substage boundaries. The age ascribed herein for the

595 Griesbachian-Dienerian boundary was based on sediment flux rates (Sanson-Barrera, 2016, chap.
596 3) and Induan astronomical tuning (Li et al., 2016); the Aegean-Bithynian boundary age is
597 supported by ammonoid biostratigraphy, cyclostratigraphy, and magnetostratigraphy (see
598 summary in Ogg et al., 2020, p. 927).
599
600 ***Unconformity in the Lower Induan***
601 The $\delta^{13}C_{org}$ record did not closely match the global signature for the Griesbachian
602 substage (Fig. 1; Ogg et al., 2020, p. 905). Specifically, the N2 negative $\delta^{13}C_{org}$ excursion is not
603 clear in Bunnerong-1 (Fig. 3) nor in Eveleigh-1 (Fig. 4). Biostratigraphically, Mays et al. (2020)
604 reported a single depth for Bunnerong-1 (760.09 m) corresponding to the *Lunatisporites*
605 *pellucidus* Palynozone, inside the Wombarra Claystone. The next sampled depth (745.62 m), in
606 the lower Scarborough Sandstone, is shown to be part of the *Protohaploxypinus samoilovichii*
607 Palynozone. The very small stratigraphic range of this zone in the central Sydney Basin conflicts
608 with its thickness in other parts of the Sydney-Gunnedah-Bowen Basin System, eastern Australia
609 (e.g., >160 m; Foster, 1982). This discrepancy could be owing, in part, to insufficient sampling
610 density in the examined cores, but a sharp contact exists between the Wombarra Claystone and
611 Scarborough Sandstone at 747.16 m depth in Bunnerong-1 and in Eveleigh-1 at 832.32 m (Fig.
612 S5). Although localized circumstances (e.g., vegetation, bacteria) could have potentially resulted
613 in subdued $\delta^{13}C_{org}$ variations in comparison to the global signature, the evidence suggests an
614 unconformity within the Griesbachian (*L. pellucidus* Palynozone) of the Sydney Basin is present,
615 at least in the Central Coalfield.
616
617 **Late Permian to Middle Triassic Floristic Timeline of the Sydney Basin**

Below, the abundance trends of the palynological morphogroups are related to the rich, well-established micro- and macrofossil records of the Sydney Basin. Likely botanical affinities of key spore/pollen taxa are provided in Table 2. A more exhaustive taxon list including less frequent microfloras is provided in Table S5. A recent, Gondwana-wide review of Early to Middle Triassic macrofloral fossil occurrences was conducted by Turner et al. (2024), but without indication of the abundances of each taxon. Here, we summarize the abundances of the most common groups of micro- and macrofossils in the Sydney Basin (Fig. 8).

Uppermost Lopingian Floras and the End-Permian Event (EPE)

The uppermost recorded pre-EPE Lopingian microfloral assemblages were composed predominantly of acavate trilete spores. These include *Horriditriletes* and *Neoraistrickia*—likely derived from Osmundales ferns (de Jersey and Raine, 1990, p. 30–31; Galtier and Taylor, 1994)—and the potentially fern-derived *Microbaculispora*. Common pollen forms included taeniate gymnosperm pollen (e.g., *Protohaploxypinus, Striatopodocarpites*) typical of Glossopteridales (Gould and Delevoryas, 1977; Lindström et al., 1997). The high abundance of the deciduous, peat-forming glossopterids is supported by the macrofloral record of the Sydney Basin (Fig. 8), which shows the last occurrences of assemblages dominated by the leaf-taxon *Glossopteris* and root-taxon *Vertebraria* (Retallack, 1977, 1980; Fielding et al., 2019). Non-taeniate bisaccate pollen were also present (e.g., *Alisporites*), which have been linked to Peltaspermales (Retallack, 2002) and Umkomasiales (=Corystospermales; Osborn and Taylor, 1993; Blomenkemper et al., 2020) seed ferns, and Voltziales conifers (Bomfleur et al., 2013; Nowak et al., 2024)

The <5-m-thick Frazer Beach Member and its equivalents across eastern Australia (McLoughlin et al., 2021) record the continental impacts of the EPE at the high southern latitudes: wetland biotas were destroyed, most likely through some combination of extreme warming and periods of drought (Frank et al., 2021), ozone depletion (Li et al., 2024), widespread wildfires (Vajda et al., 2020; Mays and McLoughlin, 2022) and, possibly, phytotoxic heavy metals (Fielding et al., 2019; Shen et al., 2023; Vajda et al., 2023a; Paterson et al., 2024). When comparing pre-EPE assemblages with those immediately overlying the EPE "dead zone," proportions of taeniate bisaccate pollen (including those produced by glossopterids) were halved, and concentrations of algal remains increased significantly, which likely represented microbial blooms in freshwater ecosystems (Mays et al., 2021a). Although landscapes were essentially depauperate in the "dead zone," leaving a negligible macrofossil record, the intermittent presence of *Alisporites* from the overlying Coal Cliff Sandstone and the prominence of the peltasperm *Lepidopteris callipteroides* from lowermost Triassic strata (Retallack, 1977, 2002) suggest that Peltaspermales were the first gymnosperms that attempted to occupy the devastated landscape following the collapse of glossopterids from the onset of the EPE (ca. 252.3 Ma; Fielding et al., 2019).

Induan Floras

The first appearance of the *Protohaploxypinus microcorpus* Palynozone in the Sydney Basin is less than 100,000 years after the termination of the EPE interval (the upper boundary of which we define at the Permian-Triassic boundary ca. 251.9 Ma; Fig. 8). The early Induan (Griesbachian) microfossil assemblages are typically dominated by filicopsid acavate trilete spores, with *Osmundacidites wellmanii* (Fig. 6T) forming a considerable portion (Fig. 8),

663 followed by *Microbaculispora*. Lycophytic cavate trilete spores (e.g., *Lundbladispora*) were
664 common and *Alisporites* representation surged around this time, potentially tied to the spread of
665 the peltasperm *Lepidopteris callipteroides* (Retallack, 1977, 2002). Taeniate bisaccate pollen
666 typical of glossopterids (e.g., *Protohaploxypinus*) were deposited in significant abundances long
667 after the extirpation of glossopterid-dominated coal measures during the EPE (Fig. 8; Mays et
668 al., 2020). While there is some evidence of this group persisting in Gondwana and elsewhere into
669 the post-EPE interval (e.g., the Karoo Basin, South Africa; Gastaldo et al., 2017), there is an
670 absence of verified glossopterid macrofossils in this interval from eastern Australia (Fielding et
671 al., 2019; see review by Turner et al., 2024). There is also evidence that *Protohaploxypinus* may
672 also derive from other seed fern groups, like peltasperms—a group that includes *Lepidopteris*
673 *callipteroides*, which is well-known from the Lower Triassic of the Sydney Basin (Retallack,
674 2002). This is because *Protohaploxypinus*-type pollen has been identified in pollen sacs
675 associated with *Permotheca* (Gomankov and Meyen, 1986, p. 95; Zavialova and Karasev, 2015),
676 a polliniferous organ connected with *L. callipteroides* (*Permotheca helbyi*; Retallack, 2002).
677 However, in their attempt to emend the diagnosis of *Permotheca*, Foraponova and Karasev
678 (2021) considered *P. helbyi* potentially belonging to the seed ferns *Pteruchus* or *Townrovia*
679 instead, which are not known to produce taeniate bisaccate pollen (Osborn and Taylor, 1993;
680 Bomfleur et al., 2011). Hence, we tentatively attribute the persistence of these pollen forms in
681 Induan strata of the Sydney Basin to: (1) potential reworking (e.g., from the underlying Illawarra
682 Coal Measures), which can be a major contributor to a palynological assemblage under some
683 conditions (e.g., Moss et al., 2005; Gastaldo, 2012; Lopes et al., 2014); (2) an affinity to a
684 presently unknown non-glossopterid gymnosperm; and/or (3) an unverified relictual population
685 of glossopterids.

686 The *P. microcorpus* Palynozone lasted ~100,000 years in this region until different plants
687 became commonplace (ca. 251.8 Ma). At this point, microfloras from the *Lunatisporites*
688 *pellucidus* Palynozone appear and surge in abundance, such as the conifer pollen *Lunatisporites*
689 (Nowak et al., 2024) and the pleuromeiacean spore *Densoisporites nejburgii* (Grauvogel-Stamm
690 and Lugardon, 2004). The macrofloras also reflected this change (Retallack, 1977; Mays et al.,
691 2020), which are characterized by abundant conifers (e.g., *Voltziopsis africana, Podozamites*)
692 and *Isoëtes*-like lycophytes, in addition to equisetaleans (e.g., *Schizoneura gondwanensis*) and
693 *Cladophlebis*-like fern fronds. Some elements of this palynozone appear to have migrated from
694 the north (e.g., *Limatulasporites*, of probable bryophytic affinity; McLoughlin et al., 1997),
695 which made its first appearance in this palynozone in the Sydney Basin, but in the underlying *P.*
696 *microcorpus* Palynozone of the Bowen Basin (Price, 1997, p. 157). This, however, does not
697 preclude the migration of other floras to the Sydney Basin from the south or on a longitudinal
698 gradient, but could be owing to diachronous first appearances for individual taxa (Lindström and
699 McLoughlin, 2007; Barbolini et al., 2016). The base of the *L. pellucidus* Zone coincided with the
700 cessation of the N1 negative $\delta^{13}C$ excursion (Fig. 1) and the final phase of a global warming
701 trend, which initiated at the onset of the EPE (Sun et al., 2012).
702 The general trend across the Dienerian (late Induan) hints toward a steady relative
703 decrease of non-taeniate bisaccate pollen, *Alisporites* included. This is reflected by the reduction
704 of peltasperm macrofossils (Fig. 8), likely because of the spread of voltzialean forests across the
705 Sydney Basin (Retallack, 1977). Persistently low abundances of charcoal occur within the
706 palynozone, possibly indicating low-density, sclerophyllous open vegetation throughout this time
707 (Retallack, 2019) limiting the spread of wildfires (Mays and McLoughlin, 2022).
708

Olenekian Floras

Forests of voltzialean conifers continued to dominate the landscape for most of the *Protohaploxypinus samoilovichii* Palynozone (Fig. 8). However, warming and other climatic changes (Retallack, 2013) likely led to their decline during the LSTM (ca. 250.3–249.6 Ma) as demonstrated by their associated *Lunatisporites* taeniate bisaccate pollen dwindling in the microfossil record during this interval. Their fall might have facilitated the further spread of already-thriving Pleuromeiaceae lycophytes (e.g., *Pleuromeia, Cylomeia*), which is shown by abundant fossil evidence of *Densoisporites* spores and other pleuromeian-associated macrofossils, such as leaves/microphylls (Mays et al., 2020; Vajda and Kear, 2024), corms (Vajda and Kear, 2024), and strobili (Retallack, 1975, 1977).

Following the LSTM (uppermost *P. samoilovichii* Palynozone, ca. 249.4 Ma), umkomasialean seed ferns grew to dominate the formerly isoëtalean landscape (Fig. 8). This is evidenced by near-monospecific beds of *Dicroidium zuberii* (interpreted as "*Dicroidium* heaths" by Retallack, 1980, p. 418) and associated increases in pollen of umkomasialean affinity, namely *Alisporites* and *Pteruchipollenites* for ~200 k.y. This transition coincided with the prominent P3 positive $\delta^{13}C$ excursion (Fig. 1), which has been linked to global cooling conditions present during the SSE (Widmann et al., 2020). According to Retallack (1977), this *Dicroidium*-dominated ecosystem included other accessory taxa, such as: (1) *D. narrabeenense* and *D. odontopteroides* (= *lancifolium*, Anderson and Anderson, 1983; see Holmes and Anderson, 2005b, p. 6–7); (2) peltasperms, especially *Lepidopteris*, and the possible peltasperm *Pachydermophyllum* (Elgorriaga et al., 2019); (3) *Taeniopteris* (*incertae sedis*); (4) equisetaleans (notably *Neocalamites*); and (5) rare ferns of probable osmundaceous affinity (e.g., *Cladophlebis*). While *Dicroidium* (Umkomasiales) first appeared in the Lopingian at the low- to

mid-latitude Gondwanan regions of Jordan and Pakistan (Kerp et al., 2006; Abu Hamad et al., 2008, 2017; Bomfleur et al., 2018), they only migrated southward after the EPE (Retallack, 1977; Anderson and Anderson, 1983; Bomfleur et al., 2018). The first known occurrence of *Dicroidium* in Bunnerong-1 (and potentially in the Sydney Basin) is at a depth of 587.47 m in the lower Bulgo Sandstone (Fielding et al., 2019, their fig. 2; Mays et al., 2020), indicating their arrival around the beginning of the Olenekian, during the earliest Smithian (ca. 251.1 Ma). This suggests that umkomasialean floras were already present in the Sydney Basin ~2 million years before their upsurge during the SSE (Fig. 8). However, this SSE-linked, *Dicroidium*-dominated flora did not persist as long as the voltzialean flora that preceded it. Once the SSE terminated (ca. 249.2 Ma), umkomasialean seed fern forests appeared to have decreased in dominance, giving way to a resurgence of isoëtaleans, namely Isoëtaceae (e.g., *Tomiostrobus*; Retallack, 1997; Holmes and Anderson, 2022).

This return of isoëtaleans characterized the early parts of the Spathian substage (ca. 249.2–248.7 Ma) and is marked by the appearance of the *Aratrisporites tenuispinosus* Palynozone in the Bald Hill Claystone (Fig. 8). Although not as dominant, the palynological evidence suggests Umkomasiales remained relatively common in the basin, alongside Isoëtales throughout the entire substage. Midway through this palynozone (ca. 248.0 Ma), a proportional increase in conifer-associated taeniate bisaccate pollen is noted (Figs. 3 and 4). Retallack (1980, p. 389 and 417) considered this a reflection of resurgent coniferous floras in the Sydney Basin at that time (represented by the Bald Hill Claystone). We found, however, that: (1) the taeniate bisaccate pollen present in the Bald Hill Claystone are of the same type as those seen in the Bulgo Sandstone (i.e., *Lunatisporites noviaulensis* and *L. pellucidus*), being potentially reworked from older sediments (Fig. S4), and (2) while conifer shoots were present in Bunnerong-1, the

most common macrofossils for this formation were umkomasialean seed fern leaves of *Dicroidium* (Fielding et al., 2019; Vajda and Kear, 2024), which are contemporaneous with well-preserved specimens of associated microfloras (*Alisporites australis*; Fig. 5D). Therefore, our results do not corroborate that a return of conifers transpired, at least for the central part of the Sydney Basin.

Anisian Floras

The Early-Middle Triassic boundary (ca. 247.2 Ma) is marked by the P4 positive $\delta^{13}C$ excursion (Fig. 1), which has been linked to cooling associated with the Early-Middle Triassic event (EMTE; see Sun et al., 2012; Trotter et al., 2015). In the Sydney Basin, the onset of the Anisian Stage coincided with a lithological change from red bed facies to the dark gray mudrocks of the thin Garie Formation, and the beginning of the *Aratrisporites parvispinosus* Palynozone. Levels of total organic carbon began to increase for the first time since the EPE, albeit modestly (Figs. 3 and 4), and floral assemblages changed. Notably, there is a temporary decline in isoëtalean spores and a rebound of non-taeniate bisaccate pollen of probable umkomasialean affinity at the end of the EMTE interval. This latter change is reflected by the macrofossil assemblages of lower Anisian age (Newport Formation and lateral equivalents), which reveal umkomasialeans as the primary group of arborescent plants (Fig. 8), as noted by the increased abundance of *Dicroidium zuberii*, along with several other *Dicroidium* leaf taxa (Retallack, 1977). Pleuromeian leaves and strobili (i.e., *Cylostrobus sydneyensis*) are also still present (Retallack, 1980). Accessory fossils include: (1) the equisetaleans *Neocalamites* and *Schizoneura*; (2) the ferns *Cladophlebis* (?Osmundales), cf. *Todites* (?Gleicheniaceae), and *Asterotheca* (Marattiales); (3) the peltasperm *Lepidopteris* and the possible peltasperm

778 "*Odontopteris"* and *Taeniopteris* (*incertae sedis*); and (4) minor abundances of the conifer
779 *Voltziopsis*.
780 The uppermost interval examined herein was the Bithynian substage (lower middle
781 Anisian). Shale lenses within the Hawkesbury Sandstone indicated that the Sydney Basin
782 continued to be dominated by *Dicroidium* (primarily *D. zuberii*), but now accompanied by leaves
783 of the probable umkomasialean cf. *Xylopteris* (Retallack, 1980). By the time the lower
784 Hawkesbury Sandstone was buried, the abundances of the most common representative of the
785 Pleuromeiaceae in the Lower Triassic of the Sydney Basin (*Densoisporites nejburgii*) had
786 become negligible. This is concurrent with the decline of *Pleuromeia* and its associated
787 macrofossils during the Middle Triassic (Retallack, 1977). Moreover, non-bisaccate pollen
788 became more prevalent in the microfossil assemblages, including monosaccate (e.g.,
789 *Striomonosaccites morondavensis*), colpate (e.g., *Cycadopites follicularis*), and polyplicate (e.g.,
790 *Praecolpatites* sp. cf. *P. sinuosus*). Throughout the rest of the Anisian (Bithynian-Illyrian), the
791 region was dominated by diverse *Dicroidium* floral communities, although *D. zuberii* was
792 gradually supplanted by *D. odontopteroides* by the latest Anisian/?lower Ladinian (Wianamatta
793 Group; Retallack, 1980). Non-umkomasialean fossils included ginkgophytes (e.g.,
794 *Sphenobaiera*) and liverworts (e.g., *Marchantites cyathoides*; Retallack, 1980). The apparent
795 increase in pollen diversity by the early Middle Triassic (Anisian) is reflected in the macrofloral
796 record across eastern Australia, which shows rising species richness, particularly among
797 umkomasialeans (Holmes, 1982, 1987; Holmes and Anderson, 2005a; see review by Turner et
798 al., 2024), peltaspermaleans (Holmes, 1982; Holmes and Anderson, 2005b), cycadaleans
799 (Holmes and Anderson, 2008), and ginkgoaleans (Holmes and Anderson, 2007).
800

The Two Primary Drivers of Early Triassic Floristic Changes at High Southern Latitudes

The LSTM and the SSE were two pivotal events that substantially influenced plant communities worldwide (see "Floristic Timeline Comparisons" section). As visualized in nMDS ordination for the Sydney Basin (Fig. 7), these occupy distinct regions in ordination space, reflecting major compositional differences in the assemblages before and after each event. Moreover, their large areas in ordination space suggest that the floristic variability during these events was far greater than that following the final climatic transition examined herein: the EMTE. The nMDS analysis showed only a general contraction in ordination space between pre- and post-EMTE assemblages, suggesting a floristic stabilization. The floristic signatures of the two dominant drivers of Early Triassic ecosystem changes (LSTM and SSE) are discussed in the following section.

The Late Smithian Thermal Maximum

The LSTM marks a significant transition in the Early Triassic microfloral assemblages of the Sydney Basin. In the nMDS analysis (Fig. 7A), the LSTM is clearly distinct from the preceding floras in the region, which is driven by an acme of cavate trilete spores, mainly *Densoisporites* (particularly *D. nejburgii*). This microfossil trend is supported by the macrofossil record (Fig. 8), which shows that their producers *Pleuromeia* (and associated organ taxa)—which have been consistently linked to *Densoisporites* (Balme, 1995, p. 104–107; Grauvogel-Stamm and Lugardon, 2004; see review by Looy et al., 2021)—was the predominant floral group in the region during the middle Early Triassic (Retallack, 1975, 1997). These findings contribute to the existing evidence of the success isoëtalean lycophytes enjoyed following the end-Permian biotic crisis (Retallack, 1997; Looy et al., 2021). However, while global hyperthermal conditions

824 concurrent with the LSTM (Sun et al., 2012; Widmann et al., 2020; Du et al., 2022) appear to
825 mark a global acme of isoëtalean-dominated palynofloras, their rise was not globally
826 synchronous (see "Generalized Global Trends" section).
827 Further support for a climatic driver behind floral transition comes from the plants
828 themselves; *Densoisporites*-affiliated pleuromeians (e.g., *P. sternbergii*)—similar to their nearest
829 extant relatives (i.e., *Isoëtes*; Keeley, 1998)—probably had remarkable tolerance to stress and
830 flourished in the absence of competitors (Looy et al., 2021). This may explain the (near-
831)monogeneric pleuromeian plant assemblages following the latest Permian (e.g., Feng et al.,
832 2020) and Early Triassic (e.g., Naugolnykh, 2013a) hyperthermal events. However, the specific
833 climate-related ecosystem stressors that promoted their proliferation remain to be identified.
834 While increased temperatures have been indicated (Romano et al., 2013; Goudemand et al.,
835 2019), other proximate environmental related stressors may have played greater roles (e.g.,
836 precipitation seasonality, soil nutrient depletion). Although the abundances of some plant
837 macrofossil groups in the Sydney Basin (i.e., *Dicroidium, Lepidopteris, Voltziopsis*) undergo
838 drastic reductions during the LSTM, none entirely disappear (Fig. 8). This may not be the case
839 for rarer, poorly represented taxa (Table S5). While these abundances are suggestive of major
840 reductions of these plant groups in the late Smithian landscape, the macrofloral records may be
841 influenced by local taphonomic biases, which would limit their utility for gleaning regional floral
842 signals. Hence, a systematic, quantitative assessment of all taxa would need to account for
843 absolute diversity and abundance variations within the LSTM interval.
844
845 ***The Smithian-Spathian Event***

The SSE represents the second major event driving significant change in Early to Middle Triassic floral assemblages within the Sydney Basin. This shift is reflected by the clear differentiation of pre- and post-SSE microfloral assemblages in ordination space (Fig. 7), which is largely owing to the replacement of the dominant spore types: from cavate trilete *Densoisporites* spores (pre-SSE) to cavate monolete *Aratrisporites* spores (post-SSE). Both groups were present in the region before and after the SSE (Fig. 8), so the influx of *Aratrisporites* cannot be explained by its novel introduction. Instead, their near-mutually exclusive relative abundances over time (Figs. 3 and 4) would seem to indicate a change in the regional conditions that favored *Aratrisporites*-producing isoëtaleans over *Densoisporites*-producing isoëtaleans. Expanding on the generalized palynology-climate model of Visscher and van der Zwan (1981), Hochuli and Vigran (2010) interpreted *Densoisporites* (*D. nejburgii*, in particular) as xerophytic (dry-adapted), and *Aratrisporites* as hygrophytic (wet-adapted). The co-occurrence of the *Aratrisporites* (Isoëtaceae) acme with the onset of red beds might therefore indicate major precipitation changes in the Sydney Basin during the post-SSE warming interval. Conversely, the cessation of red mudrock strata concurrent with a decrease in *Aratrisporites* (ca. 247.2 Ma; Fig. 8) seems to be linked to the global cooling experienced during the EMTE. However, at present, there are no clear climatic inferences that can be made from the presence of such red mudrock facies, since non-climatic factors may play a larger role in their formation (Sheldon, 2005; Li et al., 2017). Moreover, the *Aratrisporites* acme might not be consistently linked with red bed deposition, as Herbert (1997) highlights the transgressive and diachronous nature of red beds throughout the Early Triassic in the Sydney Basin. Undoubtedly, the specific climatic conditions and the tolerances of their associated isoëtalean groups in the Sydney Basin during these events remain an open question.

Cooling during the SSE likely facilitated the resurgence of gymnosperm forests in the latter phase of the event (ca. 249.4–249.2 Ma). This is evident from the increased abundances of non-taeniate bisaccate pollen, primarily *Alisporites* (Fig. 8). The influence of gymnosperms is reflected by the nMDS analysis (Fig. 7), which shows that the abundances of non-taeniate bisaccate pollen is a principal factor in differentiating pre- and post-SSE assemblages (in addition to the different groups of isoëtaleans, as outlined in the previous paragraph). The macrofloras of this interval exhibit a similar transition (Fig. 8): from isoëtalean-dominated lycophytic assemblages (e.g., *Cylostrobus, Pleuromeia*) to one dominated by umkomasialeans (e.g., *Dicroidium zuberii*). Peltasperms, represented by *Lepidopteris* leaf remains, disappear from the Bunnerong-1 core shortly after the cessation of the SSE (Fielding et al., 2019; Mays et al., 2020). Since peltasperms are another potential producer of *Alisporites*-type pollen (Retallack, 2002), their absence from the macrofloral record in the Central Coalfield soon after the SSE (ca. 249.1 Ma) indicates that the increase in *Alisporites* was almost certainly due to the rise of umkomasialean seed ferns.

These umkomasialean forests briefly flourished within the basin for ~200 k.y., until temperatures began to rise once again (Fig. 8). However, unlike during the LSTM, gymnosperms did not experience a collapse to the same extent, as their pollen and macrofossil remains have been commonly observed throughout the relatively stable Spathian substage, before reemerging as dominant following the EMTE. The significance of the post-EMTE rise of *Dicroidium* is reflected in the Triassic coal measures of Gondwana, in which *Dicroidium* is typically the primary coal-forming plant. The first post-EPE coal measures reappear in the global rock record during the Middle Triassic (Retallack et al., 1996)—such as the ?late Anisian, *Dicroidium*-dominated Nymboida Coal Measures of eastern Australia (Retallack et al., 1993; Wells, 1995;

892 Holmes, 2000)—indicating a return of terrestrial wetland carbon sinks after >8 million years. We
893 therefore interpret that the major climatic fluctuations of the Early Triassic, specifically those
894 linked to the LSTM and SSE, were principal causes behind this delay.
895
896 **Floristic Timeline Comparisons**
897 To provide context of how the LSTM and SSE impacted floras beyond the Sydney Basin,
898 here we compare the responses of other age-controlled sites and their quantitative floristic
899 records with the eastern Australian floral communities (Fig. 9). Due to the paucity of well-
900 studied Lower to Middle Triassic continental records at present, most localities compared here
901 do not strictly reflect continental systems, as in the case for the Sydney Basin, which might result
902 in certain microfloras being under- or overrepresented (see Traverse, 2007, chap. 18.2).
903
904 ***Tulong, Tibet (Northern Gondwana; Paleolatitude: ~45°S)***
905 Tulong, situated in present-day southern Tibet, holds a fossil-rich stratigraphic record
906 spanning the Permian to Upper Triassic (Brühwiler et al., 2009; Schneebeli-Hermann et al.,
907 2012a; Peng et al., 2019; Liu et al., 2020). Here, the LSTM and SSE are captured within Unit III
908 and Unit IV of the nearshore Kangshare Formation (Fig. 1). Similar to the Sydney Basin (Fig. 9),
909 cavate trilete spores were common throughout the Smithian and early LSTM, with
910 *Densoisporites* comprising ~40% of the assemblage in this interval (Schneebeli-Hermann et al.,
911 2012a).
912 During the late LSTM and SSE, a marine transgression led to the deposition of limestone,
913 interbedded with small shale lenses. These shales predominantly contained lycophytic spores of
914 *Endosporites papillatus* (~70%; Peng et al., 2019), which have been considered potentially

915 degraded forms of *D. nejburgii* (Grauvogel-Stamm and Lugardon, 2004). In contrast to the
916 Sydney Basin (Fig. 9), gymnosperm bisaccate pollen did not increase during the SSE but
917 afterward, during early Spathian warming (Schneebeli-Hermann et al., 2012a). Additionally,
918 while *Densoisporites* experienced a post-SSE increase in Tulong, this was not observed in the
919 Sydney Basin. In both regions, however, it became rare during the Spathian and negligible after
920 the EMTE.
921
922 ***Salt-Surghar Ranges, Pakistan (Northern Gondwana; Paleolatitude: ~35°S)***
923 The Salt-Surghar Ranges, located in Punjab, Pakistan, stand out as one of the most
924 intensely studied succession among those compared (Hermann et al., 2011a, 2011b, 2012;
925 Schneebeli-Hermann et al., 2012b, 2015; Schneebeli-Hermann and Bucher, 2015; Schneebeli-
926 Hermann, 2020; Galasso et al., 2022). Its Early-to-Middle Triassic floras were formed under
927 shallow marine conditions and chronicle the floral changes occurring at the northern Indian
928 margin. The immediate post-EPE flora showed common (10%–20%) gymnosperm pollen,
929 similar to the Sydney Basin. *Densoisporites* surged to 60% of the assemblage during the lowest
930 Dienerian in the Salt-Surghar Ranges, maintaining a common presence (~30%) alongside
931 *Lundbladispora* throughout the Dienerian and up to the middle Spathian. While in the Sydney
932 Basin, *Lundbladispora* displayed a similar trend, *Densoisporites* only reached comparably high
933 abundances ~1.3 million years later (middle Smithian).
934 The LSTM record, as preserved within the Upper Ceratite Limestone (Fig. 1), is
935 analogous to the Sydney Basin, reflecting a surge in *D. nejburgii* and *D. playfordii*, with
936 *Densoisporites* collectively constituting up to 90% of the microfloral assemblages (Hermann et
937 al., 2012; Schneebeli-Hermann, 2020). This dominance persisted until the SSE, during which

938 *Densoisporites* and other cavate trilete spores declined in both the Salt-Surghar Ranges and
939 Sydney Basin (Fig. 9). Although both regions experienced a surge in gymnosperm pollen during
940 the latter half of this event, taeniate bisaccate pollen became predominant in the Salt-Surghar
941 Ranges, while non-taeniate bisaccate pollen was more common in the Sydney Basin. After the
942 SSE, gymnosperm pollen lost their dominance in both regions, but with non-taeniate bisaccate
943 pollen remaining common during the Spathian. In the Salt-Surghar Ranges, *Densoisporites* was
944 the most prevalent microfloral element in the post-SSE Niveaux Intermédiaires interval (early-
945 to-middle Spathian), whereas in the Sydney Basin it was rare, with *Aratrisporites* being the most
946 common group instead (Hermann et al., 2012; Schneebeli-Hermann, 2020).
947 During the EMTE, *Densoisporites* became rare in both regions, and non-taeniate
948 bisaccate pollen reached abundances similar to those observed during the SSE (Schneebeli-
949 Hermann, 2020).
950
951 ***Greenland (Angara; Paleolatitude: ~40°N)***
952 Peary Land, situated in northern Greenland, contains a shallow marine record from the
953 late Smithian to early Anisian (Lindström et al., 2020). Combining these data with the rich
954 information for Induan floras gathered from similarly shallow marine successions in Jameson
955 Land, eastern Greenland (Looy et al., 2001; Visscher et al., 2004; Hochuli et al., 2010b, 2016;
956 Sanson-Barrera, 2016), enabled a near-complete, composite timeline of plant community
957 changes in the Northern Hemisphere mid-latitudes from the latest Permian to Middle Triassic.
958 In eastern Greenland, the post-EPE Griesbachian interval presents a markedly different
959 pattern from that of the Sydney Basin. Here, taeniate bisaccate pollen (e.g., *Lunatisporites*)
960 dominated the microflora, accounting for 30%–70% of the assemblage, while cavate trilete

961 spores increased to ~40% from less than 5% in the late Permian. This gymnosperm dominance
962 was disrupted at the Griesbachian-Dienerian boundary (Hochuli et al., 2016), as lycopsid cavate
963 trilete spores surged to 90% during the Dienerian. In contrast, the Sydney Basin maintained a
964 stable, gymnosperm-dominated microflora across the Griesbachian-Dienerian boundary and
965 throughout the Dienerian (Fig. 8). In Greenland, however, a gap in the record between the late
966 Dienerian and middle Smithian may obscure any potential rebound of gymnosperms following
967 Dienerian cooling (Fig. 9).
968 During the LSTM, spores accounted for ~80% of the microfloral assemblages in northern
969 Greenland, with *D. nejburgii* accounting for 30% (Lindström et al., 2020), whereas in the
970 Sydney Basin spores reached even higher proportions (averaging ~60%). The SSE triggered a
971 sharp decline in spore proportions in both regions, with *D. nejburgii* dropping to <1% in northern
972 Greenland, and bisaccate pollen surging to 90% of the assemblage (compared to an average of
973 ~36% in the Sydney Basin). While gymnosperm pollen remained more prevalent during the
974 middle-to-late Spathian in northern Greenland, bisaccate pollen dominated in the Lower Anisian
975 of both sites, including during the EMTE (Lindström et al., 2020).
976
977 ***Barents Sea (Angara; Paleolatitude: ~45°N)***
978 The Barents Sea succession of palynological assemblages comprises two proximal
979 localities: (1) Spitsbergen (Permian to Griesbachian), of the Svalbard archipelago (Galfetti et al.,
980 2007b; Hochuli and Vigran, 2010; Hochuli et al., 2010a; Leu et al., 2024), and (2) Svalis Dome
981 (Smithian to Anisian) in the southwestern Barents Sea, near Norway (Mangerud, 1994; Vigran et
982 al., 1998). Collectively, the assemblages from these marginal marine paleoenvironments
983 represent the northernmost extent of Early Triassic floristic data discussed here (Fig. 9).

During the EPE, the abundances of taeniate and non-taeniate bisaccate pollen became uncommon (from ~65% to <10%) and an abundance spike in lycophyte cavate trilete spores occurred (>50%; Hochuli et al., 2010a), in contrast to the Sydney Basin, which did not experience either. Comparable to the Sydney Basin, gymnosperms returned during the post-EPE interval of Spitsbergen, comprising over 50% of microfloral assemblages in the early Griesbachian. No detailed data are available from this region between the Dienerian to mid-Smithian until the LSTM interval captured from the Svalis Dome (Galfetti et al., 2007b; Hochuli and Vigran, 2010).

During the LSTM, as in the Sydney Basin, bisaccate pollen became rare, with lycophytic spores making up ~60% of microfossil assemblages, and *Densoisporites nejburgii* accounting for 20% of the total (Galfetti et al., 2007b). A distinctive feature in the Barents Sea region, compared to other localities, was the rise of the non-bisaccate pollen *Cycadopites* to around 25% before the commencement of the SSE.

Similar to the Sydney Basin, gymnosperm pollen increased during the SSE, but both taeniate and non-taeniate bisaccate pollen rose in the Barents Sea region from negligible abundances to ~30% each, with coeval decreases of *D. nejburgii* to <5% in both the Sydney Basin and the Barents Sea.

Toward the EMTE (Fig. 9), cavate trilete spores (e.g., *D. nejburgii*) became rare, with non-taeniate and taeniate bisaccate pollen becoming increasingly common, alongside *Aratrisporites* and, in the Barents Sea, *Cycadopites*. In the Anisian, both regions show *Aratrisporites* remaining prevalent, and gymnosperms—which were increasingly represented by non-taeniate bisaccate pollen in the Barents Sea—reached up to 70% of the assemblage there; their high abundances persisted into the subsequent Ladinian (Hochuli and Vigran, 2010).

Other Localities

Lower Triassic plant communities are reported from several other localities around the world (see fig. 8 in Lindström et al., 2020; Turner et al., 2024). Above, we outlined the floristic trends from the successions with age-controlled, long-term palynological data to enable comparisons with the Sydney Basin. We did not discuss in detail several other localities that record some or all of the target interval but are of interest due to their potential for further comparisons (Fig. 2A). These include, from south to north: Antarctica, particularly the Alan Hills in the Transantarctic Mountains (Awatar et al., 2014; Valentina, 2021) and the Lambert Graben in the Prince Charles Mountains (Lindström et al., 1997; McLoughlin et al., 1997); the Godavari Graben in southern India (Jha et al., 2011, 2012; Jha and Aggarwal, 2012); south China (Feng et al., 2020; Shu et al., 2023); north China (Xu et al., 2022; Hua et al., 2023); Hungary (Looy et al., 1999); and Germany (Kürschner and Herngreen, 2010; Scholze et al., 2017).

Generalized Global Trends

Plant fossil records reveal major changes in floral community compositions due to impactful global climatic events during the late Permian to Middle Triassic (Fig. 9), without the same degree of species extinction seen in coeval animal fossil records (McElwain and Punyasena, 2007; Cascales-Miñana and Cleal, 2014; Nowak et al., 2019; Xiong et al., 2021). Although we cannot assume the predicted behavior of plants under climatic changes, here we consider that the survival of certain groups was principally the result of physiological traits that promoted resilience to stress and/or latitudinal and altitudinal migration. The largest degree of floral change in the Early Triassic occurred during the LSTM (ca. 250.3–249.6 Ma). At all

regions compared herein, landscapes remained or became dominated by associations of cavate trilete spore-producing plants. The overwhelming majority of these are *Densoisporites*-producing pleuromeian isoëtaleans. While the environmental implications of this group have long been discussed (Retallack, 1997; Grauvogel-Stamm and Ash, 2005), it is likely that at least some pleuromeian species were adapted to intervals of enhanced environmental stress. For instance, the physiology of *Pleuromeia sternbergii*—linked with its living relative *Isoëtes* (Keeley, 1998)—indicates it was a slow-growing but hardy plant, capable of withstanding environmental extremes at the expense of its competitors (e.g., intermittent flooding/drying; Looy et al., 2021).

In the Sydney Basin (Fig. 8), the increase of *D. nejburgii* during the LSTM does not coincide with the prevalence of basin-wide, oxidized iron-rich mudrock red beds, which appear earlier in the stratigraphic column in other parts of the basin (Herbert, 1997). This facies is suggestive of major changes in precipitation regime and/or water table levels, although the specific conditions these strata represent remain unclear. Therefore, the surge of likely xerophytic Pleuromeiaceae isoëtalean plants cannot be entirely explained by regional red bed deposition, but instead owing to global climatic shifts. The LSTM interval also yielded lower-than-usual proportions in phytoclasts (Figs. 3 and 4), suggesting a landscape depauperate of woody remains. The relatively sparse vegetation of the region (Mays and McLoughlin, 2022) would have favored the proliferation of pioneering pleuromeians by virtue of less competition.

The rise of isoëtalean lycophytes seems to have occurred asynchronously across the globe. At the low- to mid-latitudes (~35°–45°), *Densoisporites* became the most abundant group during (or at the end) of the early Early Triassic (late Induan; ca. 251.5–251.2 Ma; Hermann et al., 2011a, 2012; Schneebeli-Hermann et al., 2012b; Lindström et al., 2020). However, this group did not rise to dominance until the LSTM at the high southern latitudes, approximately one

million years later (ca. 250.2 Ma; this study, see Fig. 8). Further support for this diachronous, low-to-high latitudinal expansion of isoëtaleans comes from paleoequatorial south China, where near-monotypic isoëtalean macrofloral assemblages occur in the immediate aftermath of the EPE (ca. 252.2 Ma; Feng et al., 2020), approximately two million years before their rise in the Sydney Basin. This progressive emergence is complicated by the fact that different isoëtalean groups occur at the various Early Triassic localities: in China, the dominant isoëtaleans are associated with *Aratrisporites*-type spores and interpreted as isoëtacean (Feng et al., 2020), while *Densoisporites*-type cavate trilete spores of probable pleuromeiacean isoëtaleans appear in greater abundance elsewhere (summarized in Fig. 9). A greater understanding of the environmental preferences for these discrete isoëtalean groups is needed before the full implications can be drawn. Regardless, the delayed gymnosperm-to-pleuromeian overturn in the Sydney Basin palynofloras seems to suggest that benign conditions—or milder climate—post-EPE persisted longer at the southern high latitudes than at lower latitude regions of Gondwana (e.g., Bomfleur et al., 2018). The worldwide acme of pleuromeiacean-derived *Densoisporites* that occurred around the start of the LSTM that lasted until the midpoint of the SSE is corroborated by the macrofossil record of the Sydney Basin, where *Pleuromeia* and its lycophytic allies *Cylomeia* (=*Cyclomeia*) are found alongside rare gymnospermous floras (*Dicroidium zuberii*) in the upper Bulgo Sandstone (Vajda and Kear, 2024). *Densoisporites* did not experience a resurgence after the SSE in the Sydney Basin (Fig. 8), a trend not observed in other Gondwanan regions, such as the Salt-Surghar Ranges, Pakistan (Schneebeli-Hermann, 2020), and Tulong, Tibet (Schneebeli-Hermann et al., 2012a; Peng et al., 2019). Therefore, not only was the rise of pleuromeians apparently delayed at the southern polar regions, but it was relatively short-lived (~800 k.y.).

The cooling interval concurrent with the SSE (ca. 249.6–249.2 Ma) likely allowed gymnosperms to regain their foothold. For example, forests of umkomasialean seed ferns became predominant for ~200 k.y. in the Sydney Basin (Fig. 8). That is, until isoëtalean lycophytes once more became the dominant plant group—but this time represented in the palynofloral record by *Aratrisporites*—for an additional two million years. Unlike the middle-to-late Smithian interval, Spathian climates were stable enough to maintain umkomasialean seed ferns forests, as shown by their macrofossil remains being regularly found alongside *Aratrisporites*-producing isoëtaleans (e.g., *Cylostrobus, Tomiostrobus*; Retallack, 1997). Umkomasialeans ultimately rose to persistent prominence in the Sydney Basin during the EMTE (ca. 247.2 Ma). Worldwide, the SSE appears to have resulted in an increase of bisaccate pollen-producing gymnosperms (Fig. 9), with their proportions never consistently dropping to as low as during the LSTM (when they were often <5%) and further increasing following the EMTE (Hochuli and Vigran, 2010; Peng et al., 2019; Lindström et al., 2020; Schneebeli-Hermann, 2020). Considering that gymnospermous floras did not constantly remain the dominant elements in landscapes following the SSE, the SSE itself should not be regarded as the sole recovery phase, but rather a necessary step in an almost 3-m.y.-long process of staggered ecosystem reestablishment between the LSTM (ca. 250.2 Ma) and the EMTE (ca. 247.2 Ma), that culminated in these plants dominating Mesozoic landscapes thereafter.

CONCLUSIONS AND SYNTHESIS

Primary Conclusions

1. The Sydney Basin provides a high southern paleolatitudinal record of plant community responses to major climatic events of the late Permian to Middle Triassic.

2. The distinctive signature of organic carbon isotope excursions for this interval provided the floristic timeline with precise correlations to the global chronostratigraphy.
3. The pivotal drivers behind Early Triassic ecosystem shifts, and the transition between landscapes dominated by gymnosperms or lycophytes, are the late Smithian thermal maximum (LSTM, ca. 250.3–249.6 Ma) and the Smithian-Spathian event (SSE, ca. 249.6–249.2 Ma).
4. The LSTM allowed the dominance of opportunistic pleuromeian lycophytes (e.g., *Pleuromeia*) for ~800 k.y., while SSE cooling enabled gymnosperm forests, led by umkomasialean seed ferns, mostly *Dicroidium*, to become established for ~200 k.y.
5. The post-SSE Early Triassic saw a mix of seed fern gymnosperms and lycophyte floras for ~2 million years until the Early–Middle Triassic Event (EMTE, ca. 247.5–247.0 Ma), after which Umkomasiales-dominated seed fern forests become dominant and stable for several million years thereafter.
6. On a global scale, floral recovery was staggered and diachronous with latitude, reflecting distinct regional climatic controls on floral responses to these major climatic events.

The presented data corroborates the first hypothesis, which stated that Early Triassic polar gymnosperm forest communities were severely impacted by global climatic events. Regarding the second hypothesis—that these communities experienced quicker recoveries following hyperthermal events (relative to those of lower latitudes)—we found that this was indeed the case following the end-Permian event (EPE, ca. 252.3–251.9 Ma); however, following the LSTM (hence, during the SSE), global gymnosperm floras appear to have returned almost simultaneously around the world ca. 249.4 Ma.

Synthesis

The Early Triassic floristic trends in the Sydney Basin align broadly with global patterns while exhibiting distinct regional characteristics. The iconic Gondwanan *Glossopteris* seed fern flora collapsed simultaneously during the EPE across eastern Australia, including the Sydney Basin. The prominence of pleuromeian lycophytes during the LSTM underscores their resilience to hyperthermal conditions; however, their significant rise at polar latitudes was delayed ~1.7 million years later than equatorial regions. The SSE and EMTE facilitated a resurgence of gymnosperm-dominated ecosystems, signaling that cooling phases were a critical component that allowed their reestablishment. Gymnosperm populations, although greatly impacted by hyperthermal intervals, likely persisted in refugia (e.g., distal or upland areas) before recolonizing landscapes by outcompeting the reigning opportunistic lycophytic floras during cooling intervals.

The recovery of terrestrial ecosystems following their end-Permian collapse was a staggered process that occurred over a span of several million years in response to variable climate, rather than being linked to any single "event." The rise-to-dominance of iconic Mesozoic gymnosperm groups, some of which first appeared in the Permian, represents the end results of this process.

APPENDICES

Appendix 1: Expanded Methods

Age Calibrations, Duration of Global Climate Events, and Lithostratigraphic Correlations

The following details apply to Figures 1, 3, 4, 7, 8, and 9. Chronostratigraphy is correlated to the global $\delta^{13}C_{carb}$ by Ogg et al. (2020, p. 905). Stage boundary absolute ages are from Cohen et al. (2013), with Smithian-Spathian substage boundary age (249.4 Ma) from Widmann et al. (2020). Substages without well-established absolute ages are shown as dashed lines; specifically, the Griesbachian-Dienerian boundary (251.5 Ma) is based on sediment flux rates from Sanson-Barrera (2016, chap. 3), and the Aegean-Bithynian boundary (245.0 Ma) is based on ammonoid biostratigraphic, cyclostratigraphic, and magnetostratigraphic proxies (see Ogg et al., 2020, p. 927). Durations of global warming and cooling event intervals (Figs. 1, 3, 4, 7, 8, and 9) is as follows: end-Permian event (EPE, ~400 k.y.; Fielding et al., 2019), late Smithian thermal maximum (LSTM, ~650 k.y.; Widmann et al., 2020), Smithian-Spathian event (SSE, ~400 k.y.; Widmann et al., 2020), and Early-Middle Triassic event (EMTE, ~500 k.y.; Chen et al., 2020).

The following is a list of sources for Figures 1 and 9 for the localities compared herein: (1) Sydney Basin (Australia), correlations from this study, lithostratigraphy from Smith and Bocking (1993, 1994); (2) Tulong (Tibet) from Schneebeli-Hermann et al. (2012a) and Peng et al. (2019), lithostratigraphy from Brühwiler et al. (2009); (3) Salt-Surghar (Pakistan), correlations from Hermann et al. (2011b) and Schneebeli-Hermann (2020); (4) Greenland (composite of northern and eastern Greenland), correlations from Lindström et al. (2020), lithostratigraphy from Håkansson (1979) and Stemmerik and Håkansson (1989); and (5) Barents Sea (composite of Svalbard and Svalis Dome), correlations from Hochuli and Vigran (2010) and Galfetti et al. (2007b), lithostratigraphy from Nilsson et al. (1996) and Mørk and Elvebakk (1999).

Additional Details for Stable Carbon Isotopes and Total Organic Carbon Analyses

Prior to the analyses, all samples were crushed and ground to a fine powder in an agate mortar and pestle. Material weights of ~0.5 g were then placed in individual 30 ml vials. Hydrochloric acid 2 M (2N) was diluted to 10% then added and mixed with the residues. The vials were oven-dried at 60 °C for 2 h then left overnight to allow all carbonate to be removed as carbon dioxide (CO_2). The acid was then decanted and the sub-samples washed twice using distilled water. After drying again, they were ground once more in situ with a metal spatula.

The technique used for the analyses was Elemental Analyzer Isotope Ratio Mass Spectrometry (EA-IRMS). First, tin capsules containing 1–5 mg of sample or reference material were loaded into an auto-sampler. At Crewe, UK, samples were dropped in a PDZ Europa ANCA-GSL/Geo 20-20 elemental analyzer manufactured by Sercon Ltd. At Storrs, Connecticut, USA, the samples were dropped in a Costech ECS 4010 Elemental Analyzer. Samples were then combusted at 1000 °C in an oxygen-rich environment. The gases produced on combustion were swept in a helium stream over a chromic oxide (Cr_2O_3) combustion catalyst, followed by copper oxide wires to oxidize hydrocarbons, and then through silver wool to remove sulfur and halides. The resultant gases—N_2, NO_x, H_2O, O_2, and CO_2—were swept through a reduction stage of pure copper wires held at 600 °C. This step removes O_2 and converts NO_x species to N_2. A magnesium perchlorate chemical trap removed water, and CO_2 is separated from N_2 by a packed column gas chromatograph held at an isothermal temperature of 100 °C. The resultant CO_2 enters the ion source of the PDZ Europa EA-IRMS where it is ionized and accelerated. Gas species of different mass are separated in a magnetic field, then simultaneously measured using a Faraday cup collector array the isotopomers of CO_2 at mass-to-charge (m/z) ratios of 44, 45, and 46. The analyses proceeded in a batch process, whereby a reference is analyzed followed by

several samples and then another reference. $\delta^{13}C$ values are reported as per mil (‰) relative to the Vienna Peedee Belemnite (VPDB) standard (International Atomic Energy Agency, 1995, p. 157). The reference material for the $\delta^{13}C_{org}$ analysis was IA-R001 (Iso-Analytical working standard wheat flour, $\delta^{13}C_{VPDB} = -26.44‰ \pm 0.14‰$, n = 20), IA-R080 (beet sugar, $\delta^{13}C_{VPDB} = -25.56‰ \pm 0.15‰$, n = 10), and IA-R006 (cane sugar, $\delta^{13}C_{VPDB} = -11.68‰ \pm 0.17‰$, n = 10). IA-R001, IA-R080, and IA-R006 have been calibrated against, and are traceable to, IAEA-CH-6 (International Atomic Energy Agency reference standard sucrose, $\delta^{13}C_{VPDB} = -10.43‰$).

To calculate the TOC values, previously acid-washed sub-samples were weighed at microgram precision before being run through the EA-IRMS process. The total ion beam data was then used to determine the mass of carbon loss following combustion. These are expressed as percentages (%) of the total dried sediment mass. For valid $\delta^{13}C$ isotopic values, TOC values needed to be above the detection limit of 0.01%. The reference material for the TOC analysis was IA-R001 (standard wheat flour, TOC = 40.43% ± 1.35%, n = 20). The analytical precision for the geochemical measurements and statistical analyses are calculated to two standard deviations (2σ, i.e., within a 95% confidence level).

Processing Details for Palynological Samples

Sub-samples were first ground and powdered with an agate mortar and pestle, followed by overnight digestion of carbonate minerals in 10% hydrochloric acid in vials. The acid was then decanted. The sub-samples were washed with distilled water, allowed to settle, and finally decanted; this rinsing process was repeated three times to remove any remaining calcium that can precipitate by the addition of hydrofluoric acid. Hydrofluoric acid (70%) was added to the sub-samples to remove silicates, which were then agitated for 4 h until acid digestion was completed.

The digested sub-samples were then poured into 50 ml polypropylene test tubes and centrifuged for five minutes at 2000 rpm. The hydrofluoric acid was then decanted while avoiding loss of any of the solute. Distilled water was added followed by vortexing, then centrifuging for two minutes and finally decanting; this dilution process was repeated four times. Approximately 25 ml of zinc bromide ($ZnBr_2$) was then added to the sub-sample residues and vortexed. The tubes were then placed in an ultrasonic bath for ~10 s. Residues were set aside for settling for 10 min, before centrifuging for 15 min at 2000 rpm to enable better separation. The floating solute was then poured into 50 ml test tubes, washed, and centrifuged for two minutes at 2000 rpm, repeating this step three times. The residue was then transferred to a 20 ml glass tube. It is from these pre-oxidized residues that the kerogen slides were made.

At this point, a portion of the residue was collected to determine the amount of oxidation required with Schulze's solution (Schulze, 1855). The solution used was composed by 30 g of potassium chlorate ($KClO_3$), 300 ml of H_2O, and 600 ml of 70% nitric acid (NHO_3). These portions were fully submerged in Schultze's solution, vortexed, and placed in a hot water bath at 50 °C. For our samples, 2 min proved to be sufficient to remove most extraneous organic matter. The oxidized sub-samples were then given 10% solution of ammonium hydroxide (NH_4OH) and placed in the hot water bath for two minutes, followed by centrifuging and washing three times. The residue was then examined to determine if the desired level of oxidation was achieved. The prepared sub-samples were then thoroughly washed and water-sieved with a 10 μm nylon mesh. The oxidized-sieved residues were collected in glass tubes.

Several drops of each residue were pipetted onto glass coverslips, mixed with one drop of polyvinyl alcohol embedding medium (which also acts as a dispersant; Riding, 2021, p. 49–50)

with a glass-stirring rod, and allowed to dry. Finally, the coverslip was mounted on a glass slide and clear casting resin was added to permanently hold the coverslip in place.

Appendix 2: The Elusive *Alisporites-Falcisporites* Complex

While identifying and counting palynomorphs, we had the issue of distinguishing specimens of *Alisporites* and *Falcisporites*. As these taxa are common elements of the Sydney Basin assemblages in most of the preserved Triassic strata, we felt it critical to clarify what is known as the "*Alisporites-Falcisporites* complex" (sensu Magohe, 2019).

Alisporites and *Falcisporites* are essentially non-taeniate, haploxylonoid bisaccate pollen grains, each with a distal colpus (see nomenclatural explanation in Punt et al., 2007). When Balme (1970, p. 387–389) defined *Falcisporites stabilis*, he contrasted it to *Alisporites australis*, noting that *A. australis* had a longitudinally elongated corpus, while the corpus of *F. stabilis* is circular-to-transversally elongated. However, he acknowledged that distinguishing between the two species in a random assemblage is challenging unless a sufficiently large number (i.e., 200) of specimens are measured for their corpus length and breath. According to de Jersey and Raine (1990, p. 46), *Falcisporites* is distinct from *Alisporites* by having a thicker cappa on the proximal side of the corpus, by virtue of an expansion of structured exoexine that runs transversely across the cappa. The problem, however, is that palynomorphs in Bunnerong-1 and Eveleigh-1 are often not preserved well enough to see this distinctive marker. Thus, this created a bias whereby *Falcisporites* specimens were instead counted as *Alisporites*. For this reason, we conflate these taxa herein and prefer the broader diagnosis of *Alisporites*, but recognize that they are not synonymous (Jansonius, 1971; Foster, 1979).

ACKNOWLEDGMENTS

We acknowledge the Cammeraygal and Gadigal peoples of the Eora Nation, the traditional owners and custodians of the land from which the collected samples originate. We thank Dominica Byun, Kyle Hughes, and Jodie Rutledge from the Geological Survey of New South Wales for their assistance with core sampling and imaging, and Holly-Anne Turner, Valentina Rossi, Aaron Quigley and Maria McNamara for assistance with sample collection and logistics. We thank Stephen McLoughlin for supporting sample processing costs (Swedish Research Council grant 2022-03920), Russ Harms for processing samples for plant microfossils, Steven Brookes for processing samples for stable carbon, and Daniel Mantle for discussions about Australian biostratigraphy and biozone index taxa. We are grateful to Troy Rasbury and Daniel Peppe for editing the manuscript and Robert A. Gastaldo and one anonymous reviewer for their constructive reviews which greatly improved the manuscript. This research was funded by Research Ireland Centre for Applied Geosciences (grants 13/RC/2092_P2 and 17/RC-PhD/3481) and Research Ireland (grant 22/FFP-P/11448) awarded to C. Mays, the Paleontological Society's Elvira and Bob Gastaldo Deciphering Earth History Award in Applied Paleobotany awarded to M. Amores, and the U.S. National Science Foundation awarded to C. Fielding and T. Frank (grant EAR-1636625).

FIGURES

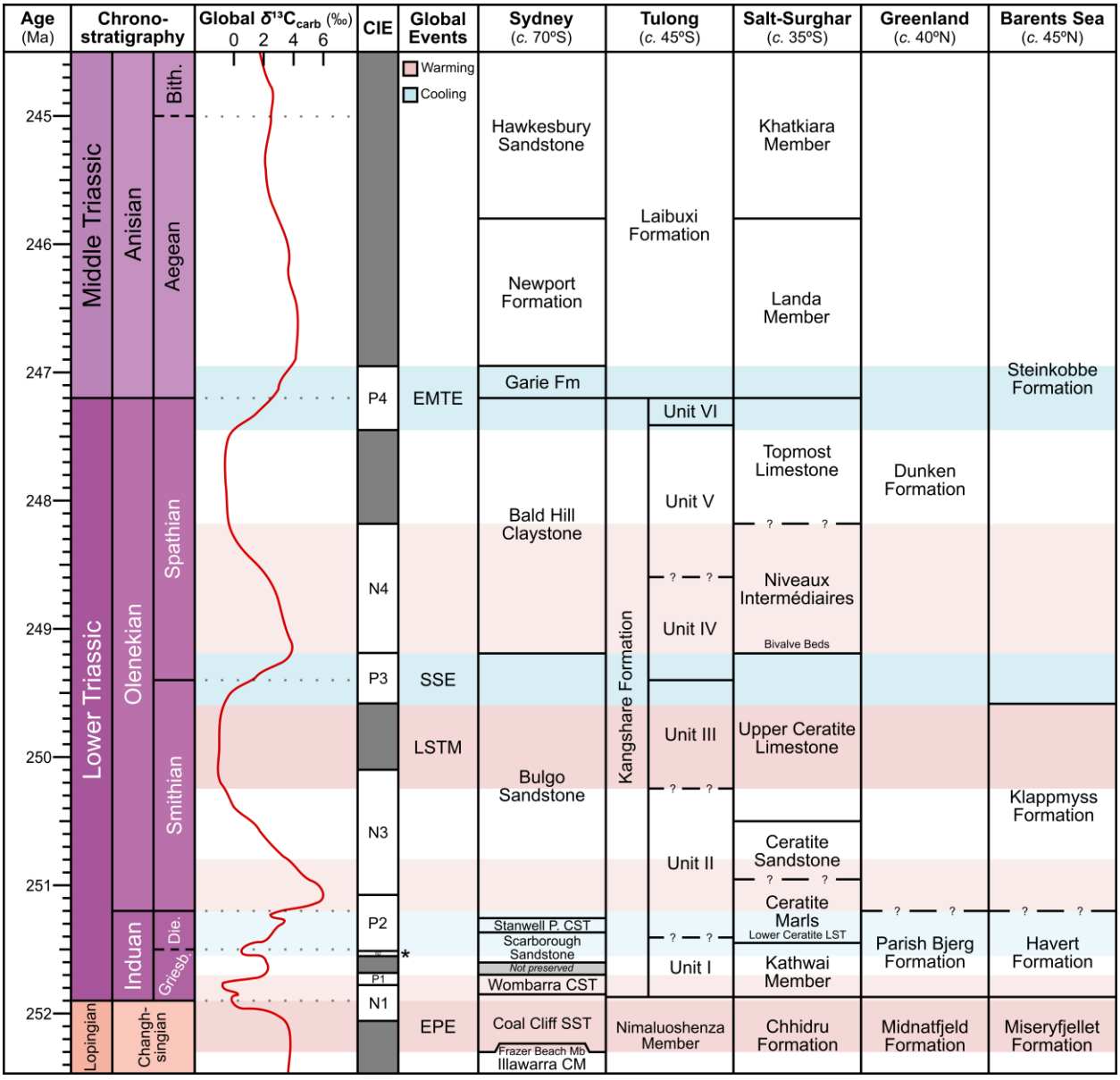

Figure 1. Chronostratigraphic and lithostratigraphic comparisons between localities with high-resolution microfloral and $\delta^{13}C$ data. The primary carbon isotope excursions (CIEs) provided time anchors, with mean depositional rates of intervening strata assumed to be constant. Nomenclature for the Early Triassic positive (P) and negative (N) carbon isotope excursions follow Song et al. (2013). Asterisk (*) below P2 corresponds to N2. Global warming and cooling events from Sun et al. (2012). Compared localities: 1—Sydney Basin (Australia); 2—Tulong

(Tibet); 3—Salt-Surghar (Pakistan); 4—Greenland (composite of northern and eastern Greenland); 5—Barents Sea (composite of Spitsbergen and Svalis Dome). Dashed lines with question marks (?) denote boundaries where chronostratigraphic constrains are insufficient for precise age determination. Sources used for age calibration, duration of global climate events, and lithostratigraphic correlations can be found in Appendix 1. Bith.—Bithynian; CM—Coal Measures; CST—Claystone; Die.—Dienerian; EMTE—Early-Middle Triassic event; EPE—end-Permian event; Fm—Formation; Griesb.—Griesbachian; LSTM—late Smithian thermal maximum; LST—Limestone; Mb—Member; P.—Park; SSE—Smithian-Spathian event; SST—Sandstone.

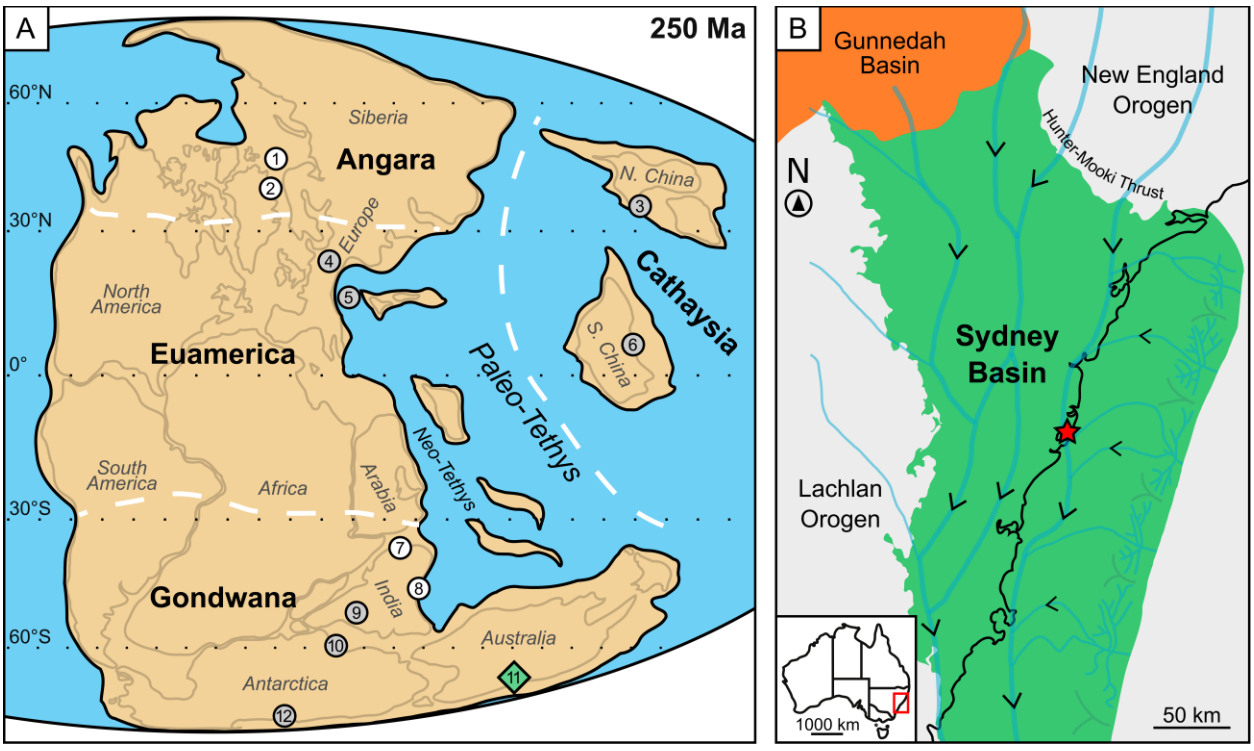

Figure 2. (A) Paleogeographic map of Earth during the Early Triassic (Olenekian, ca. 250 Ma). Paleocoastlines (black lines) modified from Kocsis and Scotese (2021), tectonic reconstructions adapted from Merdith et al. (2021), and rendered in GPlates (Müller et al., 2018) in Mollweide

projection. Extent of the Angara, Euamerica, Cathaysia, and Gondwana floral provinces (white dashes) are based on their Permian paleobiographic ranges, modified from Utting and Piasecki (1995) and McLoughlin (2011). The green diamond (◊) represents the study region, and cited localities as numbered circles: 1—Barents Sea (~45°N); 2—Greenland (~40°N); 3—North China (~35°N); 4—Germany (~25°N); 5—Hungary (~15°N); 6—South China (~5°N); 7—Salt-Surghar Ranges (~35°S); 8—Tulong (~45°S); 9—Godavari Graben (~50°S); 10—Lambert Graben (~60°S); 11—Sydney (~70°S); 12—Allan Hills (~80°S). White circles correspond to localities with high-resolution floristic information that can be temporally correlated with chemostratigraphy (see Fig. 1). (B) Composite geological map of present-day Sydney Basin, Australia, with Early Triassic drainage directions. Geographic position shown as a red rectangle in the small inset map of modern Australia. Modern coastline, areas of Sydney and Gunnedah basins, and bordering orogens are modified from Colquhoun et al. (2024). Additional geological context from features 250 Ma, such as the present extent of the New England Orogen, alluvial fan deposits (green lines), and paleocurrent directions (blue lines with black arrow heads), are modified from Fielding et al. (2021). The red star (⋆) corresponds to the target locality (detailed in Fig. S1; see text footnote 1).

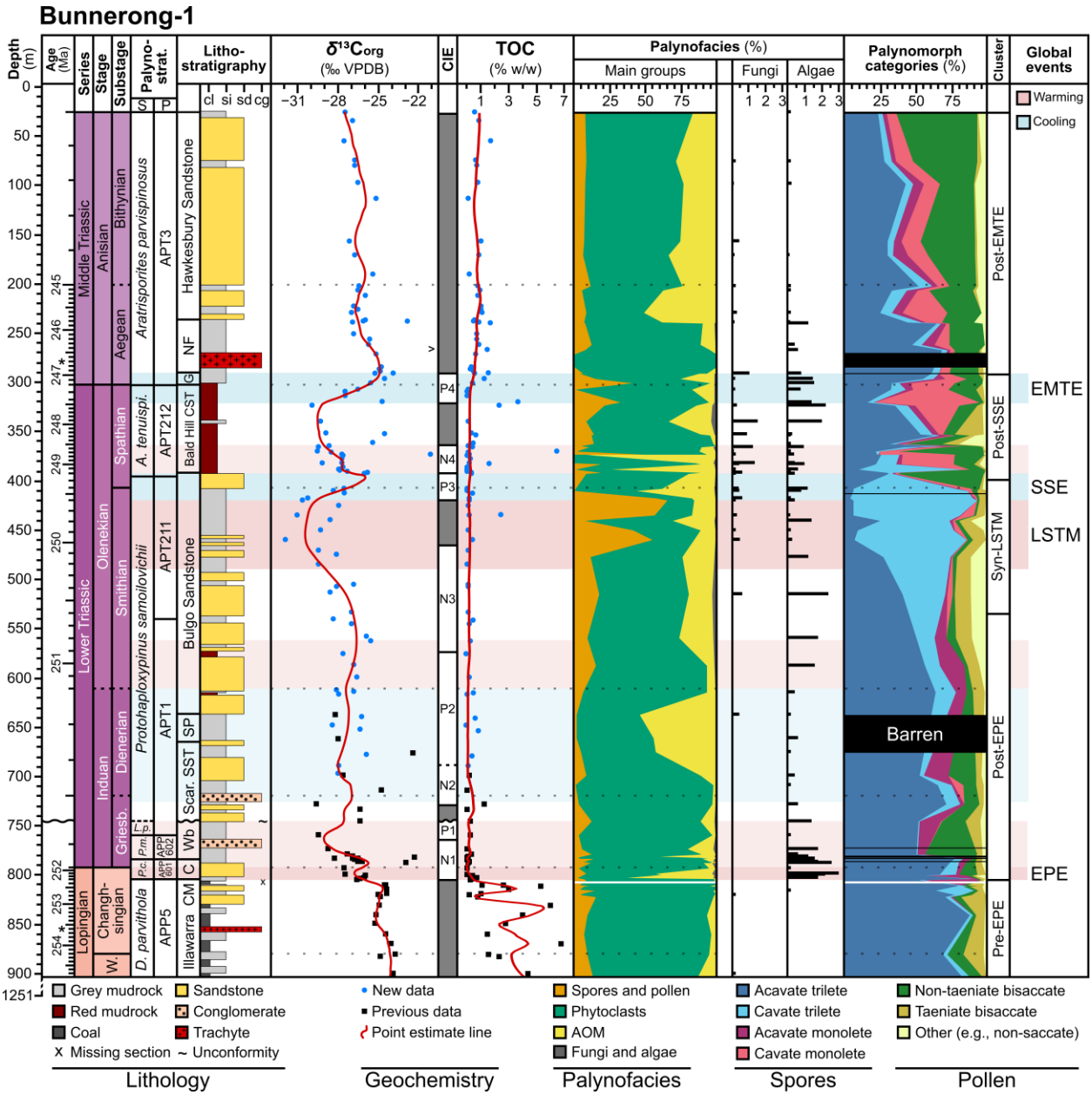

Figure 3. Synthesis of palynological and organic geochemical data for Bunnerong-1, Sydney Basin, Australia. Dashed lines in chronostratigraphy signify tentative boundary positions. Asterisks (*) in age column show sections containing trachytes from Jurassic diatremes. Sources used for age calibration can be found in Appendix 1. Values of $\delta^{13}C_{org}$ and total organic carbon (TOC) are plotted alongside a red three-point estimate line. Arrow to the right of the $\delta^{13}C_{org}$ column represents a sample (267.55 m), whose value goes higher than the cut-off point of

–21.5‰ (see Table S1; see text footnote 1). Nomenclature for the Early Triassic positive (P) and negative (N) carbon isotope excursions follow Song et al. (2013). Global warming and cooling events from Sun et al. (2012). Cluster column refers to the results of the CONISS analysis (see Fig. S2). Additional lithological data from Fielding et al. (2019), and previously published organic geochemical and palynological data from Fielding et al. (2019) and Mays et al. (2020). For specific data values, see Table S1. *A. tenuispi.—Aratrisporites tenuispinosus*; AOM—amorphous organic matter; Bald Hill CST—Bald Hill Claystone; C—Coal Cliff Sandstone; cg—conglomerate; cl—claystone; CIE—carbon isotope excursion; CM—Coal Measures; *D. parvithola—Dulhuntyispora parvithola*; EMTE—Early-Middle Triassic event; EPE—end-Permian event; G—Garie Formation; Griesb.—Griesbachian; LSTM—late Smithian thermal maximum; *L.p.—Lunatisporites pellucidus*; NF—Newport Formation; Palynostrat.—palynostratigraphy; P—informal palynozones by Price (1997); *P.c.—Playfordiaspora crenulata; P.m.—Protohaploxypinus microcorpus*; sd—sandstone; S—standardized eastern Australia palynozones (Foster, 1982; Helby et al., 1987; Mays et al., 2020); Scar. SST—Scarborough Sandstone; si—siltstone; SSE—Smithian-Spathian event; SP—Stanwell Park Claystone; VPDB—Vienna Peedee Belemnite; W.—Wuchiapingian; Wb—Wombarra Claystone.

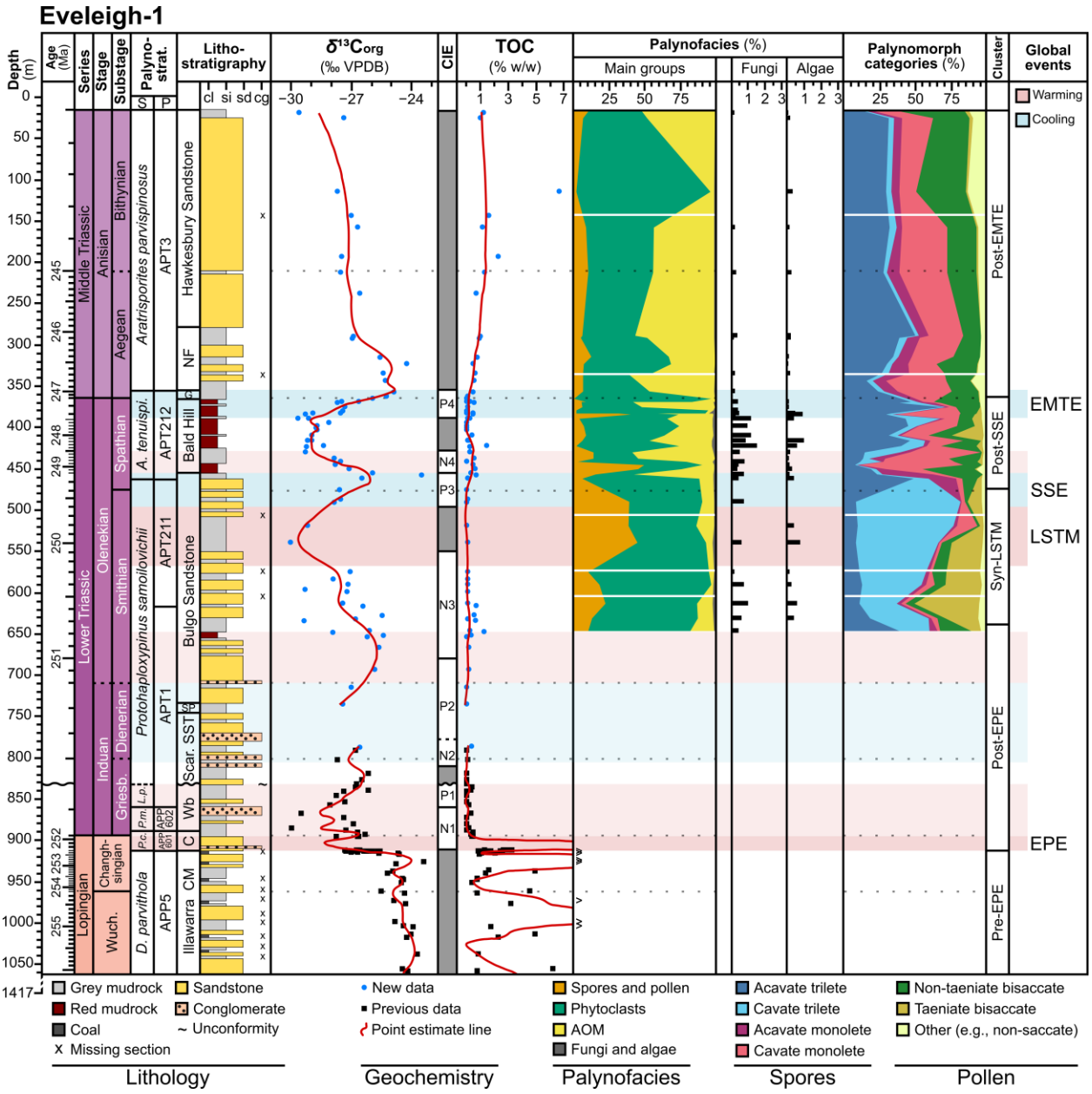

1339

1340 Figure 4. Synthesis of palynological and organic geochemical data for Eveleigh-1, Sydney Basin,

1341 Australia. Dashed lines in chronostratigraphy signify tentative boundary positions. Sources used

1342 for age calibration can be found in Appendix 1. Values of $\delta^{13}C_{org}$ and total organic carbon (TOC)

1343 are plotted alongside a red three-point estimate line. Arrows to the right of the TOC column

1344 represent samples whose values go higher than the cut-off point of 7% (see Table S1; see text

1345 footnote 1). Nomenclature for the Early Triassic positive (P) and negative (N) carbon isotope

excursions follow Song et al. (2013). Cluster column refers to the results of the CONISS analysis (see Fig. S2). Global warming and cooling events from Sun et al. (2012). Previously published organic geochemical data from Shen et al. (2023). For specific data values, see Table S1. *A. tenuispi.*—*Aratrisporites tenuispinosus*; AOM—amorphous organic matter; C—Coal Cliff Sandstone; cg—conglomerate; cl—claystone; CIE—carbon isotope excursion; CM—Coal Measures; *D. parvithola*—*Dulhuntyispora parvithola*; EMTE—Early-Middle Triassic event; EPE—end-Permian event; G—Garie Formation; Griesb.—Griesbachian; LSTM—late Smithian thermal maximum; *L.p.*—*Lunatisporites pellucidus*; NF—Newport Formation; Palynostrat.—Palynostratigraphy; *P.c.*—*Playfordiaspora crenulata*; P—informal palynozones by Price (1997); *P.m.*—*Protohaploxypinus microcorpus*; S—standardized palynozones for eastern Australia (Foster, 1982; Helby et al., 1987; Mays et al., 2020); sd—sandstone; Scar. SST—Scarborough Sandstone; si—siltstone; SSE—Smithian-Spathian event; SP—Stanwell Park Claystone; VPDB—Vienna Peedee Belemnite; Wuch.—Wuchiapingian; Wb—Wombarra Claystone.

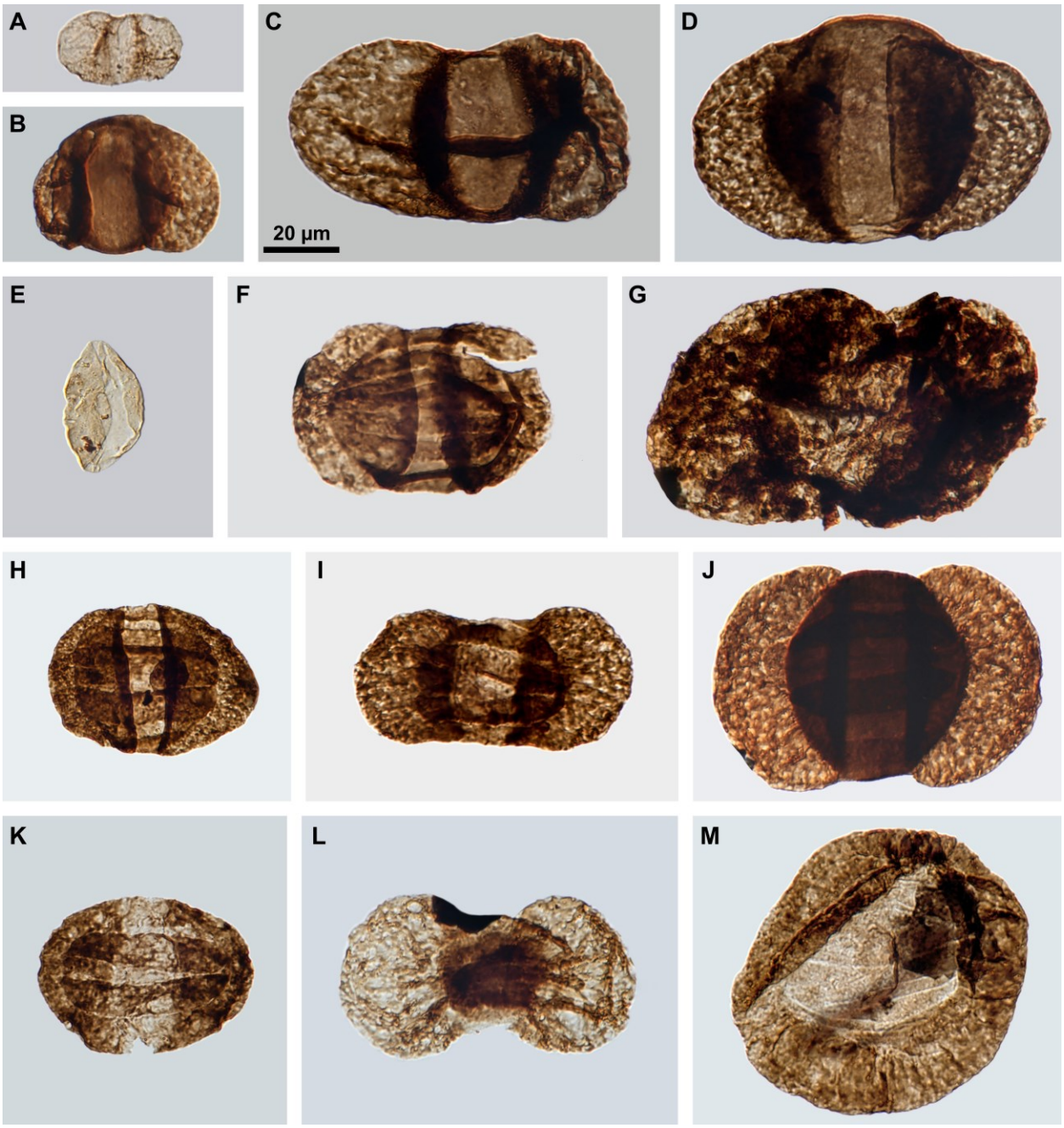

Figure 5. Selected pollen of the Induan, Olenekian, and Anisian of the Sydney Basin, Australia. All images are composed of focus-stacked photomicrographs taken with differential interference contrast; scale bar applies to all figures. England Finder coordinates and sample numbers are supplied in Table S2 (see text footnote 1), with taxon authorities in Table S3.1. (A) *Vitreisporites pallidus*; (B) *Pteruchipollenites indarraensis*; (C) *Chordasporites australiensis*; (D) *Alisporites*

australis; (E) *Cycadopites follicularis*; (F) *Protohaploxypinus samoilovichii*; (G) *Protohaploxypinus microcorpus*; (H) *Lunatisporites* sp. cf. *L. pellucidus*; (I) *Lunatisporites noviaulensis*; (J) *Protohaploxypinus* sp. cf. *P. samoilovichii*; (K) *Lunatisporites pellucidus*; (L) *Striatopodocarpites cancellatus*; (M) *Striomonosaccites morondavensis*.

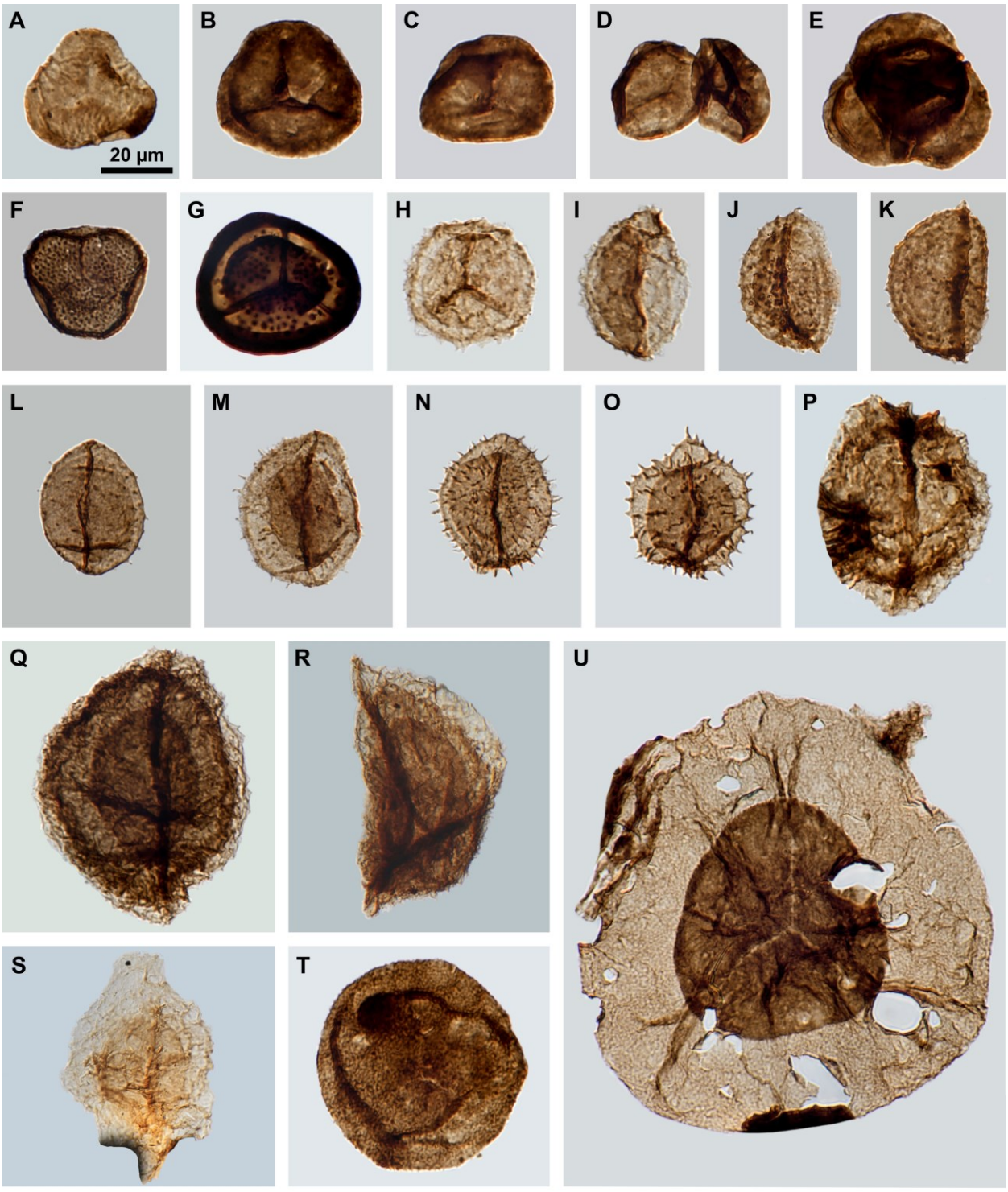

1371

1372 Figure 6. Selected spores of the Induan, Olenekian, and Anisian of the Sydney Basin, Australia.

1373 All images are composed of focus-stacked photomicrographs taken with differential interference

contrast; scale bar applies to all figures. England Finder coordinates and sample numbers are supplied in Table S2, with taxon authorities in Table S3.2. (A) *Triplexisporites playfordii*; (B) *Densoisporites nejburgii* (proximal view); (C) *Densoisporites nejburgii* (oblique view); (D) *Densoisporites nejburgii* (potentially adhering); (E) *Densoisporites nejburgii* (tetrad); (F) *Limatulasporites* species (sp.) cf. *L. fossulatus*; (G) *Limatulasporites limatulus*; (H) *Lundbladispora springsurensis*; (I–K) *Aratrisporites wollariensis*; (L) *Aratrisporites strigosus*; (M–O) *Aratrisporites tenuispinosus*; (P) *Aratrisporites plicatus*; (Q) *Aratrisporites coryliseminis* (proximal view); (R) *Aratrisporites coryliseminis* (lateral view); (S) *Aratrisporites* sp. cf. *A. parvispinosus*; (T) *Osmundacidites wellmanii*; (U) *Playfordiaspora crenulata*.

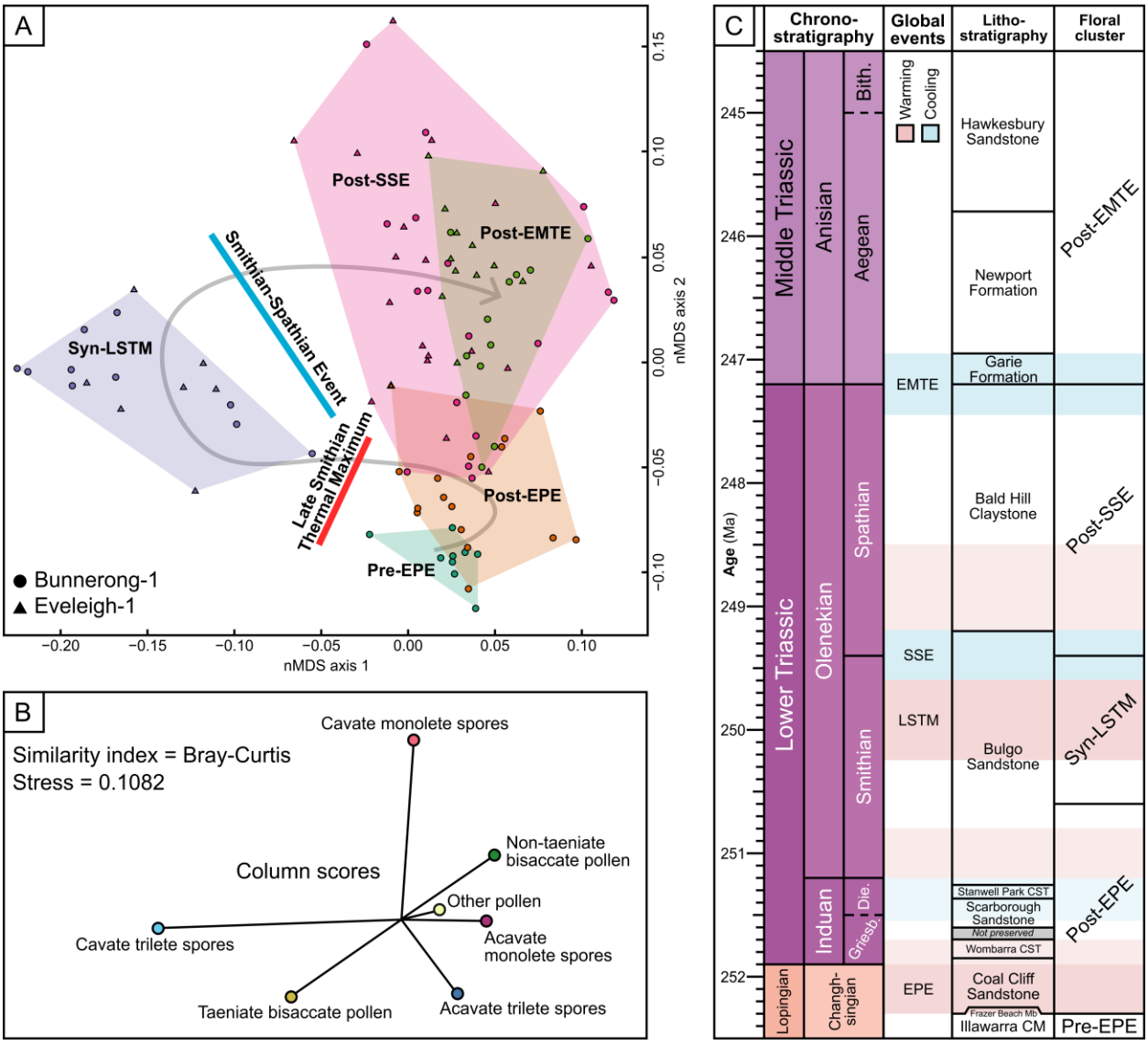

Figure 7. (A) Ordination data analysis of broad spores and pollen morphological groupings in Bunnerong-1 and Eveleigh-1 by non-metric multidimensional scaling (nMDS). The two climatic events responsible for the most significant changes in microfloral associations are the late Smithian thermal maximum and the Smithian-Spathian event. Generalized progression through time represented by a light gray arrow. (B) Column scores show the relative influences of each group on the resulting two-dimensional plot. (C) Chronostratigraphic chart with the five microfloral associations specified by cluster analysis with CONISS (see Fig. S2; see text footnote 1): 1—pre-EPE; 2—post-EPE; 3—syn-LSTM; 4—post-SSE; and 5—post-EMTE.

Global warming and cooling events from Sun et al. (2012). Substages without well-established absolute ages shown as dashed lines. Sources used for age calibration can be found in Appendix 1. Bith—Bithynian; CM—Coal Measures; CST—Claystone; Die.—Dienerian; EPE—end-Permian event; EMTE—Early-Middle Triassic event; Griesb.—Griesbachian; LSTM—late Smithian thermal maximum; Mb—Member; SSE—Smithian-Spathian event.

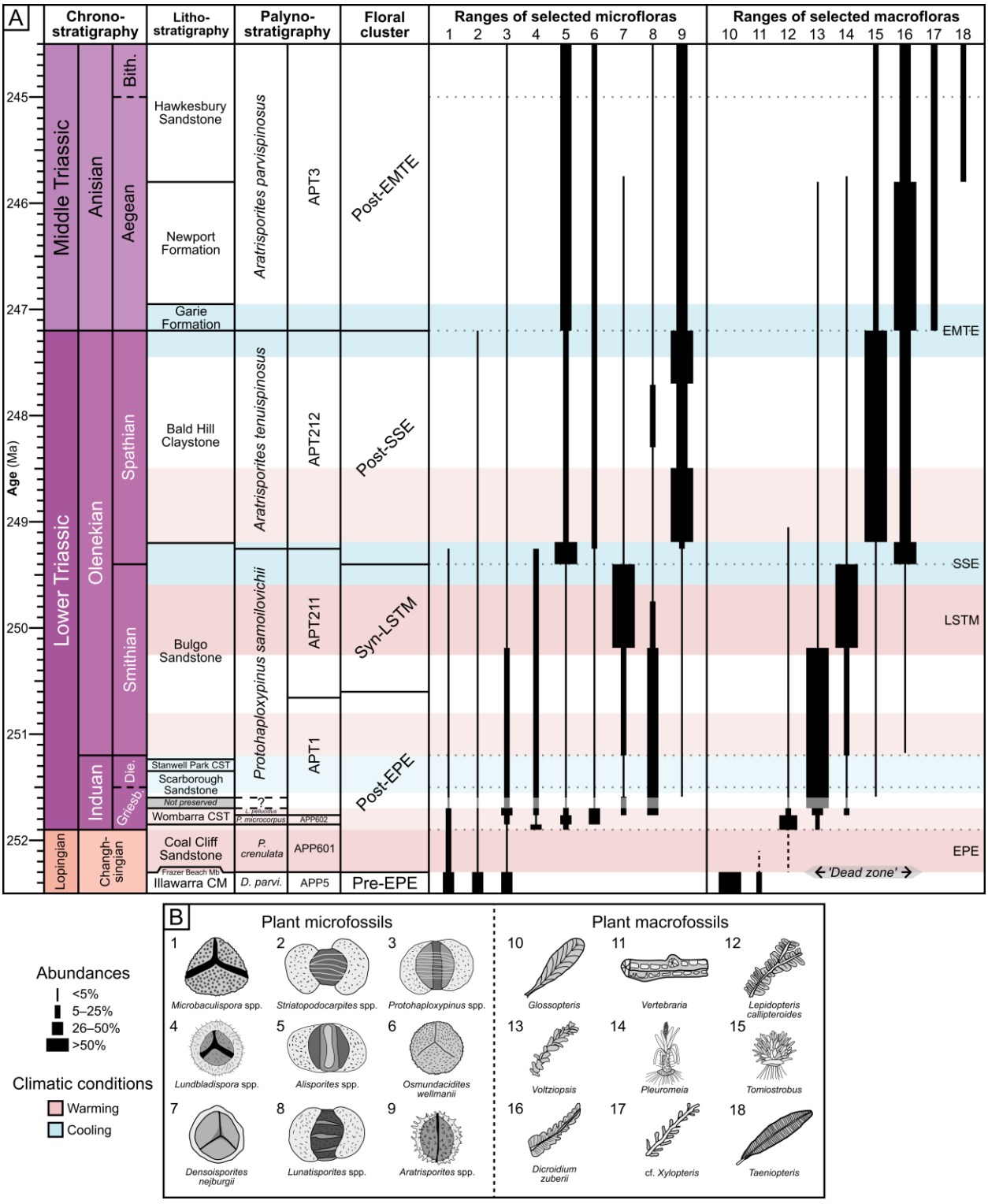

Figure 8. (A) Range chart of selected micro- and macrofloras that summarize the major floral communities present in the Sydney Basin, Australia, from the uppermost Permian

(Changhsingian) to the lower Middle Triassic (Anisian). Global warming and cooling events from Sun et al. (2012). Microfloral information derived from Helby (1970), Helby et al. (1987), Mays et al. (2020), and this study. Palynostratigraphy from the standardized palynozones for eastern Australia (Foster, 1982; Helby et al., 1987; Mays et al., 2020) on the left, and informal palynozones from Price (1997) on the right. Macrofloral information adapted from Retallack (1975, 1977, 1980, 1997, 1999), Fielding et al. (2019), and Mays et al. (2020). Fossil stratigraphic ranges with dashed lines require further verification. Substages without well-established absolute ages shown as dashed lines. Sources used for age calibration can be found in Appendix 1. (B) Illustrations of selected micro- and macrofloras. Likely affinities are provided in Table 2. Bith—Bithynian; CM—Coal Measures; CST—Claystone; *D. parvi*.—*Dulhuntyispora parvithola*; Die.—Dienerian; EMTE—Early-Middle Triassic event; EPE—end-Permian event; Griesb.—Griesbachian; *L. pellucidus*—*Lunatisporites pellucidus*; LSTM—late Smithian thermal maximum; Mb—Member; *P. microcorpus*—*Protohaploxypinus microcorpus*; *P. crenulata*—*Playfordiaspora crenulata*; SSE—Smithian-Spathian event.

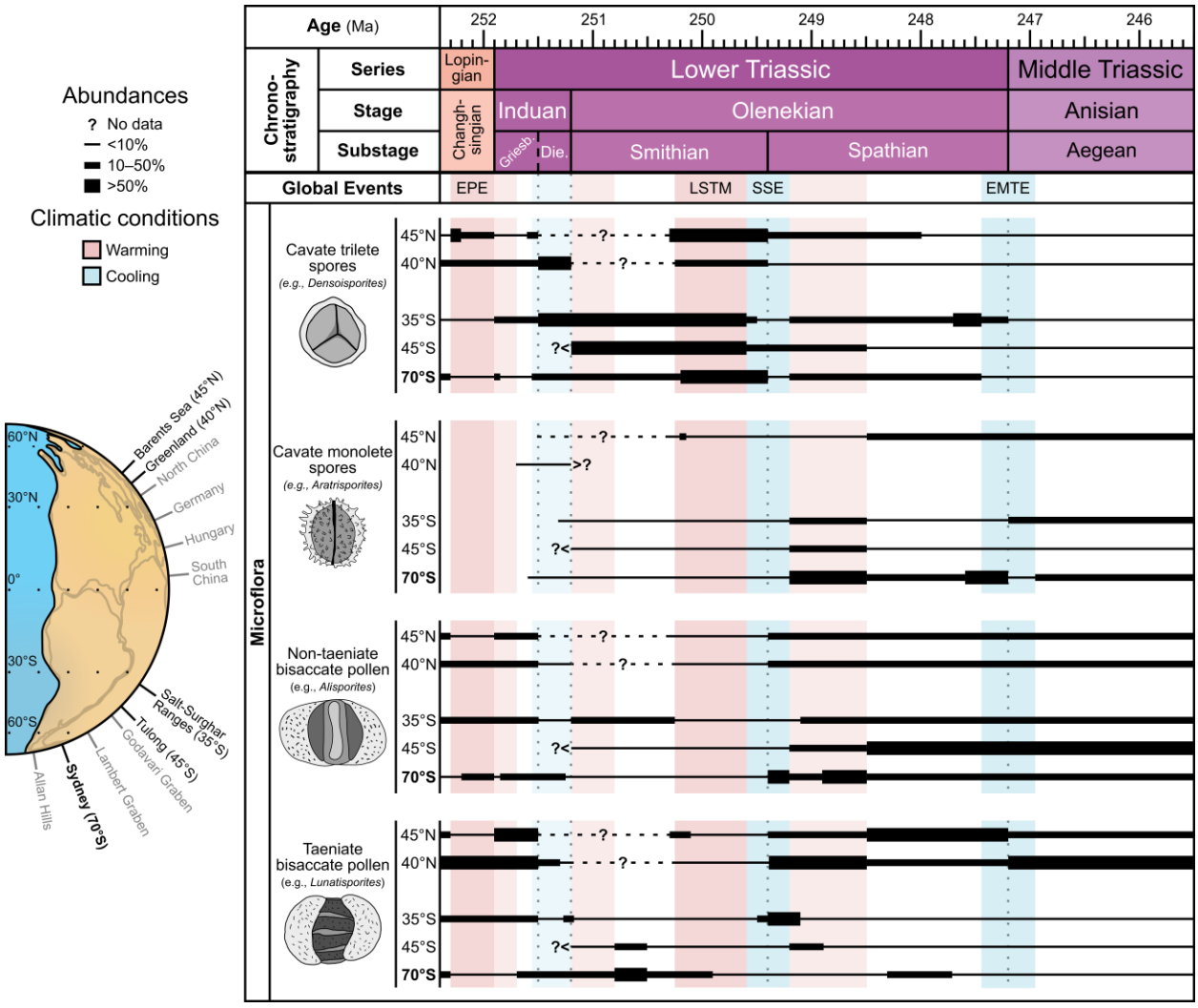

Figure 9. Global floristic comparisons with selected localities. Localities that have sufficient quantitative palynofloral data and $\delta^{13}C$ sampling density are plotted, others are in gray on the orthographic, paleogeographic map of Earth (ca. 250 Ma; Kocsis and Scotese, 2021; Merdith et al., 2021). Abundances constrained to the global chronostratigraphy by chemostratigraphic correlations are outlined in Figure 1. Global warming and cooling events from Sun et al. (2012). Substages without well-established absolute ages shown as dashed lines. Sources used for age calibration can be found in Appendix 1. References for chartered localities are: Barents Sea (~45°N) from Mangerud (1994), Vigran et al. (1998), Galfetti et al. (2007b), Hochuli et al. (2010a), and Hochuli and Vigran (2010); Greenland (~40°N) from Hochuli et al. (2010b, 2016)

and Lindström et al. (2020); Salt-Surghar Ranges, Pakistan (~35°S) from Hermann et al. (2011a, 2012), Schneebeli-Hermann et al. (2015), and Schneebeli-Hermann (2020); Tulong, Tibet (~45°S) from Schneebeli-Hermann et al. (2012a), Peng et al. (2019), and Liu et al. (2020); and Sydney, eastern Australia (~70°S) from Fielding et al. (2019), Mays et al. (2020), and this study. Die.—Dienerian; EPE—end-Permian event; EMTE—Early-Middle Triassic event; Griesb.—Griesbachian; LSTM—late Smithian thermal maximum; SSE—Smithian–Spathian event.

TABLES

Table 1. Lithological Descriptions

Name		Description (Geoscience Australia and Australian Stratigraphy Commission, 2024)
Hawkesbury Sandstone		Medium to coarse-grained quartz sandstone with minor shale and laminite lenses; secondary quartz cement.
Narrabeen Group	Newport Formation	Interbedded laminite, shale, quartz to lithic-quartz sandstone; minor red claystone.
	Garie Formation	Clay pellet sandstone, dark lithic fine sandstone, chocolate claystone bands
	Bald Hill Claystone	Dominantly red shale and fine to medium-grained sandstone.
	Bulgo Sandstone	Fine to medium-grained quartz-lithic sandstone with lenticular shale interbeds.
	Stanwell Park Claystone	Red, green, and grey shale and quartz-lithic sandstone.
	Scarborough Sandstone	Quartz-lithic sandstone, pebbly in parts.
	Wombarra Claystone	Grey shale, minor quartz-lithic sandstone.
	Coal Cliff Sandstone	Medium-grained quartz-lithic sandstone with calcareous-cement; contains sideritic oolites.
Illawarra Coal Measures		Shale, quartz-lithic sandstone, conglomerate, chert, sporadically carbonaceous mudstone, coal, and torbanite seams.

Table 2. Botanical Affinities of Mentioned Spore-Pollen Taxa With Sources

Taxon	Affinities and sources*
POLLEN	
└Non-taeniate bisaccate	
└*Alisporites* spp.	Conifer (Voltziales[1,2]); †seed fern (Peltaspermales[3,4], Umkomasiales[5,6])
└*Chordasporites* spp.	Seed fern (§Peltaspermales, §Umkomasiales)
└*Pteruchipollenites* spp.	Seed fern (Umkomasiales[6])
└*Vitreisporites* spp.	Seed fern (?Caytoniales[7], †Peltaspermales[8])
└Taeniate bisaccate	
└*Lunatisporites* spp.	Conifer (Voltziales[2])
└*Protohaploxypinus* spp.	Seed fern (§Glossopteridales[9,10], Peltaspermales[8,11])
└*Striatopodocarpites* spp.	Seed fern (Glossopteridales[9])
└Other	
└Colpate	
└*Cycadopites* spp.	Bennettitales[12], †Cycadales[13,14], Ginkgoales[13,14], Gnetales[15], †seed fern (Peltaspermales[16,17])
└Polyplicate	
└*Praecolpatites* spp.	§Ginkgoales[13], †Gnetales[15]
└Taeniate monosaccate	
└*Striomonosaccites* spp.	Seed fern (Glossopteridales[9])
SPORES	
└Acavate trilete	
└*Brevitriletes* spp.	Fern (Zygopteridales[18])
└*Craterisporites* spp.	§Fern (*incertae sedis*)
└*Horriditriletes* spp.	Fern (Osmundales[19])
└*Leiotriletes* spp.	Fern (Zygopteridales[20], Botryopteridales[21])
└*Microbaculispora* spp.	§Fern (*incertae sedis*)
└*Neoraistrickia* spp.	Fern (Osmundales[22])
└*Osmundacidites* spp.	Fern (Osmundales[23])
└*Raistrickia* spp.	Fern (Zygopteridales[24], Botryopteridales[21])
└*Rewanispora* spp.	§Lycopod (*incertae sedis*)
└*Triplexisporites* spp.	Fern (?Schizaeales[25], ?Polypodiales[25])
└Cavate trilete	
└*Annulispora* spp.	§Bryophyte (*incertae sedis*)
└*Densoisporites* spp.	Lycopod (†Isoëtales[26,27], Selaginellales[28,29])
└*Endosporites* spp.	Lycopod (?Isoëtales[30], ?Lepidodendrales[31])
└*Kraeuselisporites* spp.	§Lycopod (*incertae sedis*)
└*Limatulasporites* spp.	§Bryophyte (*incertae sedis*[32])
└*Lundbladispora* spp.	Lycopod (Isoëtales[33])
└*Playfordiaspora* spp.	§Lycopod (*incertae sedis*)
└*Striatella* spp.	Fern (?Polypodiales[34])
└Cavate monolete	
└*Aratrisporites* spp.	Lycopod (Isoëtales[35,36])

Note: Listed affinities are in respect to macrofloras found in the Sydney Basin between the late Permian and Middle Triassic (e.g., Retallack, 1977). Plant orders known outside this expected temporal range are shown with a question mark (?) before their name. For taxonomic ranks below order, see cited sources herein. Sources: 1, Bomfleur et al. (2013); 2, Nowak et al. (2024); 3, Retallack (2002); 4, Naugolnykh (2013b); 5, Blomenkemper et al. (2020); 6. Osborn and Taylor (1993); 7, van Konijnenburg-van Cittert (1971); 8, Gomankov and Meyen (1986); 9, Lindström

et al. (1997); 10, Gould and Delevoryas, (1977); 11, Zavialova and Karasev, (2015); 12, Pott et al. (2017); 13, Tekleva et al. (2007); 14, Zavialova et al. (2016); 15, Krassilov and Bugdaeva (1988); 16, Vajda et al. (2023b); 17, Vajda et al. (2024); 18, Galtier and Scott (1979); 19, Galtier and Taylor, (1994); 20, Chaphekar and Alvin (1972); 21, Potonié (1962); 22, see discussion by de Jersey and Raine (1990, pp. 30–31) regarding the status of *Neoraistrickia* as a senior synonym of *Horriditriletes*; 23, Litwin (1985); 24, Mickle (1980); 25, tentative, morphology (i.e. striae) of *Anemia* and *Ceratopteris* (Dettmann and Clifford, 1992) show similarities; 26, typically associated with pleuromeians (Pleuromeiaceae), with *D. nejburgii* in particular being found *in situ* in *Pleuromeia sternbergii* (Grauvogel-Stamm and Lugardon, 2004) and *P. rossica* (Lugardon et al., 1999); 27, Retallack (1997) refers to *D. playfordii* being found in *Tomiostrobus polaris*; 28, spores morphologically similar with *D. playfordii* in Lundblad (1948); 29, Zavialova et al. (2010); 30, Pigg and Rothwell (1983) report *Endosporites* spores in Carboniferous-aged *Chaloneria* (Chaloneriaceae); 31, Chaloner (1953); 32, no *in situ* occurrences, but suggested by McLoughlin et al. (1997) to be bryophytic; 33, Wood and Beeston (1979), with Retallack (1997) associating *Lundbladispora* sp. cf. *L. springsurensis* to *Isoetes beestonii* (Isoëtaceae); 34, no *in situ* occurrences, but suggested by Filatoff and Price (1988); 35, Helby and Martin (1965) report *Aratrisporites tenuispinosus* in *Cylostrobus sydneyensis* (Pleuromeiaceae); 36, Ash (1979) found *Aratrisporites* ?*tenuispinosus* in *Skilliostrobus australis* (junior synonym of *Tomiostrobus australis*; Retallack, 1997).

[*] General sources based on the review by Balme (1995).

[†] Proposed principal affinity, considering regional co-eval macrofossils.

[§] No conclusive sources found, considering morphologically analogous taxa.

REFERENCES CITED

Abu Hamad, A., Kerp, H., Vörding, B., and Bandel, K., 2008, A Late Permian flora with Dicroidium from the Dead Sea region, Jordan: Review of Palaeobotany and Palynology, v. 149, p. 85–130, https://doi.org/10.1016/j.revpalbo.2007.10.006.

Abu Hamad, A., Blomenkemper, P., Kerp, H., and Bomfleur, B., 2017, *Dicroidium bandelii* sp. nov. (corystospermalean foliage) from the Permian of Jordan: PalZ,v. 91, p. 641–648, https://doi.org/10.1007/s12542-017-0384-2.

Alvarez, S.A., Gibbs, S.J., Bown, P.R., Kim, H., Sheward, R.M., and Ridgwell, A., 2019, Diversity decoupled from ecosystem function and resilience during mass extinction recovery: Nature, v. 574, p. 242–245, https://doi.org/10.1038/s41586-019-1590-8.

Anderson, J.M., and Anderson, H.M., 1983, Palaeoflora of Southern Africa—Molteno Formation (Triassic)—Part 1. Introduction; Part 2. Dicroidium: Rotterdam, Netherlands, August Aimé Balkema, v. 1, 227 p.

Ash, S.R., 1979, *Skilliostrobus* gen. nov., a new lycopsid cone from the Early Triassic of Australia: Alcheringa, v. 3, p. 73–89, https://doi.org/10.1080/03115517908619087.

Augland, L.E., Ryabov, V.V., Vernikovsky, V.A., Planke, S., Polozov, A.G., Callegaro, S., Jerram, D.A., and Svensen, H.H., 2019, The main pulse of the Siberian Traps expanded in size and composition: Scientific Reports, v. 9, 18723, https://doi.org/10.1038/s41598-019-54023-2.

Awatar, R., Tewari, R., Agnihotri, D., Chatterjee, S., Pillai, S.S.K., and Meena, K.L., 2014, Late Permian and Triassic palynomorphs from the Allan Hills, central Transantarctic Mountains, South Victoria Land, Antarctica: Current Science, v. 106, p. 988–996, https://www.jstor.org/stable/24102383.

Bachan, A., van de Schootbrugge, B., Fiebig, J., McRoberts, C.A., Ciarapica, G., and Payne, J.L., 2012, Carbon cycle dynamics following the end-Triassic mass extinction—Constraints from paired δ^{13}Ccarb and δ^{13}Corg records: Geochemistry, Geophysics, Geosystems, v. 13, https://doi.org/10.1029/2012GC004150.

Balme, B.E., 1970, Palynology of Permian and Triassic strata in the Salt Range and Surghar Range, West Pakistan, *in* Kummel, B., and Teichert, K., eds., Stratigraphic Boundary Problems—Permian and Triassic of West Pakistan: Lawrence, Kansas, USA, University of Kansas Press Special Publication 4, p. 305–453, https://hdl.handle.net/1808/3896.

Balme, B.E., 1995, Fossil in situ spores and pollen grains—an annotated catalogue: Review of Palaeobotany and Palynology, v. 87, p. 81–323, https://doi.org/10.1016/0034-6667(95)93235-X.

Barbolini, N., Bamford, M.K., and Rubidge, B., 2016, Radiometric dating demonstrates that Permian spore-pollen zones of Australia and South Africa are diachronous: Gondwana Research, v. 37, p. 241–251, https://doi.org/10.1016/j.gr.2016.06.006.

Barreda, V.D., Cúneo, N.R., Wilf, P., Currano, E.D., Scasso, R.A., and Brinkhuis, H., 2012, Cretaceous/Paleogene floral turnover in Patagonia—Drop in diversity, low Extinction, and a *Classopollis* spike: PLoS One, v. 7, https://doi.org/10.1371/journal.pone.0052455.

Bercovici, A., Hadley, A., and Villanueva-Amadoz, U., 2009, Improving depth of field resolution for palynological photomicrography: Palaeontologica Electronica, v. 12, no. 2, 12 p., https://palaeo-electronica.org/2009_2/170/.

Blomenkemper, P., Kerp, H., Abu Hamad, A., and Bomfleur, B., 2020, Contributions towards whole-plant reconstructions of *Dicroidium* plants (Umkomasiaceae) from the Permian of Jordan: Review of Palaeobotany and Palynology, v. 278, https://doi.org/10.1016/j.revpalbo.2020.104210.

Bomfleur, B., Taylor, E.L., Taylor, T.N., Serbet, R., Krings, M., and Kerp, H., 2011, Systematics and paleoecology of a new peltaspermalean seed fern from the Triassic polar vegetation of Gondwana: International Journal of Plant Sciences, v. 172, p. 807–835, https://doi.org/10.1086/660188.

Bomfleur, B., Decombeix, A.-L., Escapa, I.H., Schwendemann, A.B., and Axsmith, B., 2013, Whole-plant concept and environment reconstruction of a *Telemachus* conifer (Voltziales) from the Triassic of Antarctica: International Journal of Plant Sciences, v. 174, p. 425–444, https://doi.org/10.1086/668686.

Bomfleur, B., Blomenkemper, P., Kerp, H., and McLoughlin, S., 2018, Polar regions of the Mesozoic–Paleogene greenhouse world as refugia for relict plant groups, *in* Krings, M., Harper, C.J., Cúneo, R.N., and Rothwell, G.W., eds., Transformative Paleobotany—Papers to Commemorate the Life and Legacy of Thomas N. Taylor: Academic Press, p. 593–611, https://doi.org/10.1016/B978-0-12-813012-4.00024-3.

Bond, D.P.G., and Grasby, S.E., 2017, On the causes of mass extinctions: Palaeogeography, Palaeoclimatology, Palaeoecology, v. 478, p. 3–29, https://doi.org/10.1016/j.palaeo.2016.11.005.

Bowman, H.N., 1980, Southern Coalfield, upper Shoalhaven Group and Illawarra Coal Measures, *in* Herbert, C., and Helby, C., eds., A Guide to the Sydney Basin: Australia, Don West, Government Printer, Geological Survey of New South Wales, Department of Mineral Resources Bulletin, v. 26, p. 117–132, https://nswdpe.intersearch.com.au/nswdpejspui/handle/1/2237.

Boyce, C.K., and Lee, J.-E., 2017, Plant evolution and climate over geological timescales: Annual Review of Earth and Planetary Sciences, v. 45, p. 61–87, https://doi.org/10.1146/annurev-earth-063016-015629.

Broothaerts, N., Robles-López, S., Abel-Schaad, D., Pérez-Díaz, S., Alba-Sánchez, F., Luelmo-Lautenschlaeger, R., Glais, A., and López-Sáez, J.A., 2018, Reconstructing past arboreal cover based on modern and fossil pollen data—A statistical approach for the Gredos Range (central Spain): Review of Palaeobotany and Palynology, v. 255, p. 1–13, https://doi.org/10.1016/j.revpalbo.2018.04.007.

Brühwiler, T., Goudemand, N., Galfetti, T., Bucher, H., Baud, A., Ware, D., Hermann, E., Hochuli, P.A., and Martini, R., 2009, The Lower Triassic sedimentary and carbon isotope records from Tulong (south Tibet) and their significance for Tethyan palaeoceanography: Sedimentary Geology, v. 222, p. 314–332, https://doi.org/10.1016/j.sedgeo.2009.10.003.

Burgess, S.D., and Bowring, S.A., 2015, High-precision geochronology confirms voluminous magmatism before, during, and after Earth's most severe extinction: Science Advances, v. 1, https://doi.org/10.1126/sciadv.1500470.

Burgess, S.D., Bowring, S., and Shen, S., 2014, High-precision timeline for Earth's most severe extinction: Proceedings of the National Academy of Sciences of the United States of America, v. 111, p. 3316–3321, https://doi.org/10.1073/pnas.1317692111.

Cao, C., Wang, W., and Jin, Y., 2002, Carbon isotope excursions across the Permian–Triassic boundary in the Meishan section, Zhejiang Province, China: Chinese Science Bulletin, v. 47, p. 1125–1129, https://doi.org/10.1360/02tb9252.

Carvalho, M.R., et al., 2021, Extinction at the end-Cretaceous and the origin of modern Neotropical rainforests: Science, v. 372, p. 63–68, https://doi.org/10.1126/science.abf1969.

Cascales-Miñana, B., and Cleal, C.J., 2014, The plant fossil record reflects just two great extinction events: Terra Nova, v. 26, p. 195–200, https://doi.org/10.1111/ter.12086.

Cascales-Miñana, B., Diez, J.B., Gerrienne, P., and Cleal, C.J., 2016, A palaeobotanical perspective on the great end-Permian biotic crisis: Historical Biology, v. 28, p. 1066–1074, https://doi.org/10.1080/08912963.2015.1103237.

Chaloner, W.G., 1953, A new species of *Lepidostrobus* containing unusual spores: Geological Magazine, v. 90, p. 97–110, https://doi.org/10.1017/S0016756800063998.

Chaphekar, M., and Alvin, K.L., 1972, On the fertile parts of the coenopterid fern *Metaclepsydropsis duplex* (Williamson): Review of Palaeobotany and Palynology, v. 14, p. 63–76, https://doi.org/10.1016/0034-6667(72)90008-5.

Chen, Y., Jiang, H., Ogg, J.G., Zhang, Y., Gong, Y., and Yan, C., 2020, Early–Middle Triassic boundary interval—Integrated chemo-bio-magneto-stratigraphy of potential GSSPs for the base of the Anisian Stage in south China: Earth and Planetary Science Letters, v. 530, https://doi.org/10.1016/j.epsl.2019.115863.

Chen, Z.-Q., and Benton, M.J., 2012, The timing and pattern of biotic recovery following the end-Permian mass extinction: Nature Geoscience, v. 5, p. 375–383, https://doi.org/10.1038/ngeo1475.

Clarke, K.R., 1993, Non-parametric multivariate analyses of changes in community structure: Australian Journal of Ecology, v. 18, p. 117–143, https://doi.org/10.1111/j.1442-9993.1993.tb00438.x.

Clarke, K.R., Somerfield, P.J., and Chapman, M.G., 2006, On resemblance measures for ecological studies, including taxonomic dissimilarities and a zero-adjusted Bray-Curtis coefficient for denuded assemblages: Journal of Experimental Marine Biology and Ecology, v. 330, p. 55–80, https://doi.org/10.1016/j.jembe.2005.12.017.

Clarke, W.B., 1878, Remarks on the Sedimentary Formations of New South Wales—Illustrated by References to Other Provinces of Australasia: Sydney, Australia, Thomas Richards, Government Printer, 165 p., https://doi.org/10.5962/bhl.title.167745.

Cohen, K.M., Finney, S.C., Gibbard, P.L., and Fan, J.-X., 2013, The ICS International Chronostratigraphic Chart: Episodes, v. 36, p. 199–204, https://doi.org/10.18814/epiiugs/2013/v36i3/002.

Colquhoun, G.P., Hughes, K.S., Deyssing, L., Ballard, J.C., Folkes, C.B., Phillips, G., Troedson, A.L., and Fitzherbert, J.A., 2024, New South Wales Seamless Geology Data package, version 2.4 [digital dataset]: Geological Survey of New South Wales Geological Map, https://search.geoscience.nsw.gov.au/product/9232/8454175.

Condon, D.J., McLean, N., Noble, S.R., and Bowring, S.A., 2010, Isotopic composition ($^{238}U/^{235}U$) of some commonly used uranium reference materials: Geochimica et Cosmochimica Acta, v. 74, p. 7127–7143, https://doi.org/10.1016/j.gca.2010.09.019.

Condon, D.J., Schoene, B., McLean, N.M., Bowring, S.A., and Parrish, R.R., 2015, Metrology and traceability of U–Pb isotope dilution geochronology (EARTHTIME Tracer Calibration Part I): Geochimica et Cosmochimica Acta, v. 164, p. 464–480, https://doi.org/10.1016/j.gca.2015.05.026.

Cowan, E.J., 1993, Longitudinal fluvial drainage patterns within a foreland basin-fill—Permo-Triassic Sydney Basin, Australia: Sedimentary Geology, v. 85, p. 557–577, https://doi.org/10.1016/0037-0738(93)90102-B.

Cramer, B.D., and Jarvis, I., 2020, Carbon isotope stratigraphy, in Gradstein, F.M., Ogg, J.G., Schmitz, M.D., and Ogg, G.M., eds., Geologic Time Scale 2020: Elsevier, p. 309–343, https://doi.org/10.1016/B978-0-12-824360-2.00011-5.

Dettmann, M.E., and Clifford, H.T., 1992, Phylogeny and biogeography of *Ruffordia*, *Mohria* and *Anemia* (Schizaeaceae) and *Ceratopteris* (Pteridaceae): Evidence from *in situ* and dispersed spores: Alcheringa, v. 16, p. 269–314, https://doi.org/10.1080/03115519208619111.

de Jersey, N.J., and Raine, J.I., 1990, Triassic and earliest Jurassic miospores from the Murihiku Supergroup, New Zealand: New Zealand Geological Survey Paleontological Bulletin, v. 62, p. 1–164.

DiMichele, W.A., Behrensmeyer, A.K., Olszewski, T.D., Labandeira, C.C., Pandolfi, J.M., Wing, S.L., and Bobe, R., 2004, Long-term stasis in ecological assemblages—Evidence from the fossil record: Annual Review of Ecology, Evolution, and Systematics, v. 35, p. 285–322, https://doi.org/10.1146/annurev.ecolsys.35.120202.110110.

Du, Y., Song, H., Algeo, T.J., Song, H., Tian, L., Chu, D., Shi, W., Li, C., and Tong, J., 2022, A massive magmatic degassing event drove the late Smithian thermal maximum and

Smithian-Spathian boundary mass extinction: Global and Planetary Change, v. 215, https://doi.org/10.1016/j.gloplacha.2022.103878.

Elgorriaga, A., Escapa, I.H., and Cúneo, N.R., 2019, Relictual *Lepidopteris* (Peltaspermales) from the Early Jurassic Cañadón Asfalto Formation, Patagonia, Argentina: International Journal of Plant Sciences, v. 180, p. 578–596, https://doi.org/10.1086/703461.

Elkins-Tanton, L.T., Grasby, S.E., Black, B.A., Veselovskiy, R.V., Ardakani, O.H., and Goodarzi, F., 2020, Field evidence for coal combustion links the 252 Ma Siberian Traps with global carbon disruption: Geology, v. 48, p. 986–991, https://doi.org/10.1130/G47365.1.

Erwin, D.H., 1998, The end and the beginning—recoveries from mass extinctions: Trends in Ecology & Evolution, v. 13, p. 344–349, https://doi.org/10.1016/S0169-5347(98)01436-0.

Feng, Z., Wei, H.-B., Guo, Y., He, X.-Y., Sui, Q., Zhou, Y., Liu, H.-Y., Gou, X.-D., and Lv, Y., 2020, From rainforest to herbland—New insights into land plant responses to the end-Permian mass extinction: Earth-Science Reviews, v. 204, https://doi.org/10.1016/j.earscirev.2020.103153.

Fielding, C.R., et al., 2019, Age and pattern of the southern high-latitude continental end-Permian extinction constrained by multiproxy analysis: Nature Communications, v. 10, 385, https://doi.org/10.1038/s41467-018-07934-z.

Fielding, C.R., Frank, T.D., Tevyaw, A.P., Savatic, K., Vajda, V., McLoughlin, S., Mays, C., Nicoll, R.S., Bocking, M., and Crowley, J.L., 2021, Sedimentology of the continental end-Permian extinction event in the Sydney Basin, eastern Australia: Sedimentology, v. 68, p. 30–62, https://doi.org/10.1111/sed.12782.

Filatoff, J., and Price, P.L., 1988, A Pteridacean spore lineage in the Australian Mesozoic, *in* Jell, P.A., and Playford, G., eds., Palynological and Palaeobotanical Studies in Honour of Basil E. Balme: Sydney, Australia, Association of Australasian Palaeontologists, Memoir 5, p. 89–124, https://catalogue.nla.gov.au/catalog/651308.

Foraponova, T.S., and Karasev, E.V., 2021, Systematic problems of pollen organs of the genus *Permotheca* Zalessky from the Permian of Subangara: Paleontological Journal, v. 55, p. 691–706, https://doi.org/10.1134/S0031030121060058.

Foster, C.B., 1979, Permian plant microfossils of the Blair Athol Coal Measures, Baralaba Coal Measures, and basal Rewan Formation of Queensland [Ph.D. dissertation]: Queensland, Australia, University of Queensland, 244 p., https://catalogue.nla.gov.au/Record/349499.

Foster, C.B., 1982, Spore-pollen assemblages of the Bowen Basin, Queensland (Australia)—Their relationship to the Permian/Triassic boundary: Review of Palaeobotany and Palynology, v. 36, p. 165–183, https://doi.org/10.1016/0034-6667(82)90016-1.

Frank, T.D., et al., 2021, Pace, magnitude, and nature of terrestrial climate change through the end-Permian extinction in southeastern Gondwana: Geology, v. 49, p. 1089–1095, https://doi.org/10.1130/G48795.1.

Galasso, F., Bucher, H., and Schneebeli-Hermann, E., 2022, Mapping monstrosity—Malformed sporomorphs across the Smithian/Spathian boundary interval and beyond (Salt Range, Pakistan): Global and Planetary Change, v. 219, https://doi.org/10.1016/j.gloplacha.2022.103975.

Galfetti, T., et al., 2007a, Timing of the Early Triassic carbon cycle perturbations inferred from new U–Pb ages and ammonoid biochronozones: Earth and Planetary Science Letters, v. 258, p. 593–604, https://doi.org/10.1016/j.epsl.2007.04.023.

Galfetti, T., Hochuli, P.A., Brayard, A., Bucher, H., Weissert, H., and Vigran, J.O., 2007b, Smithian-Spathian boundary event—Evidence for global climatic change in the wake of the end-Permian biotic crisis: Geology, v. 35, p. 291–294, https://doi.org/10.1130/G23117A.1.

Galtier, J., and Scott, A.C., 1979, Studies of Paleozoic ferns: On the genus *Corynepteris*. A redescription of the type and some other European species: Palaeontographica. Abteilung B, Paläophytologie, v. 170, no. 4–6, p. 81–125.

Galtier, J., and Taylor, T.N., 1994, The first record of ferns from the Permian of Antarctica: Review of Palaeobotany and Palynology, v. 83, p. 227–239, https://doi.org/10.1016/0034-6667(94)90071-X.

Gastaldo, R.A., 2012, Taphonomic controls on the distribution of palynomorphs in tidally influenced coastal deltaic settings: Palaios, v. 27, p. 798–810, https://doi.org/10.2110/palo.2012.p12-030r.

Gastaldo, R.A., Neveling, J., Looy, C.V., Bamford, M.K., Kamo, S.L., and Geissman, J.W., 2017, Paleontology of the Blaauwater 67 and 65 farms, South Africa: Testing the *Daptocephalus*/*Lystrosaurus* Biozone boundary in a stratigraphic framework: Palaios, v. 32, p. 349–366, https://doi.org/10.2110/palo.2016.106.

Gastaldo, R.A., Kamo, S.L., Neveling, J., Geissman, J.W., Looy, C.V., and Martini, A.M., 2020, The base of the *Lystrosaurus* Assemblage Zone, Karoo Basin, predates the end-Permian marine extinction: Nature Communications, v. 11, 1428, https://doi.org/10.1038/s41467-020-15243-7.

Goldbery, R., and Holland, W.N., 1973, Stratigraphy and sedimentation of redbed facies in Narrabeen Group of Sydney Basin, Australia: AAPG Bulletin, v. 57, p. 1314–1334, https://doi.org/10.1306/83D90EA8-16C7-11D7-8645000102C1865D.

Gomankov, A.V., and Meyen, S.V., 1986, Tatarina Flora (Composition and Distribution in the Late Permian of Eurasia): Moscow, USSR, Труды Геологического Института Академия Наук СССР, Труды 401, 175 p., https://www.geokniga.org/books/2916 [translated from Татариновая Флора (Состав и Распространение в Поздней Перми Евразии)].

Goudemand, N., Romano, C., Leu, M., Bucher, H., Trotter, J.A., and Williams, I.S., 2019, Dynamic interplay between climate and marine biodiversity upheavals during the early Triassic Smithian-Spathian biotic crisis: Earth-Science Reviews, v. 195, p. 169–178, https://doi.org/10.1016/j.earscirev.2019.01.013.

Gould, R.E., and Delevoryas, T., 1977, The biology of *Glossopteris*—evidence from petrified seed-bearing and pollen-bearing organs: Alcheringa, v. 1, p. 387–399, https://doi.org/10.1080/03115517708527774.

Gradstein, F.M., Ogg, J.G., Schmitz, M.D., and Ogg, G.M., eds., 2020, Geologic Time Scale 2020: Amsterdam, Netherlands, Elsevier, v. 1–2, 1357 p., https://doi.org/10.1016/C2020-1-02369-3.

Grauvogel-Stamm, L., and Ash, S.R., 2005, Recovery of the Triassic land flora from the end-Permian life crisis: Comptes Rendus Palévol, v. 4, p. 593–608, https://doi.org/10.1016/j.crpv.2005.07.002.

Grauvogel-Stamm, L., and Lugardon, B., 2004, The spores of the Triassic lycopsid *Pleuromeia sternbergii* (Münster) corda—Morphology, ultrastructure, phylogenetic implications,

and chronostratigraphic inferences: International Journal of Plant Sciences, v. 165, p. 631–650, https://doi.org/10.1086/386562.

Grimm, E.C., 1987, CONISS—a FORTRAN 77 program for stratigraphically constrained cluster analysis by the method of incremental sum of squares: Computers & Geosciences, v. 13, p. 13–35, https://doi.org/10.1016/0098-3004(87)90022-7.

Grimm, E.C., 1991, TILIA and TILIAGRAPH. PC Spreadsheet and Graphics Software for Pollen Data: NeotomaDB, https://www.neotomadb.org/apps/tilia (accessed January 2025).

Grimm, N.B., et al., 2013, The impacts of climate change on ecosystem structure and function: Frontiers in Ecology and the Environment, v. 11, p. 474–482, https://doi.org/10.1890/120282.

Gröcke, D.R., 1998, Carbon-isotope analyses of fossil plants as a chemostratigraphic and palaeoenvironmental tool: Lethaia, v. 31, p. 1–13, https://doi.org/10.1111/j.1502-3931.1998.tb00482.x.

Gröcke, D.R., 2002, The carbon isotope composition of ancient CO_2 based on higher-plant organic matter: Philosophical Transactions of the Royal Society of London, A: Mathematical, Physical and Engineering Sciences, v. 360, p. 633–658, https://doi.org/10.1098/rsta.2001.0965.

Gröcke, D.R., 2020, Carbon isotope stratigraphy: Principles and applications, *in* Montenari, M., ed., Stratigraphy & Timescales: Massachusetts, USA, Academic Press, Carbon Isotope Stratigraphy, v. 5, p. 1–40, https://doi.org/10.1016/bs.sats.2020.08.002.

Gulbranson, E.L., Isbell, J.L., Taylor, E.L., Ryberg, P.E., Taylor, T.N., and Flaig, P.P., 2012, Permian polar forests—deciduousness and environmental variation: Geobiology, v. 10, p. 479–495, https://doi.org/10.1111/j.1472-4669.2012.00338.x.

Håkansson, E., 1979, Carboniferous to Tertiary development of the Wandel Sea Basin, eastern North Greenland: Rapport Grønlands Geologiske Undersøgelse, v. 88, p. 73–83, https://doi.org/10.34194/rapggu.v88.7558.

Hammer, Ø., Harper, D.A.T., and Ryan, P.D., 2001, PAST—Paleontological statistics software package for education and data analysis: Palaeontologia Electronica, v. 4, p. 1–9, https://www.nhm.uio.no/english/research/resources/past/.

Helby, R., 1970, A biostratigraphy of the late Permian and Triassic of the Sydney Basin [Ph.D. dissertation]: Sydney, Australia, University of Sydney, 513 p., https://ses.library.usyd.edu.au/handle/2123/17203.

Helby, R., and Martin, A.R.H., 1965, *Cylostrobus* gen. nov., cones of lycopsidean plants from the Narrabeen group (Triassic) of New South Wales: Australian Journal of Botany, v. 13, p. 389–404, https://doi.org/10.1071/BT9650389.

Helby, R., Morgan, R., and Partridge, A.D., 1987, A palynological zonation of the Australian Mesozoic, *in* Jell, P.A., ed., Studies in Australian Mesozoic Palynology: Memoirs of the Association of Australasian Palaeontologists, v. 4, p. 1–94.

Herbert, C., 1980, Depositional development of the Sydney Basin, *in* Herbert, C., and Helby, R., eds., A Guide to the Sydney Basin: Australia, Don West, Government Printer, Geological Survey of New South Wales, Department of Mineral Resources Bulletin, v. 26, p. 10–52, https://nswdpe.intersearch.com.au/nswdpejspui/handle/1/2237.

Herbert, C., and Helby, R., eds., 1980, A Guide to the Sydney Basin: Australia, Don West, Government Printer, Geological Survey of New South Wales, Department of Mineral Resources Bulletin 26, 603 p., https://nswdpe.intersearch.com.au/nswdpejspui/handle/1/2237.

Herbert, G., 1997, Sequence stratigraphic analysis of early and middle Triassic alluvial and estuarine fades in the Sydney Basin, Australia: Australian Journal of Earth Sciences, v. 44, p. 125–143, https://doi.org/10.1080/08120099708728299.

Hermann, E., Hochuli, P.A., Bucher, H., Brühwiler, T., Hautmann, M., Ware, D., and Roohi, G., 2011a, Terrestrial ecosystems on North Gondwana following the end-Permian mass extinction: Gondwana Research, v. 20, p. 630–637, https://doi.org/10.1016/j.gr.2011.01.008.

Hermann, E., Hochuli, P.A., Méhay, S., Bucher, H., Brühwiler, T., Ware, D., Hautmann, M., Roohi, G., ur-Rehman, K., and Yaseen, A., 2011b, Organic matter and palaeoenvironmental signals during the Early Triassic biotic recovery—The Salt Range and Surghar Range records: Sedimentary Geology, v. 234, p. 19–41, https://doi.org/10.1016/j.sedgeo.2010.11.003.

Hermann, E., Hochuli, P.A., Bucher, H., and Roohi, G., 2012, Uppermost Permian to Middle Triassic palynology of the Salt Range and Surghar Range, Pakistan: Review of Palaeobotany and Palynology, v. 169, p. 61–95, https://doi.org/10.1016/j.revpalbo.2011.10.004.

Hesselbo, S.P., Morgans-Bell, H.S., McElwain, J.C., Rees, P.M., Robinson, S.A., and Ross, C.E., 2003, Carbon-cycle perturbation in the Middle Jurassic and accompanying changes in the terrestrial paleoenvironment: The Journal of Geology, v. 111, p. 259–276, https://doi.org/10.1086/373968.

Hesselbo, S.P., Korte, C., Ullmann, C.V., and Ebbesen, A.L., 2020, Carbon and oxygen isotope records from the southern Eurasian Seaway following the Triassic-Jurassic boundary—Parallel long-term enhanced carbon burial and seawater warming: Earth-Science Reviews, v. 203, https://doi.org/10.1016/j.earscirev.2020.103131.

Hochuli, P.A., and Vigran, J.O., 2010, Climate variations in the boreal Triassic—Inferred from palynological records from the Barents Sea: Palaeogeography, Palaeoclimatology, Palaeoecology, v. 290, p. 20–42, https://doi.org/10.1016/j.palaeo.2009.08.013.

Hochuli, P.A., Hermann, E., Vigran, J.O., Bucher, H., and Weissert, H., 2010a, Rapid demise and recovery of plant ecosystems across the end-Permian extinction event: Global and Planetary Change, v. 74, p. 144–155, https://doi.org/10.1016/j.gloplacha.2010.10.004.

Hochuli, P.A., Vigran, J.O., Hermann, E., and Bucher, H., 2010b, Multiple climatic changes around the Permian–Triassic boundary event revealed by an expanded palynological record from mid-Norway: Geological Society of America Bulletin, v. 122, p. 884–896, https://doi.org/10.1130/B26551.1.

Hochuli, P.A., Sanson-Barrera, A., Schneebeli-Hermann, E., and Bucher, H., 2016, Severest crisis overlooked—Worst disruption of terrestrial environments postdates the Permian–Triassic mass extinction: Scientific Reports, v. 6, https://doi.org/10.1038/srep28372.

Holmes, W.B.K., 1982, The Middle Triassic flora from Benolong, near Dubbo, central-western New South Wales: Alcheringa, v. 6, p. 1–33, https://doi.org/10.1080/03115518208565416.

Holmes, W.B.K., 1987, New corystosperm ovulate fructifications from the Middle Triassic of eastern Australia: Alcheringa, v. 11, p. 165–173, https://doi.org/10.1080/03115518708618987.

Holmes, W.B.K., 2000, The Middle Triassic megafossil flora of the Basin Creek formation, Nymboida Coal Measures, NSW, Australia. Part 1: Bryophyta, Sphenophyta: Proceedings of the Linnean Society of New South Wales, v. 122, p. 43–68, https://archive.org/details/biostor-68062.

Holmes, W.B.K., and Anderson, H.M., 2005a, The Middle Triassic megafossil flora of the Basin Creek Formation, Nymboida Coal Measures, New South Wales, Australia. Part 4. Umkomasiaceae. *Dicroidium* and affiliated fructifications: Proceedings of the Linnean Society of New South Wales, v. 126, p. 1–37, https://biostor.org/reference/252124.

Holmes, W.B.K., and Anderson, H.M., 2005b, The Middle Triassic megafossil flora of the Basin Creek Formation, Nymboida Coal Measures, New South Wales, Australia. Part 5. The Genera *Lepidopteris*, *Kurtziana*, *Rochipteris* and *Walkomiopteris*: Proceedings of the Linnean Society of New South Wales, v. 126, p. 39–79, https://archive.org/details/biostor-252125.

Holmes, W.B.K., and Anderson, H.M., 2007, The Middle Triassic megafossil flora of the Basin Creek Formation, Nymboida Coal Measures, New South Wales, Australia. Part 6. Ginkgophyta: Proceedings of the Linnean Society of New South Wales, v. 128, p. 155–200, https://archive.org/details/biostor-252202.

Holmes, W.B.K., and Anderson, H.M., 2008, The Middle Triassic megafossil flora of the Basin Creek Formation, Nymboida Coal Measures, New South Wales, Australia. Part 7. Cycadophyta: Proceedings of the Linnean Society of New South Wales, v. 129, p. 113–149, https://archive.org/details/biostor-252207.

Holmes, W.B.K., and Anderson, H.M., 2022, The Middle Triassic megafossil flora of the Basin Creek Formation, Nymboida Coal Measures, New South Wales, Australia. Part 10. Miscellaneous Foliar (*Rochipteris*) and Fertile Genera (*Fraxinopsis*, *Tomiostrobus*, *Umkomasia*, *Weltrichia*): Proceedings of the Linnean Society of New South Wales, v. 144, https://openjournals.library.sydney.edu.au/LIN/article/view/16680.

Hren, M.T., Tice, M.M., and Chamberlain, C.P., 2009, Oxygen and hydrogen isotope evidence for a temperate climate 3.42 billion years ago: Nature, v. 462, p. 205–208, https://doi.org/10.1038/nature08518.

Hua, F., Shao, L., Zhang, T., Bond, D.P.G., Wang, X., Wang, J., Yan, Z., Lu, J., and Hilton, J., 2023, An astronomical timescale for the Permian–Triassic mass extinction reveals a two-step, million-year-long terrestrial crisis in south China: Earth and Planetary Science Letters, v. 605, https://doi.org/10.1016/j.epsl.2023.118035.

International Atomic Energy Agency, 1995, Reference and Intercomparison Materials for Stable Isotopes of Light Elements: International Atomic Energy Agency, IAEA-TECDOC-825, 165 p., https://www.iaea.org/publications/5471/reference-and-intercomparison-materials-for-stable-isotopes-of-light-elements.

Jansonius, J., 1971, Emended diagnosis of *Alisporites* Daugherty, 1941: Pollen et Spores, v. 13, p. 349–357.

Jessop, K., Daczko, N.R., and Piazolo, S., 2019, Tectonic cycles of the New England Orogen, eastern Australia: A Review: Australian Journal of Earth Sciences, v. 66, p. 459–496, https://doi.org/10.1080/08120099.2018.1548378.

Jha, N., and Aggarwal, N., 2012, Permian–Triassic palynostratigraphy in Mailaram area, Godavari Graben, Andhra Pradesh, India: Journal of Earth System Science, v. 121, p. 1257–1285, https://doi.org/10.1007/s12040-012-0224-4.

Jha, N., Pauline Sabina, K., and Mehrotra, N.C., 2011, Early Triassic palynomorphs from Manuguru area of Godavari graben, Andhra Pradesh: Journal of the Geological Society of India, v. 78, p. 167–174, https://doi.org/10.1007/s12594-011-0072-x.

Jha, N., Chary, M.B., and Aggarwal, N., 2012, Permian Triassic palynofloral transition in Chintalapudi area, Godavari Graben, Andhra Pradesh, India: Journal of Earth System Science, v. 121, p. 1287–1303, https://doi.org/10.1007/s12040-012-0228-0.

Juggins, S., 2025, C2: Newcastle University, United Kingdom, https://www.staff.ncl.ac.uk/stephen.juggins/software/C2Home.htm (accessed January 2025).

Kaiho, K., Kajiwara, Y., Nakano, T., Miura, Y., Kawahata, H., Tazaki, K., Ueshima, M., Chen, Z., and Shi, G.R., 2001, End-Permian catastrophe by a bolide impact—Evidence of a gigantic release of sulfur from the mantle: Geology, v. 29, p. 815–818, https://doi.org/10.1130/0091-7613(2001)029<0815:EPCBAB>2.0.CO;2.

Keeley, J.E., 1998, CAM photosynthesis in submerged aquatic plants: Botanical Review, v. 64, p. 121–175, https://doi.org/10.1007/BF02856581.

Kerp, H., Hamad, A.A., Vörding, B., and Bandel, K., 2006, Typical Triassic Gondwanan floral elements in the Upper Permian of the paleotropics: Geology, v. 34, p. 265–268, https://doi.org/10.1130/G22187.1.

Kocsis, Á.T., and Scotese, C.R., 2021, Mapping paleocoastlines and continental flooding during the Phanerozoic: Earth-Science Reviews, v. 213, https://doi.org/10.1016/j.earscirev.2020.103463.

Korte, C., and Kozur, H.W., 2010, Carbon-isotope stratigraphy across the Permian–Triassic boundary—A review: Journal of Asian Earth Sciences, v. 39, p. 215–235, https://doi.org/10.1016/j.jseaes.2010.01.005.

Kozub, D., Shapoval, J., Yatsenko, S., Starikh, V., and Dobarskyi, A., 2025, Helicon Focus: Kharkiv, Ukraine, https://www.heliconsoft.com/heliconsoft-products/helicon-focus/ (accessed January 2025).

Krassilov, V.A., and Bugdaeva, E.V., 1988, Gnetalean plants from the Jurassic of Ust-Balej, East Siberia: Review of Palaeobotany and Palynology, v. 53, p. 359–376, https://doi.org/10.1016/0034-6667(88)90040-1.

Kürschner, W.M., and Herngreen, G.F.W., 2010, Triassic palynology of central and northwestern Europe: a review of palynofloral diversity patterns and biostratigraphic subdivisions, *in* Lucas, S.G., ed., The Triassic Timescale: Geological Society, London, Special Publication 334, p. 263–283, https://doi.org/10.1144/SP334.11.

Kustatscher, E., Ash, S.R., Karasev, E., Pott, C., Vajda, V., Yu, J., and McLoughlin, S., 2018, Flora of the Late Triassic, in Tanner, L.H., ed., The Late Triassic World: Cham, Germany, Springer: Topics in Geobiology, v. 46, p. 545–622, https://doi.org/10.1007/978-3-319-68009-5_13.

Laurie, J.R., et al., 2016, Calibrating the middle and late Permian palynostratigraphy of Australia to the geologic time-scale via U–Pb zircon CA-IDTIMS dating: Australian Journal of Earth Sciences, v. 63, p. 701–730, https://doi.org/10.1080/08120099.2016.1233456.

Lehrmann, D.J., et al., 2015, An integrated biostratigraphy (conodonts and foraminifers) and chronostratigraphy (paleomagnetic reversals, magnetic susceptibility, elemental chemistry, carbon isotopes and geochronology) for the Permian–Upper Triassic strata of Guandao section, Nanpanjiang Basin, south China: Journal of Asian Earth Sciences, v. 108, p. 117–135, https://doi.org/10.1016/j.jseaes.2015.04.030.

Leu, M., Bucher, H., Baud, A., Vennemann, T., Luz, Z., Hautmann, M., and Goudemand, N., 2023, An expanded Smithian-Spathian (Lower Triassic) boundary from a reefal build-up record in Oman—implications for conodont taxonomy, high-resolution biochronology and the carbon isotope record: Papers in Palaeontology, v. 9, https://doi.org/10.1002/spp2.1481.

Leu, M., Schneebeli-Hermann, E., Hammer, Ø., Lindemann, F.-J., and Bucher, H., 2024, Spatiotemporal dynamics of nektonic biodiversity and vegetation shifts during the Smithian–Spathian transition—conodont and palynomorph insights from Svalbard: Lethaia, v. 57, p. 1–19, https://doi.org/10.18261/let.57.2.3.

Li, J., Gastaldo, R.A., Neveling, J., and Geissman, J.W., 2017, Siltstones across the *Daptocephalus* (Dicynodon) and Lystrosaurus assemblage zones, Karoo Basin, South Africa, show no evidence for aridification: Journal of Sedimentary Research, v. 87, p. 653–671, https://doi.org/10.2110/jsr.2017.35.

Li, M., Ogg, J., Zhang, Y., Huang, C., Hinnov, L., Chen, Z.-Q., and Zou, Z., 2016, Astronomical tuning of the end-Permian extinction and the Early Triassic Epoch of south China and Germany: Earth and Planetary Science Letters, v. 441, p. 10–25, https://doi.org/10.1016/j.epsl.2016.02.017.

Li, M., Huang, C., Hinnov, L., Chen, W., Ogg, J., and Tian, W., 2018, Astrochronology of the Anisian stage (Middle Triassic) at the Guandao reference section, south China: Earth and Planetary Science Letters, v. 482, p. 591–606, https://doi.org/10.1016/j.epsl.2017.11.042.

Li, R., Shen, S.-Z., Xia, X.-P., Xiao, B., Feng, Y., and Chen, H., 2024, Atmospheric ozone destruction and the end-Permian crisis—Evidence from multiple sulfur isotopes: Chemical Geology, v. 647, https://doi.org/10.1016/j.chemgeo.2024.121936.

Lindström, S., 2021, Two-phased mass rarity and extinction in land plants during the End-Triassic climate crisis: Frontiers of Earth Science, v. 9, https://doi.org/10.3389/feart.2021.780343.

Lindström, S., and McLoughlin, S., 2007, Synchronous palynofloristic extinction and recovery after the end-Permian event in the Prince Charles Mountains, Antarctica—Implications

for palynofloristic turnover across Gondwana: Review of Palaeobotany and Palynology, v. 145, p. 89–122, https://doi.org/10.1016/j.revpalbo.2006.09.002.

Lindström, S., McLoughlin, S., and Drinnan, A.N., 1997, Intraspecific variation of taeniate bisaccate pollen within Permian glossopterid sporangia, from the Prince Charles Mountains, Antarctica: International Journal of Plant Sciences, v. 158, p. 673–684, https://doi.org/10.1086/297479.

Lindström, S., Erlström, M., Piasecki, S., Nielsen, L.H., and Mathiesen, A., 2017, Palynology and terrestrial ecosystem change of the Middle Triassic to lowermost Jurassic succession of the eastern Danish Basin: Review of Palaeobotany and Palynology, v. 244, p. 65–95, https://doi.org/10.1016/j.revpalbo.2017.04.007.

Lindström, S., Bjerager, M., Alsen, P., Sanei, H., and Bojesen-Koefoed, J., 2020, The Smithian-Spathian boundary in North Greenland—implications for extreme global climate changes: Geological Magazine, v. 157, p. 1547–1567, https://doi.org/10.1017/S0016756819000669.

Litwin, R.J., 1985, Fertile organs and in situ spores of ferns from the late Triassic Chinle Formation of Arizona and New Mexico, with discussion of the associated dispersed spores: Review of Palaeobotany and Palynology, v. 44, p. 101–146, https://doi.org/10.1016/0034-6667(85)90030-2.

Liu, F., Peng, H., Bomfleur, B., Kerp, H., Zhu, H., and Shen, S., 2020, Palynology and vegetation dynamics across the Permian–Triassic boundary in southern Tibet: Earth-Science Reviews, v. 209, https://doi.org/10.1016/j.earscirev.2020.103278.

Looy, C.V., Brugman, W.A., Dilcher, D.L., and Visscher, H., 1999, The delayed resurgence of equatorial forests after the Permian–Triassic ecologic crisis: Proceedings of the

National Academy of Sciences of the United States of America, v. 96, p. 13857–13862, https://doi.org/10.1073/pnas.96.24.13857.

Looy, C.V., Twitchett, R.J., Dilcher, D.L., and Visscher, H., 2001, Life in the end-Permian dead zone: Proceedings of the National Academy of Sciences of the United States of America, v. 98, p. 7879–7883, https://doi.org/10.1073/pnas.131218098.

Looy, C.V., van Konijnenburg-van Cittert, J.H.A., and Duijnstee, I.A.P., 2021, Proliferation of isoëtalean lycophytes during the Permo–Triassic biotic crises: A proxy for the state of the terrestrial biosphere: Frontiers of Earth Science, v. 9, https://doi.org/10.3389/feart.2021.615370.

Lopes, G., Pereira, Z., Fernandes, P., Wicander, R., Matos, J.X., Rosa, D., and Oliveira, J.T., 2014, The significance of reworked palynomorphs (middle Cambrian to Tournaisian) in the Visean Toca da Moura Complex (South Portugal)—Implications for the geodynamic evolution of Ossa Morena Zone: Review of Palaeobotany and Palynology, v. 200, p. 1–23, https://doi.org/10.1016/j.revpalbo.2013.07.003.

Lowery, C.M., et al., 2018, Rapid recovery of life at ground zero of the end-Cretaceous mass extinction: Nature, v. 558, p. 288–291, https://doi.org/10.1038/s41586-018-0163-6.

Lugardon, B., Grauvogel-Stamm, L., and Dobruskina, I., 1999, The microspores of *Pleuromeia rossica* Neuburg (Lycopsida; Triassic)—Comparative ultrastructure and phylogenetic implications: Comptes Rendus de l'Académie des Sciences, v. 329, p. 435–442, https://doi.org/10.1016/S1251-8050(00)80068-3.

Lundblad, B., 1948, A selaginelloid strobilus from East Greenland (Triassic): Dansk Geologisk Forening, v. 11, no. 3, p. 351–363, https://2dgf.dk/publikationer/bulletin/bulletin-volume-11-1946/.

Magohe, S.P., 2019, Preliminary palynology of the Karoo equivalent Tanga Beds, coastal Tanzania—Insights on preservation, age and depositional environments: Tanzania Journal of Science, v. 45, p. 392–404, https://www.ajol.info/index.php/tjs/article/view/191199.

Mangerud, G., 1994, Palynostratigraphy of the Permian and lowermost Triassic succession, Finnmark Platform, Barents sea: Review of Palaeobotany and Palynology, v. 82, p. 317–349, https://doi.org/10.1016/0034-6667(94)90082-5.

Mayne, S.J., Nicholas, E., Bigg-Wither, A.L., Rasidi, J.S., and Raine, M.J., 1974, Geology of the Sydney Basin—A Review: Canberra, Australia, Australian Government Publishing Service, Bureau of Mineral Resources, Geology and Geophysics Bulletin 149, 229 p., https://pid.geoscience.gov.au/dataset/ga/115.

Mays, C., and McLoughlin, S., 2022, End-Permian burnout—The role of Permian–Triassic wildfires in extinction, carbon cycling, and environmental change in Eastern Gondwana: Palaios, v. 37, p. 292–317, https://doi.org/10.2110/palo.2021.051.

Mays, C., Vajda, V., Frank, T.D., Fielding, C.R., Nicoll, R.S., Tevyaw, A.P., and McLoughlin, S., 2020, Refined Permian–Triassic floristic timeline reveals early collapse and delayed recovery of south polar terrestrial ecosystems: Geological Society of America Bulletin, v. 132, p. 1489–1513, https://doi.org/10.1130/B35355.1.

Mays, C., McLoughlin, S., Frank, T.D., Fielding, C.R., Slater, S.M., and Vajda, V., 2021a, Lethal microbial blooms delayed freshwater ecosystem recovery following the end-Permian extinction: Nature Communications, v. 12, 5511, https://doi.org/10.1038/s41467-021-25711-3.

Mays, C., Vajda, V., and McLoughlin, S., 2021b, Permian–Triassic non-marine algae of Gondwana—Distributions, natural affinities and ecological implications: Earth-Science Reviews, v. 212, https://doi.org/10.1016/j.earscirev.2020.103382.

McElwain, J.C., and Punyasena, S.W., 2007, Mass extinction events and the plant fossil record: Trends in Ecology & Evolution, v. 22, p. 548–557, https://doi.org/10.1016/j.tree.2007.09.003.

McLean, N.M., Condon, D.J., Schoene, B., and Bowring, S.A., 2015, Evaluating uncertainties in the calibration of isotopic reference materials and multi-element isotopic tracers (EARTHTIME Tracer Calibration Part II): Geochimica et Cosmochimica Acta, v. 164, p. 481–501, https://doi.org/10.1016/j.gca.2015.02.040.

McLoughlin, S., 2011, *Glossopteris*—insights into the architecture and relationships of an iconic Permian Gondwanan plant: Journal of the Botanical Society of Bengal, v. 65, no. 2, p. 1–14.

McLoughlin, S., Lindström, S., and Drinnan, A.N., 1997, Gondwanan floristic and sedimentological trends during the Permian–Triassic transition—new evidence from the Amery Group, northern Prince Charles Mountains, East Antarctica: Antarctic Science, v. 9, p. 281–298, https://doi.org/10.1017/S0954102097000370.

McLoughlin, S., Nicoll, R.S., Crowley, J.L., Vajda, V., Mays, C., Fielding, C.R., Frank, T.D., Wheeler, A., and Bocking, M., 2021, Age and paleoenvironmental significance of the Frazer Beach Member—A new lithostratigraphic unit overlying the end-Permian extinction horizon in the Sydney Basin, Australia: Frontiers of Earth Science, v. 8, https://doi.org/10.3389/feart.2020.600976.

Merdith, A.S., Williams, S.E., Collins, A.S., Tetley, M.G., Mulder, J.A., Blades, M.L., Young, A., Armistead, S.E., Cannon, J., Zahirovic, S., and Müller, R.D., 2021, Extending full-plate tectonic models into deep time—Linking the Neoproterozoic and the Phanerozoic: Earth-Science Reviews, v. 214, https://doi.org/10.1016/j.earscirev.2020.103477.

Metcalfe, I., Crowley, J.L., Nicoll, R.S., and Schmitz, M., 2015, High-precision U-Pb CA-TIMS calibration of Middle Permian to Lower Triassic sequences, mass extinction and extreme climate-change in eastern Australian Gondwana: Gondwana Research, v. 28, p. 61–81, https://doi.org/10.1016/j.gr.2014.09.002.

Mickle, J.E., 1980, *Ankyropteris* from the Pennsylvanian of Eastern Kentucky: Botanical Gazette, v. 141, p. 230–243, https://doi.org/10.1086/337149.

Minchin, P.R., 1987, An evaluation of the relative robustness of techniques for ecological ordination: Vegetatio, v. 69, p. 89–107, https://doi.org/10.1007/BF00038690.

Mørk, A., and Elvebakk, G., 1999, Lithological description of subcropping Lower and Middle Triassic rocks from the Svalis Dome, Barents Sea: Polar Research, v. 18, p. 83–104, https://doi.org/10.3402/polar.v18i1.6559.

Moss, P.T., Kershaw, A.P., and Grindrod, J., 2005, Pollen transport and deposition in riverine and marine environments within the humid tropics of northeastern Australia: Review of Palaeobotany and Palynology, v. 134, p. 55–69, https://doi.org/10.1016/j.revpalbo.2004.11.003.

Müller, R.D., Cannon, J., Qin, X., Watson, R.J., Gurnis, M., Williams, S., Pfaffelmoser, T., Seton, M., Russell, S.H.J., and Zahirovic, S., 2018, GPlates—Building a virtual Earth through deep time: Geochemistry, Geophysics, Geosystems, v. 19, p. 2243–2261, https://doi.org/10.1029/2018GC007584.

Müller, R.D., Flament, N., Cannon, J., Tetley, M.G., Williams, S.E., Cao, X., Bodur, Ö.F., Zahirovic, S., and Merdith, A., 2022, A tectonic-rules-based mantle reference frame since 1 billion years ago—implications for supercontinent cycles and plate–mantle system evolution: Solid Earth, v. 13, p. 1127–1159, https://doi.org/10.5194/se-13-1127-2022.

Naugolnykh, S.V., 2013a, The heterosporous lycopodiophyte *Pleuromeia rossica* Neuburg, 1960 from the Lower Triassic of the Volga River basin (Russia)—organography and reconstruction according to the 'whole-plant' concept: Wulfenia, v. 20, p. 1–16.

Naugolnykh, S.V., 2013b, New male reproductive organs of gymnosperms *Permotheca colovratica* sp. nov. from the Lower Permian of the Ural Mountains: Paleontological Journal, v. 47, p. 114–126, https://doi.org/10.1134/S0031030113010097.

Nilsson, I., Mangerud, G., and Mørk, A., 1996, Permian stratigraphy of the Svalis Dome, south-western Barents Sea: Norsk Geologisk Tiddsskrift, v. 76, no. 3, p. 127–146, https://njg.geologi.no/publications/permian-stratigraphy-of-the-svalis-domesouth-western-barents-sea/.

Nowak, H., Schneebeli-Hermann, E., and Kustatscher, E., 2019, No mass extinction for land plants at the Permian–Triassic transition: Nature Communications, v. 10, https://doi.org/10.1038/s41467-018-07945-w.

Nowak, H., Kustatscher, E., Roghi, G., and van Konijnenburg-van Cittert, J.H.A., 2024, *In situ* pollen of voltzialean conifers from the Middle Triassic in central Europe: Review of Palaeobotany and Palynology, v. 323, https://doi.org/10.1016/j.revpalbo.2024.105077.

Ogg, J.G., Chen, Z.-Q., Orchard, M.J., and Jiang, H.S., 2020, The Triassic Period, *in* Gradstein, F.M., Ogg, J.G., Schmitz, M.D., and Ogg, G.M., eds., Geologic Time Scale 2020: Elsevier, p. 903–953, https://doi.org/10.1016/B978-0-12-824360-2.00025-5.

Osborn, J.M., and Taylor, T.N., 1993, Pollen morphology and ultrastructure of the Corystospermales: permineralized *in situ* grains from the Triassic of Antarctica: Review of Palaeobotany and Palynology, v. 79, p. 205–219, https://doi.org/10.1016/0034-6667(93)90023-N.

Ovtcharova, M., Bucher, H., Schaltegger, U., Galfetti, T., Brayard, A., and Guex, J., 2006, New Early to Middle Triassic U–Pb ages from south China—Calibration with ammonoid biochronozones and implications for the timing of the Triassic biotic recovery: Earth and Planetary Science Letters, v. 243, p. 463–475, https://doi.org/10.1016/j.epsl.2006.01.042.

Ovtcharova, M., Goudemand, N., Hammer, Ø., Guodun, K., Cordey, F., Galfetti, T., Schaltegger, U., and Bucher, H., 2015, Developing a strategy for accurate definition of a geological boundary through radio-isotopic and biochronological dating—The Early-Middle Triassic boundary (south China): Earth-Science Reviews, v. 146, p. 65–76, https://doi.org/10.1016/j.earscirev.2015.03.006.

Paterson, N.W., Rossi, V.M., and Schneebeli-Hermann, E., 2024, Volcanogenic mercury and plant mutagenesis during the end-Permian mass extinction—Palaeoecological perturbation in northern Pangaea: Gondwana Research, v. 134, p. 123–143, https://doi.org/10.1016/j.gr.2024.06.018.

Paton, M.T., Ivanov, A.V., Fiorentini, M.L., McNaughton, N.J., Mudrovska, I., Reznitskii, L.Z., and Demonterova, E.I., 2010, Late Permian and Early Triassic magmatic pulses in the Angara-Taseeva syncline, southern Siberian Traps and their possible influence on the environment: Russian Geology and Geophysics, v. 51, p. 1012–1020, https://doi.org/10.1016/j.rgg.2010.08.009.

Payne, J.L., Lehrmann, D.J., Wei, J., Orchard, M.J., Schrag, D.P., and Knoll, A.H., 2004, Large perturbations of the carbon cycle during recovery from the end-Permian extinction: Science, v. 305, p. 506–509, https://doi.org/10.1126/science.1097023.

Peng, J., Li, J., Li, W., Slater, S.M., Zhu, H., and Vajda, V., 2018, The Triassic to Early Jurassic palynological record of the Tarim Basin, China: Palaeobiodiversity and Palaeoenvironments, v. 98, p. 7–28, https://doi.org/10.1007/s12549-017-0279-y.

Peng, J., Li, J., Slater, S.M., Zhang, Q., Zhu, H., and Vajda, V., 2019, Triassic vegetation and climate evolution on the northern margin of Gondwana: A palynological study from Tulong, southern Xizang (Tibet), China: Journal of Asian Earth Sciences, v. 175, p. 74–82, https://doi.org/10.1016/j.jseaes.2018.06.005.

Pigg, K.B., and Rothwell, G.W., 1983, *Chaloneria* gen. nov.; heterosporous lycophytes from the Pennsylvanian of North America: Botanical Gazette (Chicago, Illinois, USA), v. 144, no. 1, p. 132–147, https://doi.org/10.1086/337354.

Posit Team, 2025, RStudio—Integrated Development Environment for R: Boston, Massachusetts, USA, https://posit.co/download/rstudio-desktop/ (accessed January 2025).

Potonié, R., 1962, Synopsis of *in situ* spores: Stuttgart, Germany, Schweizerbart, Beihefte zum Geologischen Jahrbuch 52, 204 p. [translated from Synopsis der Sporae *in situ*].

Pott, C., Fischer, T., and Aschauer, B., 2017, *Lunzia austriaca*—a bennettitalean microsporangiate structure with *Cycadopites*-like in situ pollen from the Carnian (Upper Triassic) of Lunz, Austria: Grana, v. 56, p. 321–338, https://doi.org/10.1080/00173134.2017.1282010.

Price, P.L., 1997, Permian to Jurassic palynostratigraphic nomenclature of the Bowen and Surat basins, *in* Green, P.M., ed., The Surat and Bowen Basins, Southeast Queensland: Brisbane,

Australia, Queensland Department of Mines and Energy, Queensland Minerals and Energy Review Series, p. 137–178.

Punt, W., Hoen, P.P., Blackmore, S., Nilsson, S., and Le Thomas, A., 2007, Glossary of pollen and spore terminology: Review of Palaeobotany and Palynology, v. 143, p. 1–81, https://doi.org/10.1016/j.revpalbo.2006.06.008.

R Core Team, 2025, R—A language and environment for statistical computing: Department of the University of Auckland, New Zealand, https://www.R-project.org/ (accessed January 2025).

Retallack, G.J., 1975, The life and times of a Triassic lycopod: Alcheringa, v. 1, p. 3–29, https://doi.org/10.1080/03115517508619477.

Retallack, G.J., 1977, Reconstructing Triassic vegetation of eastern Australasia—a new approach for the biostratigraphy of Gondwanaland: Alcheringa, v. 1, p. 247–278, https://doi.org/10.1080/03115517708527763.

Retallack, G.J., 1980, Late Carboniferous to Middle Triassic megafossil floras from the Sydney Basin, *in* Herbert, C., and Helby, R., eds., A Guide to the Sydney Basin: New South Wales Geological Survey Bulletin 26, p. 384–430, https://nswdpe.intersearch.com.au/nswdpejspui/handle/1/2237.

Retallack, G.J., 1997, Earliest Triassic origin of *Isoetes* and quillwort evolutionary radiation: Journal of Paleontology, v. 71, p. 500–521, https://doi.org/10.1017/S0022336000039524.

Retallack, G., 1999, Postapocalyptic greenhouse paleoclimate revealed by earliest Triassic paleosols in the Sydney Basin, Australia: Geological Society of America Bulletin, v. 111, p. 52–70, https://doi.org/10.1130/0016-7606(1999)111<0052:PGPRBE>2.3.CO;2.

Retallack, G.J., 2002, *Lepidopteris callipteroides*, an earliest Triassic seed fern of the Sydney Basin, southeastern Australia: Alcheringa, v. 26, p. 475–500, https://doi.org/10.1080/03115510208619538.

Retallack, G.J., 2013, Permian and Triassic greenhouse crises: Gondwana Research, v. 24, p. 90–103, https://doi.org/10.1016/j.gr.2012.03.003.

Retallack, G.J., 2019, Leaf preservation in *Eucalyptus* woodland as a model for sclerophyll fossil floras: Alcheringa, v. 43, p. 71–84, https://doi.org/10.1080/03115518.2018.1457180.

Retallack, G.J., and Krull, E.S., 1999, Landscape ecological shift at the Permian-Triassic boundary in Antarctica: Australian Journal of Earth Sciences, v. 46, p. 785–812, https://doi.org/10.1046/j.1440-0952.1999.00745.x.

Retallack, G.J., Renne, P.R., and Kimbrough, D.L., 1993, New radiometric ages for Triassic floras of southeast Gondwana, *in* Lucas, S.G., and Morales, M., eds., The Nonmarine Triassic: Albuquerque, New Mexico, USA: Bulletin of the New Mexico Museum of Natural History and Science, v. 3, p. 415–418, https://nmdigital.unm.edu/digital/collection/bulletins/id/7153/rec/1.

Retallack, G.J., Veevers, J.J., and Morante, R., 1996, Global coal gap between Permian–Triassic extinction and Middle Triassic recovery of peatforming plants: Geological Society of America Bulletin, v. 108, p. 195–207, https://doi.org/10.1130/0016-7606(1996)108<0195:GCGBPT>2.3.CO;2.

Richard, M.J., Duff, B.A., Korsh, R.J., Heidecker, E.J., Scheibner, E., and Turner, N.J., 1983, Tasman Orogen, Australia, *in* Rast, N., and Delany, F.M., eds., Profile of Orogenic Belts,

American Geophysical Union, Geodynamics Series, v. 10, p. 5–19, https://doi.org/10.1029/GD010p0005.

Riding, J.B., 2021, A guide to preparation protocols in palynology: Palynology, v. 45, p. 1–110, https://doi.org/10.1080/01916122.2021.1878305.

Rojas, A., Calatayud, J., Kowalewski, M., Neuman, M., and Rosvall, M., 2021, A multiscale view of the Phanerozoic fossil record reveals the three major biotic transitions: Communications Biology, v. 4, 309, https://doi.org/10.1038/s42003-021-01805-y.

Romano, C., Goudemand, N., Vennemann, T.W., Ware, D., Schneebeli-Hermann, E., Hochuli, P.A., Brühwiler, T., Brinkmann, W., and Bucher, H., 2013, Climatic and biotic upheavals following the end-Permian mass extinction: Nature Geoscience, v. 6, p. 57–60, https://doi.org/10.1038/ngeo1667.

Ruhl, M., Bonis, N.R., Reichart, G.-J., Damsté, J.S.S., and Kürschner, W.M., 2011, Atmospheric carbon injection linked to end-Triassic mass extinction: Science, v. 333, p. 430–434, https://doi.org/10.1126/science.1204255.

Sahney, S., and Benton, M.J., 2008, Recovery from the most profound mass extinction of all time: Proceedings of the Royal Society, B: Biological Sciences, v. 275, p. 759–765, https://doi.org/10.1098/rspb.2007.1370.

Sanson-Barrera, A., 2016, Earliest Triassic climatic, environmental and floral evolution of east Greenland [Ph.D. dissertation]: Zurich, Switzerland, University of Zurich, 55 p., https://doi.org/10.5167/uzh-204634.

Schneebeli-Hermann, E., 2020, Regime shifts in an Early Triassic subtropical ecosystem: Frontiers of Earth Science, v. 8, https://doi.org/10.3389/feart.2020.588696.

Schneebeli-Hermann, E., and Bucher, H., 2015, Palynostratigraphy at the Permian–Triassic boundary of the Amb section, Salt Range, Pakistan: Palynology, v. 39, p. 1–18, https://doi.org/10.1080/01916122.2014.921648.

Schneebeli-Hermann, E., Hochuli, P.A., Bucher, H., Goudemand, N., Brühwiler, T., and Galfetti, T., 2012a, Palynology of the Lower Triassic succession of Tulong, south Tibet—Evidence for early recovery of gymnosperms: Palaeogeography, Palaeoclimatology, Palaeoecology, v. 339–341, p. 12–24, https://doi.org/10.1016/j.palaeo.2012.04.010.

Schneebeli-Hermann, E., Kürschner, W.M., Hochuli, P.A., Bucher, H., Ware, D., Goudemand, N., and Roohi, G., 2012b, Palynofacies analysis of the Permian–Triassic transition in the Amb section (Salt Range, Pakistan)—Implications for the anoxia on the South Tethyan Margin: Journal of Asian Earth Sciences, v. 60, p. 225–234, https://doi.org/10.1016/j.jseaes.2012.09.005.

Schneebeli-Hermann, E., Kürschner, W.M., Kerp, H., Bomfleur, B., Hochuli, P.A., Bucher, H., Ware, D., and Roohi, G., 2015, Vegetation history across the Permian–Triassic boundary in Pakistan (Amb section, Salt Range): Gondwana Research, v. 27, p. 911–924, https://doi.org/10.1016/j.gr.2013.11.007.

Schobben, M., van de Schootbrugge, B., and Wignall, P.B., 2019, Interpreting the carbon isotope record of mass extinctions: Elements, v. 15, p. 331–337, https://doi.org/10.2138/gselements.15.5.331.

Scholze, F., Wang, X., Kirscher, U., Kraft, J., Schneider, J.W., Götz, A.E., Joachimski, M.M., and Bachtadse, V., 2017, A multistratigraphic approach to pinpoint the Permian–Triassic boundary in continental deposits—The Zechstein–Lower Buntsandstein transition in Germany:

Global and Planetary Change, v. 152, p. 129–151, https://doi.org/10.1016/j.gloplacha.2017.03.004.

Schulze, F., 1855, Remarks on the occurrence of well-preserved cellulose in lignite and hard coal [translated from Bemerkungen über das vorkommen wohlerhaltener cellulose in braunkohle und

steinkohle]: Bericht über die zur Bekanntmachung geeigneten Verhandlungen der Königlichen Preussische Akademie der Wissenschaften zu Berlin—Sitzung der physikalisch-mathematischen Klasse, v. 5, p. 676–678, https://www.biodiversitylibrary.org/item/41576.

Sheldon, N.D., 2005, Do red beds indicate paleoclimatic conditions?—A Permian case study: Palaeogeography, Palaeoclimatology, Palaeoecology, v. 228, p. 305–319, https://doi.org/10.1016/j.palaeo.2005.06.009.

Shen, J., Algeo, T.J., Planavsky, N.J., Yu, J., Feng, Q., Song, H., Song, H., Rowe, H., Zhou, L., and Chen, J., 2019, Mercury enrichments provide evidence of Early Triassic volcanism following the end-Permian mass extinction: Earth-Science Reviews, v. 195, p. 191–212, https://doi.org/10.1016/j.earscirev.2019.05.010.

Shen, J., Chen, J., Yu, J., Algeo, T.J., Smith, R.M.H., Botha, J., Frank, T.D., Fielding, C.R., Ward, P.D., and Mather, T.A., 2023, Mercury evidence from southern Pangea terrestrial sections for end-Permian global volcanic effects: Nature Communications, v. 14, 6, https://doi.org/10.1038/s41467-022-35272-8.

Shu, W., et al., 2023, Permian-Middle Triassic floral succession in North China and implications for the great transition of continental ecosystems: Geological Society of America Bulletin, v. 135, p. 1747–1767, https://doi.org/10.1130/B36316.1.

Slater, S.M., Twitchett, R.J., Danise, S., and Vajda, V., 2019, Substantial vegetation response to Early Jurassic global warming with impacts on oceanic anoxia: Nature Geoscience, v. 12, p. 462–467, https://doi.org/10.1038/s41561-019-0349-z.

Smith, B.C., and Bocking, M.A., 1993, Well Completion Report, Pacific Power Hawkesbury, Eveleigh DDH 1 PEL 5: Pacific Power Well Report WCR258, 1130 p., https://search.geoscience.nsw.gov.au/report/R00002580.

Smith, B.C., and Bocking, M.A., 1994, Well Completion Report, Pacific Power Hawkesbury Bunnerong DDH 1 PEL 5: Pacific Power Well Report WCR257, 1412 p., https://search.geoscience.nsw.gov.au/report/R00002581.

Song, H., Tong, J., Algeo, T.J., Horacek, M., Qiu, H., Song, H., Tian, L., and Chen, Z.-Q., 2013, Large vertical $\delta^{13}C_{DIC}$ gradients in Early Triassic seas of the south China craton—Implications for oceanographic changes related to Siberian Traps volcanism: Global and Planetary Change, v. 105, p. 7–20, https://doi.org/10.1016/j.gloplacha.2012.10.023.

Song, H., Wignall, P.B., and Dunhill, A.M., 2018, Decoupled taxonomic and ecological recoveries from the Permo–Triassic extinction: Science Advances, v. 4, https://doi.org/10.1126/sciadv.aat5091.

Song, H., Huang, S., Jia, E., Dai, X., Wignall, P.B., and Dunhill, A.M., 2020, Flat latitudinal diversity gradient caused by the Permian–Triassic mass extinction: Proceedings of the National Academy of Sciences of the United States of America, v. 117, p. 17578–17583, https://doi.org/10.1073/pnas.1918953117.

Stanley, S.M., 2009, Evidence from ammonoids and conodonts for multiple Early Triassic mass extinctions: Proceedings of the National Academy of Sciences of the United States of America, v. 106, p. 15264–15267, https://doi.org/10.1073/pnas.0907992106.

Stanley, S.M., 2016, Estimates of the magnitudes of major marine mass extinctions in earth history: Proceedings of the National Academy of Sciences of the United States of America, v. 113, p. E6325–E6334, https://doi.org/10.1073/pnas.1613094113.

Stemmerik, L., and Håkansson, E., 1989, Stratigraphy and depositional history of the upper Palaeozoic and Triassic sediments in the Wandel Sea Basin, central and eastern North Greenland: Rapport Grønlands Geologiske Undersøgelse, v. 143, p. 21–45, https://doi.org/10.34194/rapggu.v143.8056.

Stuecker, M.F., et al., 2018, Polar amplification dominated by local forcing and feedbacks: Nature Climate Change, v. 8, p. 1076–1081, https://doi.org/10.1038/s41558-018-0339-y.

Sun, Y., Joachimski, M.M., Wignall, P.B., Yan, C., Chen, Y., Jiang, H., Wang, L., and Lai, X., 2012, Lethally hot temperatures during the Early Triassic greenhouse: Science, v. 338, p. 366–370, https://doi.org/10.1126/science.1224126.

Sun, Y.D., Richoz, S., Krystyn, L., Grasby, S.E., Chen, Y.L., Banerjee, D., and Joachimski, M.M., 2021, Integrated bio-chemostratigraphy of Lower and Middle Triassic marine successions at Spiti in the Indian Himalaya—Implications for the Early Triassic nutrient crisis: Global and Planetary Change, v. 196, https://doi.org/10.1016/j.gloplacha.2020.103363.

Svensen, H.H., Frolov, S., Akhmanov, G.G., Polozov, A.G., Jerram, D.A., Shiganova, O.V., Melnikov, N.V., Iyer, K., and Planke, S., 2018, Sills and gas generation in the Siberian Traps: Philosophical Transactions of the Royal Society, A: Mathematical, Physical and Engineering Sciences, v. 376, https://doi.org/10.1098/rsta.2017.0080.

Taylor, E.L., Taylor, T.N., and Cúneo, N.R., 1992, The present is not the key to the past—A polar forest from the Permian of Antarctica: Science, v. 257, p. 1675–1677, https://doi.org/10.1126/science.257.5077.1675.

Tekleva, M.V., Polevova, S.V., and Zavialova, N.E., 2007, On some peculiarities of sporoderm structure in members of the Cycadales and Ginkgoales: Paleontological Journal, v. 41, p. 1162–1178, https://doi.org/10.1134/S0031030107110159.

Traverse, A., 2007, Paleopalynology (2nd edition): Dordrecht, Germany, Springer, 813 p., https://doi.org/10.1007/978-1-4020-5610-9.

Trotter, J.A., Williams, I.S., Nicora, A., Mazza, M., and Rigo, M., 2015, Long-term cycles of Triassic climate change—a new $\delta^{18}O$ record from conodont apatite: Earth and Planetary Science Letters, v. 415, p. 165–174, https://doi.org/10.1016/j.epsl.2015.01.038.

Turner, H.-A., McLoughlin, S., and Mays, C., 2024, Comprehensive survey of Early to Middle Triassic Gondwanan floras reveals under-representation of plant–arthropod interactions: Frontiers in Ecology and Evolution, v. 12, https://doi.org/10.3389/fevo.2024.1419254.

Tyson, R.V., 1995, Sedimentary Organic Matter—Organic Facies and Palynofacies: Dordrecht, Netherlands, Springer, 615 p., https://doi.org/10.1007/978-94-011-0739-6.

Utting, J., and Piasecki, S., 1995, Palynology of the Permian of northern continents: A review, *in* Scholle, P.A., Peryt, M., and Ulmer-Scholle, D.S., eds., The Permian of Northern Pangea: Berlin, Springer, v. 1, p. 236–261, https://doi.org/10.1007/978-3-642-78593-1_15.

Vajda, V., and Kear, B.P., 2024, An earliest Triassic riparian ecosystem from the Bulgo Sandstone (Sydney Basin), Australia: Palynofloral evidence of a high-latitude terrestrial vertebrate habitat after the end-Permian mass extinction: Alcheringa, v. 48, p. 483–494, https://doi.org/10.1080/03115518.2024.2392489.

Vajda, V., McLoughlin, S., Mays, C., Frank, T.D., Fielding, C.R., Tevyaw, A., Lehsten, V., Bocking, M., and Nicoll, R.S., 2020, End-Permian (252 Mya) deforestation, wildfires and flooding—An ancient biotic crisis with lessons for the present: Earth and Planetary Science Letters, v. 529, https://doi.org/10.1016/j.epsl.2019.115875.

Vajda, V., Sigfridsson Clauss, K.G.V., Krüger, A., and Nehzati, S., 2023a, Changes in Fe-redox and Fe-species across the end-Permian 'Dead Zone' in the Sydney Basin, Australia (252.10±0.06 Ma)—Evidence from X-ray absorption spectroscopy: Evolving Earth, v. 1, https://doi.org/10.1016/j.eve.2023.100029.

Vajda, V., McLoughlin, S., Slater, S.M., Gustafsson, O., and Rasmusson, A.G., 2023b, The 'seed-fern' *Lepidopteris* mass-produced the abnormal pollen *Ricciisporites* during the end-Triassic biotic crisis: Palaeogeography, Palaeoclimatology, Palaeoecology, v. 627, https://doi.org/10.1016/j.palaeo.2023.111723.

Vajda, V., McLoughlin, S., Slater, S.M., Gustafsson, O., and Rasmusson, A.G., 2024, Confirmation that *Antevsia zeilleri* microsporangiate organs associated with latest Triassic *Lepidopteris ottonis* (Peltaspermales) leaves produced *Cycadopites*-*Monosulcites*-*Chasmatosporites*- and *Ricciisporites*-type monosulcate pollen: Palaeogeography, Palaeoclimatology, Palaeoecology, v. 640, https://doi.org/10.1016/j.palaeo.2024.112111.

Valentina, C., 2021, Palynology and paleobotany of Permo–Triassic Beacon Supergroup at Allan Hills, South Victoria Land, Antarctica: Stratigraphical and paleoenvironmental change implications [Ph.D. dissertation]: Siena, Italy, University of Siena, 198 p., https://doi.org/10.25434/corti-valentina_phd2021.

van Konijnenburg-van Cittert, J.H.A., 1971, *In situ* gymnosperm pollen from the Middle Jurassic of Yorkshire: Acta Botanica Neerlandica, v. 20, p. 1–97, https://doi.org/10.1111/j.1438-8677.1971.tb00688.x.

Vigran, J.O., Mangerud, G., Mørk, A., Bugge, T., and Weitschat, W., 1998, Biostratigraphy and sequence stratigraphy of the lower and middle Triassic deposits from the Svalis Dome, Central Barents Sea, Norway: Palynology, v. 22, p. 89–141, https://doi.org/10.1080/01916122.1998.9989505.

Visscher, H., and van der Zwan, C.J., 1981, Palynology of the circum-Mediterranean Triassic: Phytogeographical and palaeoclimatological implications: Geologische Rundschau, v. 70, p. 625–634, https://doi.org/10.1007/BF01822140.

Visscher, H., Looy, C.V., Collinson, M.E., Brinkhuis, H., van Konijnenburg-van Cittert, J.H.A., Kürschner, W.M., and Sephton, M.A., 2004, Environmental mutagenesis during the end-Permian ecological crisis: Proceedings of the National Academy of Sciences of the United States of America, v. 101, p. 12952–12956, https://doi.org/10.1073/pnas.0404472101.

Ward, C.R., 1972, Sedimentation in the Narrabeen Group, southern Sydney Basin, New South Wales: Journal of the Geological Society of Australia, v. 19, p. 393–409, https://doi.org/10.1080/00167617208728809.

Ward, C.R., Harrington, H.J., Mallett, C.W., and Beeston, J.W., eds., 1995, Geology of Australian Coal Basins: Sydney, Australia, Geological Society of Australia, Coal Geology Group Special Publication 1, 596 p., https://www.osti.gov/etdeweb/biblio/240845.

Wells, A.T., 1995, Nymboida, Red Cliff and Evans Head Coal Measures, New South Wales, *in* Ward, C.R., Harrington, H.J., Mallett, C.W., and Beeston, J.W., eds., Geology of

Australian Coal Basins: Sydney, Australia, Geological Society of Australia, Coal Geology Group, Geology of Australian Coal Basin, Special Publication 1, p. 529–532. Weng, C., and Hooghiemstra, H., 2024, How many pollen grains should we count?—A basic statistical view: Review of Palaeobotany and Palynology, v. 330, https://doi.org/10.1016/j.revpalbo.2024.105126.

Wickham, H., 2016, ggplot2—Elegant graphics for data analysis: New York, USA, Springer-Verlag, https://ggplot2.tidyverse.org (accessed January 2025).

Wickham, H., Francois, R., Henry, L., Müller, K., and Vaughan, D., 2023, dplyr—A grammar of data manipulation: R package version 1.1.4, https://dplyr.tidyverse.org (accessed December 2024).

Widmann, P., Bucher, H., Leu, M., Vennemann, T., Bagherpour, B., Schneebeli-Hermann, E., Goudemand, N., and Schaltegger, U., 2020, Dynamics of the largest carbon isotope excursion during the Early Triassic biotic recovery: Frontiers of Earth Science, v. 8, https://doi.org/10.3389/feart.2020.00196.

Wood, G.R., and Beeston, J.W., 1979, A late Permian lycopod cone *Skilliostrobus* sp. cf. *S. australis* Ash 1979 from Queensland: Geological Survey of Queensland Publications, v. 387, p. 41–49.

Wu, Q., et al., 2024, The terrestrial end-Permian mass extinction in the paleotropics postdates the marine extinction: Science Advances, v. 10, https://doi.org/10.1126/sciadv.adi7284.

Xiong, C., Wang, J., Huang, P., Cascales-Miñana, B., Cleal, C.J., Benton, M.J., and Xue, J., 2021, Plant resilience and extinctions through the Permian to Middle Triassic on the North

China Block—A multilevel diversity analysis of macrofossil records: Earth-Science Reviews, v. 223, https://doi.org/10.1016/j.earscirev.2021.103846.

Xu, Z., Hilton, J., Yu, J., Wignall, P.B., Yin, H., Xue, Q., Ran, W., Li, H., Shen, J., and Meng, F., 2022, End Permian to Middle Triassic plant species richness and abundance patterns in south China—Coevolution of plants and the environment through the Permian–Triassic transition: Earth-Science Reviews, v. 232, https://doi.org/10.1016/j.earscirev.2022.104136.

Zavialova, N., and Karasev, E., 2015, Exine ultrastructure of in situ *Protohaploxypinus* from a Permian peltasperm pollen organ, Russian Platform: Review of Palaeobotany and Palynology, v. 213, p. 27–41, https://doi.org/10.1016/j.revpalbo.2014.11.003.

Zavialova, N., Kustatscher, E., and van Konijnenburg-van Cittert, J.H.A., 2010, Spore ultrastructure of *Selaginellites leonardii* and diversity of selaginellalean spores: Geo.Alp, v. 7, p. 1–18.

Zavialova, N., Nosova, N., and Gavrilova, O., 2016, Pollen grains associated with gymnospermous mesofossils from the Jurassic of Uzbekistan: Review of Palaeobotany and Palynology, v. 233, p. 125–145, https://www.doi.org/10.1016/j.revpalbo.2016.07.009.

Zhang, F., Romaniello, S.J., Algeo, T.J., Lau, K.V., Clapham, M.E., Richoz, S., Herrmann, A.D., Smith, H., Horacek, M., and Anbar, A.D., 2018, Multiple episodes of extensive marine anoxia linked to global warming and continental weathering following the latest Permian mass extinction: Science Advances, v. 4, https://doi.org/10.1126/sciadv.1602921.

Zhao, H., Algeo, T.J., Liu, Y., Chen, Z.-Q., Zhang, L., Hu, Z., and Li, Z., 2020, Lower Triassic carbonate $\delta^{238}U$ record demonstrates expanded oceanic anoxia during Smithian Thermal Maximum and improved ventilation during Smithian-Spathian boundary cooling event:

Palaeogeography, Palaeoclimatology, Palaeoecology, v. 539, https://doi.org/10.1016/j.palaeo.2019.109393.

FOOTNOTES

[1]Supplemental Material. Data repository can be found in Table S1. Additional palynomorph specimen details (e.g., England Finder location) are in Table S2. Authorities of mentioned plant microfossil taxa are in Table S3. Statistical summary of stable carbon isotopes and total organic matter is in Table S4. Review of the expected microfloras found in the Sydney Basin from the Lopingian to the Anisian is in Table S5. Location of analyzed borehole sites is in Figure S1. Cluster analysis of floral groupings is in Figure S2. Shepard plot for ordination data analysis goodness-of-fit is in Figure S3. Examples of putative reworked plant microfossils are in Figure S4. Unconformity between the Wombarra Claystone and Scarborough Sandstone is in Figure S5.

Science Editor: Troy Rasbury

Associate Editor: Daniel Peppe

Reviewers: Robert A. Gastaldo, Anonymous

Cite as: Amores, M., Frank, T.D., Fielding, C.R., Hren, M.T. & Mays, C., 2025. Age-controlled south polar floral trends show a staggered Early Triassic gymnosperm recovery

following the end-Permian event. Geological Society of America Bulletin, v. 137, no. 7–8 3255–3282, https://doi.org/10.1130/B38017.1.